Advancing Computational Analysis and Modelling of EEG/MEG Data

Dheeraj Rathee (BE, MTech)

Faculty of Computing, Engineering and the
Built Environment, Ulster University

Thesis submitted for the degree of

Doctor of Philosophy (PhD)

February, 2019

I confirm that the word count of this thesis is less than 100,000 words

Jai Dada Ram Singh

To my late grandparents

Mrs. Pyari Devi

Mr. Sube Singh Rathee

Contents

Acknowledgments

This work was carried out at the Intelligent Systems Research Centre (ISRC), Faculty of Computing, Engineering and the Built Environment, Ulster University, and financially supported by Vice Chancellor's Research Scholarship (VCRS) award.

I owe immense gratitude to my supervisors, Prof Girijesh Prasad and Dr Hubert Ceccoti for providing excellent supervision and being so enjoyable to work with. I want to thank for their everlasting cooperation and reliance as well as the scientific and personal support and guidance.

I am greatly appreciative to all my collaborators for their valuable contribution. I want to especially thank Dr Haider Raza, Dr Yogesh Kumar Meena, Dr Anirban Chowdhury, Mr Sujit Roy, and Prof Ashish Dutta for their scientific contributions and sharing their expertise related to M/EEG data analysis and stroke rehabilitation. They were always available for discussions and willing to answer questions for which I am very thankful. I really appreciate Dr Jose Bornot for the MEG training, and Dr Alok Joshi and Dr Naomi Du Bois for valuable suggestions and support.

Special thanks go to my fellows in ISRC who provided a great working atmosphere in the lab so that I can fully concentrate on my research. I sincerely thank Dr KongFatt Wong-Lin as the internal reviewer who supported me in all stages of my PhD programme and for his constructive comments on my 100 day report, confirmation report, and thesis. I appreciate Miss Paula Sheerin, Mrs Louise Gallagher, and Mrs Michelle Stewart for dealing with my multiple travel arrangements and document submissions during these years.

Finally, yet importantly, I owe a lot to the support of my parents (Mrs. Bimla Devi and Mr. Kartar Singh Rathee), brother and sister (Yogesh and Promila), wife (Neeharika), sister-in-law (Munesh), lovely nieces and nephews (Nikhil, Ritik, Daksh, Peehu) and my beautiful daughter (Moira). Without their indefatigable support and love, I could never have reached this point.

Declaration

"I hereby declare that with effect from the date on which the thesis is deposited in Research Student Administration of Ulster University, I permit

1. the Librarian of the University to allow the thesis to be copied in whole or in part without reference to me on the understanding that such authority applies to the provision of single copies made for study purposes or for inclusion within the stock of another library.

2. the thesis to be made available through the Ulster Institutional Repository and/or EThOS under the terms of the Ulster eTheses Deposit Agreement which I have signed.

IT IS A CONDITION OF USE OF THIS THESIS THAT ANYONE WHO CONSULTS IT MUST RECOGNISE THAT THE COPYRIGHT RESTS WITH THE UNIVERSITY AND THEN SUBSEQUENTLY TO THE AUTHOR ON THE EXPIRY OF THIS PERIOD AND THAT NO QUOTATION FROM THE THESIS AND NO INFORMATION DERIVED FROM IT MAY BE PUBLISHED UNLESS THE SOURCE IS PROPERLY ACKNOWLEDGED.'

Dheeraj Rathee

Abstract

To better understand the human brain, further advancements in the capabilities of computational modelling and analysis of functional neuroimaging data are required. Electro− and magneto−encephalography (EEG and MEG) technologies provide efficient ways to study the complex neural characteristics of both healthy and diseased brains. This thesis contributes towards extending the current approaches for analysis and functional connectivity (FC) modelling of M/EEG data. It includes an extensive review of the different computational modelling and analysis methods applied for the pre-processing, feature mining, and feature learning of the M/EEG signals in pursuit of single-trial neurophysiological patterns and their applications in various fields. This is followed by a review of current frameworks for modelling large scale functional brain networks. These reviews have identified open research challenges in terms of low performance of M/EEG based single-trial detection systems due to insufficient/inappropriate pre-processing and feature extraction methods and lack of neurophysiological validation of such systems. The research undertaken towards addressing these challenges have led to three original research contributions. In the first contribution, the estimation of current source density (CSD) is introduced as an essential pre-processing step for EEG analysis. It is shown that CSD significantly improves the distinction of motor-imagery (MI) related brain responses and has performed better than other referencing schemes (i.e. common reference and common average reference) and spherical surface Laplacian (SSL) methods (i.e. finite difference method and SSL using realistic head model). In the second contribution, EEG-based single-trial FC networks are introduced for MI (hand, feet, and tongue imagery kinaesthetic movements) and cognitive imagery (CI) tasks (word generation, mathematical subtraction, and spatial navigation) by implementing 'partial' granger causality modelling (PGCM) on two publically available EEG datasets. The outcome demonstrated that EEG brain networks for mixed imagery tasks (i.e. combination of CI and MI) can provide higher classification accuracy (for both binary and multi-class approaches) as compared to the current state-of-the-art method i.e. common spatial patterns (CSP). Moreover, it is shown for the first time that the FC between spatially distributed brain regions can provide additional useful discriminant information for the classification of the brain responses evoked during imagery tasks. In the third contribution, we investigated the temporal evolution and reorganisation of resting-state MEG FC networks over the four weeks of a multi-modal EEG-driven post-stroke upper limb (UL) movement rehabilitative therapy. The findings provide reliable brain connectivity patterns for evaluating UL functional recovery during stroke neurorehabilitation.

Abbreviations

AAL Automated Anatomical Labelling

ADHD Attention-Deficit Hyperactivity Disorder

ADL Activities of Daily Living

AIC Akaike Information Criterion

ALS Amyotrophic Lateral Sclerosis

AR Autoregressive

ARAT Action Research Arm Test

AUC Area Under The ROC Curve

BCI Brain-Computer Interface

BAPD Brain Activation Pattern Detection

BGC Bivariate Granger Causality

BLDA Bayesian Linear Discriminant Analysis

BMI Brain-Machine Interface

BP Band-power

CAR Common Average Reference

CGC Conditional Granger Causality

CI Cognitive Imagery

CR Common Reference

CSD Current Source Density

CSP Common Spatial Pattern

CV Cross-Validation

DTF Directed Transfer Function

ECoG Electrocorticography

EEG Electroencephalography

EKG Electrocardiogram

EMG Electromyography

EOG Electrooculography

ERD Event-Related Desynchronisation

ERP Event-Related Potential

ERS Event-Related Synchronisation

FBCSP Filter Bank Common Spatial Pattern

FBN Functional Brain Networks

FC Functional Connectivity

FDR False Discovery Rate

FES Functional Electrical Stimulation

fMRI Functional Magnetic Resonance Imaging

GCM Granger Causality Modelling

GS Grip-Strength

GUI Graphical User Interface

HPI Head Position Indicator

ICA Independent Component Analysis

ITR Information Transfer Rate

kNN k-Nearest Neighbours

LDA Linear Discriminant Analysis

LFP Local Field Potentials

LIS Locked-in Syndrome

LWR Levinson-Wiggins-Robinson

PCA Principle Component Analysis

PDC Partial Directed Coherence

PET Positron Emmision Tomography

PGC Partial Granger Causality

PMC Premotor Cortex

PP Physical Practice

MA Motor Attempt

MCID Minimal Clinically Important Difference

MEG Magnetoencephalography

MI Motor Imagery

MIM Multivariate Interaction Measure

MMSE Mini-Mental State Examination

MP Mental Practice

MVAR Multivariate Autoregressive Model

NIRS Near-Infrared Spectroscopy

RS Resting-state

ROI Region of Interest

SBIC Schwarz Bayesian Information Criterion

SCP Slow Cortical Potential

SL Surface Laplacian

SMA Supplementary Motor Area

SMR Sensorimotor Rhythm

SNR Signal-To-Noise Ratio

SPECT Single Positron Emission Computerised Tomography

SSVEP Steady-State Visual Evoked Potential

SSL Spherical Surface Laplacian

SSS Signal-Space Separation

SQUID Superconducting Quantum Interference Devices

SVM Support Vector Machines

UL Upper-limb

VC Volume Conduction

List of Tables

List of Figures

Chapter 1

Introduction

1.1 Introduction and problem statement

Functional neuroimaging methods provide a means of evaluating local changes in brain activity and can be performed on healthy (normal) as well as diseased (compromised) brains [1, 2, 3]. Several functional neuroimaging methods are currently available, including those based on a hemodynamic measure (e.g. functional magnetic resonance imaging (fMRI)) and those based on electrophysiological and associated mechanisms of the brain (e.g. electroencephalography (EEG) and magnetoencephalography (MEG)). The electric currents in the synchronously-active neural population cause generation of electric potentials [4] and magnetic fields [5] which can be measured non-invasively using EEG and MEG, respectively. Both neuroimaging techniques have developed into widely used quantitative diagnostic tools in the analysis of brain signals and patterns. EEG and MEG potentially contain a rich source of information related to the functional, physiological, and pathological status of the brain.

Computational modelling and analysis of the M/EEG data required extensive implementation of signal processing algorithms. The signal analysis process must consider additional constraints, e.g., minimal computational cost and availability of small data points in case the system needs to work in online (real-time)

scenario involving single-trial based feature/pattern detection. M/EEG based single-trial feature detection systems have been extensively used for various applications such as clinical decision making, rehabilitative and restorative interventions, communication and control, and cognitive training [6, 7, 8, 9, 10]. A typical signal processing and analysis pipeline of an M/EEG data analysis system consists of several steps: data acquisition, pre-processing, feature extraction, feature translation and machine learning. Each of these steps involves dedicated computational methods and contributes to the over all performance of the system. Despite decades of research and development of these computational methods single-trial M/EEG-based brain activation pattern detection (BAPD) systems (e.g. brain-computer interfaces (BCIs)) have found very limited usage in real-world applications. Thus, there is a pressing need to improve the performance and reliability of these M/EEG-based systems by further advancing the computational analysis and modelling of M/EEG data.

This thesis aims to undertake the following open challenges in the research field of M/EEG computational analysis and modelling:

- Volume conduction (VC) involves mixing of the spatio-temporal information generated at the cortical sources of the brain as the tissues and bone structure between the human cortex and the scalp induce superimposition of electrophysiological dynamics of the EEG signal [11, 12]. This may result in diminished separability of the EEG features for distinct cognitive tasks/processes and hence, severely affects the performance of the EEG-based BAPD systems. Several measures i.e. EEG referencing schemes and surface Laplacian (SL) estimation can be applied for minimising the effect of VC at the scalp level recordings [13, 14, 15, 16, 17] (for further details refer to [18]). However, majority of previous research studies involve qualitative comparison of different spatial transformation methods often restricting their analysis to different algorithms or different parameters for the same algorithm (e.g. parameters optimisation of SL methods, source imaging techniques, or different independent component

analysis (ICA) algorithms) [19, 20, 21]. Thus, there is an urgent need for an empirical evaluation of the effect of the current available referencing schemes and SL methods on single-trial classification of EEG signals.

- One of the probable reasons for the lower performance of current EEG-based BAPD systems is the use of features derived from channel specific data (e.g. band-power (BP), autoregressive (AR), common spatial patterns (CSP) and wavelets), which may not contain information about interactions among different brain regions, while it is well known that multiple brain regions dynamically interact in accomplishing a mental task. Over the last few years, several research groups attempted to implement connectivity-based BCIs [22, 23, 24, 25, 26] using different measures to map the interactions between distinct brain regions. However, a majority of these studies reported lower performances of connectivity-based features for single-trial BAPD systems.

- A major application field of M/EEG-based single-trial BAPD systems is upper-limb (UL) stroke rehabilitation [27, 28, 8, 29]. Majority of the previous studies related to this field relied on the behavioural measures for the assessment of the efficacy of M/EEG based UL stroke rehabilitative interventions in terms of functional recovery. Recently, neurophysiological measures such as functional brain networks (FBNs) have been evaluated successfully for this purpose. However, reorganisation of FBNs during the course of a longitudinal M/EEG-based UL stroke rehabilitation intervention is still poorly understood. Thus, the neurophysiological patterns based on M/EEG FBNs must be explored to better understand the process of stroke recovery and to assess the clinical efficacy of the M/EEG based UL stroke rehabilitation intervention.

1.2 Thesis outline

The remainder of the thesis is organised as follows.

- **Chapter 2** outlines the key idea and motivation behind advancing the current computational analysis and modelling methods for M/EEG-based BAPD systems. This chapter will provide a systematic discussion on several topics related to this field of research. First, Section 2.1 introduces this chapter. Second, Section 2.2 provides a brief description about the anatomical and physiological aspects of the human brain along with EEG and MEG neuroimaging technologies. Third, various steps involved in a single-trial BAPD system using M/EEG data are described in Section 2.3. Fourth, current referencing schemes and SL approaches for EEG data are presented in Section 2.4. Fifth, Section 2.5 describes two state-of-the-art M/EEG feature extraction methods i.e. CSP and GCM in detail. Next, various applications of an M/EEG-based BAPD system are provided in Section 2.6. Furthermore, current outstanding issues in the field of M/EEG data analysis and pattern recognition are presented in Section 2.7. Finally, Section 2.8 summaries this chapter.

- **Chapter 3** undertakes an empirical evaluation of the effect of the current available referencing schemes and SL methods on single-trial classification of EEG signals. This chapter is organised as follows: Section 3.1 introduces this chapter. Section 3.2 provides a detailed description of the EEG dataset and the algorithms implemented. Section 3.3 and 3.4 present the data processing and analysis pipeline and outcomes of the studies undertaken. Section 3.5 provides a detailed review of the outcomes and impact of the studies undertaken in this chapter. Section 3.6 summaries the findings of this chapter.

- **Chapter 4** aims to address the limitation of low classification accuracies of EEG-based FC features. This chapter is organised as follows: Section 4.1 introduces this chapter. Section 4.2 describes the connectivity methods, the

BCI datasets, data processing and analysis pipelines, and performance evaluation method. Next, Section 4.3 presents the results obtained from the analysis. Finally, the results are discussed in Section 4.4 and Section 4.5 summarises the findings of this chapter.

- **Chapter 5** aims to study the neural mechanisms related to the stroke recovery obtained from BCI-driven robotic hand exoskeleton. In particular, the associations between the estimated brain networks of the RS MEG data and the behavioural outcomes related to stroke recovery are evaluated. This chapter is organised as follows: Section 5.1 introduces this chapter. Section 5.2 provides the detailed description about the participants, rehabilitative intervention, assessment of hand functional recovery, and acquisition and connectivity analysis of RS MEG data. Section 5.3 illustrates the outcomes of the hand functional recovery assessment and the RS MEG connectivity analysis. Section 5.4 provides a detailed review of the outcomes and impact of the studies undertaken in this chapter. Section 5.5 concludes the chapter.

- **Chapter 6** presents a summary of the work performed in the previous chapters along with their limitations, and new directions for future work are proposed.

1.3 Publications

The research work undertaken in this thesis is published in following peer-reviewed articles:

Journals publications

- **Rathee, D.**, Raza H., Prasad G., Cecotti H. (2017) "Current source density estimation enhances the performance of motor-imagery related Brain-computer interface." *IEEE Transactions on Neural Systems and Rehabilitation Engineering*, 25(12), pp. 2461-2471. **Rathee et al. 2017a**

- **Rathee, D.**, Cecotti. H., Prasad G. (2017) "Single-trial effective brain connectivity patterns enhance discriminability of mental imagery tasks." *Journal of Neural Engineering*, 14(5), 056005. **Rathee et al. 2017b**

- **Rathee, D.**, Meena, Y. K., Chowdhury. A., Dutta, A., McDonough S., and Prasad, G. (2018) "Brain-Machine Interface Driven Post-stroke Upper-limb Functional Recovery Correlates with Beta-band Mediated Cortical Networks." *IEEE Transactions on Neural Systems and Rehabilitation Engineering*, (under editorial review). **Rathee et al. 2018a**

Conferences publications

- **Rathee, D.**, Meena, Y. K., Chowdhury. A., Dutta, A., McDonough, S., and Prasad, G. (2018) "Functional whole-brain connectivity using magnetoencephalography to identify the neuro-biomarkers of BMI driven stroke recovery." *Conference Abstract: The 21st International Conference on Biomagnetism (Biomag 2018)*, Philadelphia, US. **Rathee et al. 2018b**

- **Rathee D.**, Cecotti. H., Prasad G. (2018) "Current source density estimates improve the discriminability of scalp-level brain connectivity features related to motor-imagery tasks." *Engineering in Medicine and Biology Society (EMBC),* 40^{th} *Annual International Conference of the IEEE* (in press). **Rathee et al. 2018c**

- **Rathee D.**, Cecotti. H., Prasad G. (2016) "Estimation of effective fronto-parietal connectivity during motor imagery using partial granger causality analysis." *Neural Networks (IJCNN), IEEE International Joint Conference on*, pp. 2055-2062. **Rathee et al. 2016a**

Other relevant peer-reviewed publications that are not included in this thesis are following:

Journal publications

- Raza H., **Rathee D.**, Zhou S., Cecotti. H., Prasad G. (2018) "Covariate shift estimation based adaptive ensemble learning for handling non- stationarity in motor-imagery related EEG-based Brain-computer interface." *Neurocomputing* (in press) **2018**. **Raza et al. 2018d**

Conference publications

- **Rathee D.**, Cecotti. H., Prasad G. (2018) "Classification of propofol-induced sedation states using brain connectivity analysis." *Engineering in Medicine and Biology Society (EMBC),* 40^{th} *Annual International Conference of the IEEE*, (in press). **Rathee et al. 2018e**

- **Rathee D.**, Cecotti. H., Prasad G. (2017) "Propofol-induced sedation diminishes the strength of frontal-parietal-occipital EEG network." *Engineering in Medicine and Biology Society (EMBC),* 39^{th} *Annual International Conference of the IEEE*, pp. 4463-4466. **Rathee et al. 2017c**

- **Rathee D.**, Cecotti. H., Prasad G. (2017) "Functional Connectivity Networks and Tangent Space Analysis Efficiently Discriminate Distinct Levels of Propofol-induced Sedation." *Conference Abstract:* 8^{th} *Annual Translational Medicine (TMED8) Conference*, Londonderry, UK. **Rathee et al. 2017d**

- **Rathee D.**, Cecotti. H., Prasad G. (2017) "Comparing Cognitive and Motor Imagery Features for Classification of MEG Responses." *Conference Abstract: MEG-UK 2017*, Oxford, UK. **Rathee et al. 2017e**

- **Rathee D.**, Cecotti. H., Prasad G. (2016) "Effective connectivity analysis in fronto-centroparietal network during altered levels of consciousness." *Front. Neuroinform (58), Conference Abstract: Neuroinformatics 2016*, Reading, UK. **Rathee et al. 2016b**

- **Rathee D.**, Cecotti. H., Prasad G. (2016) "(Un)Consciousness and Time-Series Complexity: A study with spontaneous EEG." *Conference Abstract: MEG-UK 2016*, Yorkshire, UK. **Rathee et al. 2016c**

Chapter 2

Computational modelling and EEG/MEG data analysis for single-trial brain activation pattern detection: A review

2.1 Introduction

Computational neuroscience has seen a revolutionary change with the introduction of practical methods to non-invasive imaging that provides immense support in the development of a functional and structural understanding of the neural system. Functional neuroimaging methods provide a means of evaluating local changes in brain activity and can be performed on healthy (normal) as well as diseased (compromised) brains [1, 2, 3]. Several functional neuroimaging methods are currently available, including those based on a hemodynamic measure (e.g. functional magnetic resonance imaging (fMRI)) and those based on electrophysiological and associated mechanisms of the brain (e.g. electroencephalography (EEG) and magnetoencephalography (MEG)). As the focus of this thesis is on these latter two methods – EEG and MEG, this chapter will further concentrate on the computational analysis and modelling of the data

generated by these two approaches. The electric currents in the synchronously-active neural population cause generation of electric potentials [4] and magnetic fields [5] which can be measured non-invasively using EEG and MEG, respectively. With EEG being able to record neural activities from both tangential and radial brain sources and MEG having higher sensitivity to tangential sources, the two methods are complementary to each other. Both neuroimaging techniques have developed into widely used quantitative diagnostic tools in the analysis of brain signals and patterns. EEG and MEG potentially contain a rich source of information related to the functional, physiological, and pathological status of the brain. In particular, they are extremely useful for the diagnosis and monitoring of brain activity and offer not only the functional but also pathological, physiological, and metabolic changes within the brain and implicitly other body parts.

A considerable amount of signal processing is involved in computational modelling and analysis of the M/EEG data, e.g. signal-to-noise ratio (SNR) enhancement (also known as pre-processing), feature extraction, source localization, automated classification, hidden information extraction (pattern detection), and dynamic modelling. These involve a variety of signal processing methods, e.g. surface Laplacian (SL), signal-space projections, principal/independent component analysis (PCA/ICA), temporal/spatial filtering, and machine learning approaches. This chapter will provide a systematic discussion on several topics related to this field of research. First, Section 2.2 provides a brief introduction of the anatomical and physiological aspects of the human brain along with EEG and MEG neuroimaging technologies. Second, various steps involved in a single-trial brain activation pattern detection (BAPD) system using M/EEG data are described in Section 2.3. Third, current referencing schemes and SL approaches for EEG data are presented in Section 2.4. Fourth, Section 2.5 describes two state-of-the-art M/EEG feature extraction methods i.e. common spatial pattern (CSP) and Granger causality modelling (GCM) in detail. Next, various applications of an M/EEG-based BAPD system are provided in

Section 2.6. Furthermore, current outstanding issues in the field of M/EEG data analysis and pattern recognition are presented in Section 2.7. Finally, Section 2.8 summarises this chapter.

2.2 Functional neuroimaging methods

There are several brain imaging methods to study physiological (functional) patterns of the human brain, e.g. fMRI, positron emmision tomography (PET), single positron emission computerised tomography (SPECT), EEG, local field potentials (LFPs), electrocorticogram (ECoG), MEG, and near-infrared spectroscopy (NIRS). Apart from these, there are other brain imaging techniques involving methods like radiolabelling, histological, or optical imaging techniques. Noninvasive M/EEG neuroimaging offers two unique attractions, namely high time resolution in the millisecond range and direct access to neuronal signalling rather than the indirect metabolic signals picked up by fMRI, PET, and NIRS. This section focus on the two neuroimaging techniques, i.e. EEG and MEG. In particular, the focus is on how, why, and where the brain generates electrical/magnetic activities that can be recorded noninvasively on the scalp.

2.2.1 Human brain

The brain, one of the most complex human body organs, constitutes more than 100 billion nerve cells (primary neuronal body) which are interconnected by specialised structures known as synapses. The healthy human brain remains plastic during the entire lifespan, allowing the individual to keep gathering and remembering information and to learn new skills.

Different brain regions are connected to other parts of the brain as well as to the sensory and motor periphery by axonal fibres that form the brain's white matter due to its visual appearance of white colour myelin sheets. The anatomy of the human brain includes two major structural regions, namely cortical area (cerebrum) and subcortical areas (thalamus, brainstem, and cerebellum) as

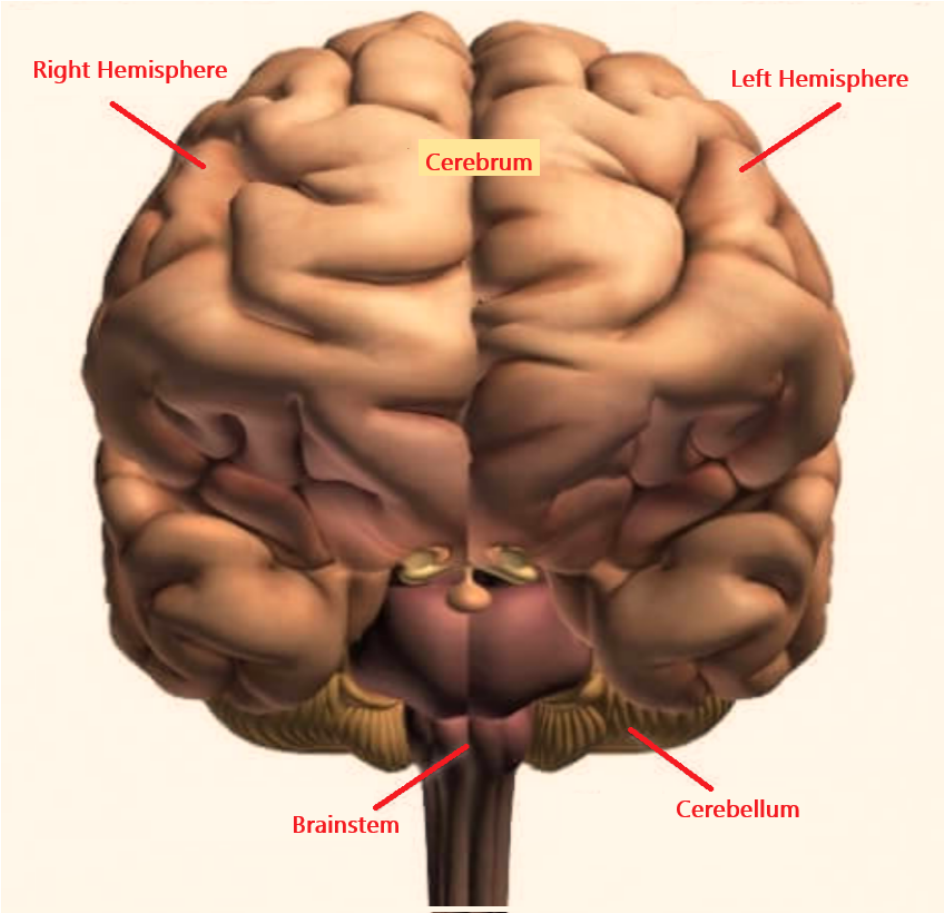

Figure 2.1: Major anatomical regions of Human Brain

illustrated in Fig. 2.1. A brief description related to the structural and functional aspects of the parts mentioned above of the brain is provided below.

- The cortical area consists of the two paired cerebral hemispheres (see Fig. 2.1). Each hemisphere is covered with cortex, a structure that varies in thickness in different regions from about 1.5 to 4.0 mm. The cortex is known colloquially as grey matter because of the colour imparted by its large number of neurons. The cerebral cortex has four major parts, or lobes, namely frontal, parietal, occipital, and temporal. The frontal and parietal lobes are separated by the central sulcus, which is a deep groove between the cortical folds (called gyri). The frontal lobe lies on the anterior of the central sulcus, and the parietal lobe lies on its posterior side. The frontal lobe is involved in higher-order executive functions including complex

cognitive behaviours, personality, and decision making. Parietal lobe is responsible for sensation (e.g. pain, touch), sensory comprehension, recognition, perception of stimuli, orientation, and movement. The occipital lobe, at the posterior pole of the brain, consists primarily of visual areas and is responsible for visual processing. The temporal lobes are located ventrally along the sides of the brain. They are critical for auditory signal processing, higher-level visual processing, and memory.

- The major subcortical areas of the brain that interact with the cortex and are intimately involved in motor and sensory function include thalamus, brainstem, and cerebellum. The thalamus is located below the cortex and deep within the cerebrum. It serves as the primary gateway to the cerebral cortex for sensory inputs from the spinal cord and other subcortical structures including basal ganglia and cerebellum. The brainstem is at the base of the brain and consists of the midbrain, pons, and medulla oblongata. The cerebellum is nestled under the posterior part of the cerebral hemispheres. The cerebellum is involved in the production of smooth, coordinated movements as well as in motor learning and adaptation.

2.2.2 Electroencephalography

EEG has its earliest beginnings in the 1930s as a tool of clinical diagnostics after Hans Berger, a psychiatrist from Germany, recorded the electrical activity originated by the human brain for the first time [4]. The widespread clinical use of EEG began by visual inspection of the spontaneous EEG activity in patients suffering from various neurological disorders, particularly epilepsy.

EEG signals are recorded as potential differences, and their measurement requires both a recording electrode and a reference electrode (see Fig. 2.2 (A)). Typical EEG scalp electrodes are circular plates of metal that, when coupled to a conductive medium, provide a good low-resistance path between the scalp and EEG amplifier.

Suppose $V(r,t)$ is an unknown scalp potential. Each EEG channel records an

experimental scalp potential that depends on a pair of scalp electrode locations (r_n, r_R). In standard EEG parlance, reference recordings involve choosing some fixed location r_R , typically an ear, mastoid, or neck site, and recording all potentials with respect to this fixed site. Apart from fixed reference montage, EEG can also be acquired in bipolar setting which involves recording of potential difference between two nearby electrodes both of which are presumed to be changing in potential. These recordings are not fundamentally different from referenced recordings, except that bipolar recordings acknowledge the presence and influence of the reference electrode explicitly. The process of EEG recording is further described in Section 2.3.1.

2.2.3 Magnetoencephalography

In addition to the generation of electrical signals, brain-current sources can also generate an external magnetic field in the order of femto− and pico−Tesla (1 fT = 10^{-15} Tesla and 1 pT = 10^{-12} Tesla). MEG is a neuroimaging technique, pioneered by [30], that uses an array of sensors located around the head that are extremely sensitive to minuscule changes in these magnetic fields resulted from corresponding changes in the electrical activity within the brain (see [31], for a detailed review).

As the typical MEG signal is of the order of 100 fT and thus a mere 10^{-8} times the strength of the Earth's steady magnetic field, the best-quality MEG recordings are carried out inside magnetically shielded rooms. The most commonly used MEG sensors are SQUIDS (Superconducting quantum interference devices), which do not make direct contact with the head as they are immersed within the vacuum-insulated liquid-helium dewar. The magnetic fields emanating from the head induce current flows in the SQUIDs. They combine the physical phenomena of flux quantisation and Josephson tunneling [32, 33]. The circuit associated with the SQUID functions as a flux-voltage amplifier, transforming the magnetic flux sensed by the SQUID to a voltage readable by the computer. The essential property of the SQUID is that a steady increase in the magnetic flux threading the

loop causes the critical current to oscillate with a period of one flux quantum. In today's SQUIDs, using conventional semiconductor readout electronics, one can typically detect a change in magnetic flux corresponding to 10^{-6} times the magnetic flux quantum(2.07 x 10^{-15} Tm^2) in one second [34, 35]. This allows the current MEG systems to have a high temporal resolution. The primary source currents of both MEG and EEG arise in the cortical pyramidal neurons, which can be radial (perpendicular to the cortical surface) and tangential (see Fig. 2.2 (B)). EEG measures the voltage difference between different parts of the scalp and is most sensitive to the superficial radial currents.

However, MEG signals majorly represent the tangential currents generated by the neuronal population present in the walls of cortical fissures. This is an advantage over EEG, as about two-third of the cerebral cortex is located within fissures that are difficult places to reach even with the intracranial recordings. Moreover, as the magnetic fields are insensitive to the inhomogeneities of the intervening tissues between cortical surface and sensor array, MEG signals are less distorted than EEG signals. An additional significant difference between MEG and EEG is that EEG recordings measure the voltage between two recording sites whereas MEG recordings provide information on the magnetic flux or its gradient precisely at the measurement site. Moreover, EEG is more susceptible to muscle artefacts than MEG as the EEG electrodes are placed in direct contact with the scalp surface. The process of MEG recording is further described in Section 2.3.1.

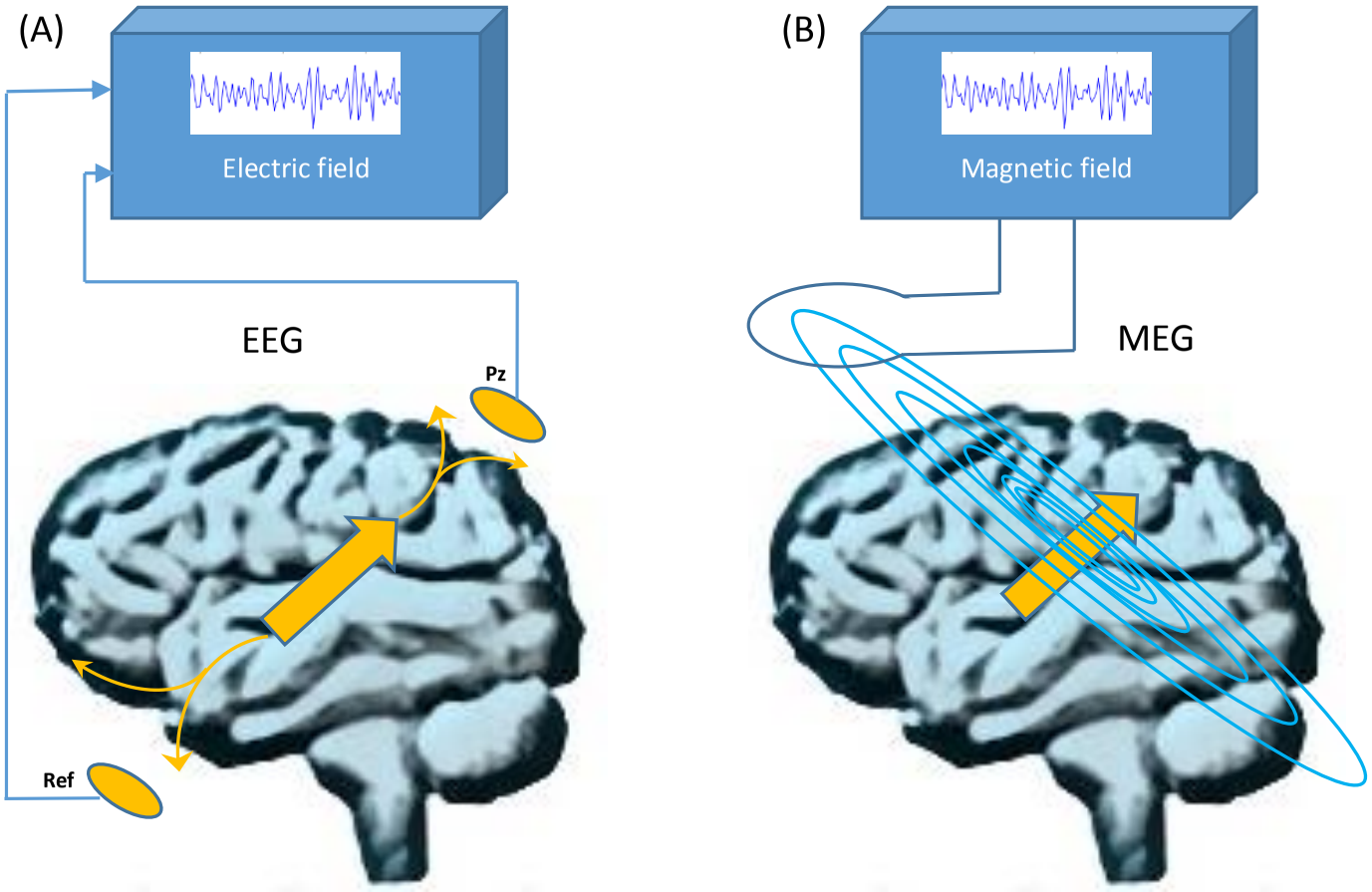

Figure 2.2: Schematic diagram representing EEG and MEG recording mechanisms.

Current advancements towards future MEG systems are majorly focused on development of novel MEG sensors. High-transition-temperature (High-T_c) SQUIDs could be applied to MEG with much reduced thermal shielding and thus shorter distance from the brain compared to the current liquid-helium-cooled SQUIDs [36]. However, the sensitivity of high-T_c SQUIDs is still clearly inferior, and although the reduced distance to brain means larger signals, improvements in sensitivity are needed for high-T_c SQUIDs to be on a par with their low-T_c cousins, high-T_c SQUIDs hold promise for an adjustable high-resolution MEG array [36, 37].

Optically-pumped magnetometers (OPM), based on magnetic-field-induced polarization rotation in an alkali-metal vapor, have demonstrated sensitivities approaching those of low-T_c SQUIDs. MEG with chip-scale OPM sensors has been demonstrated [38]. Such sensors would enable construction of a multi-channel MEG system with an individually-adjustable array, where the sensors are within millimeters from the scalp. A new generation portable OPM sensors are presented recently to allow room temperature recording [39].

Both high-Tc SQUIDs and OPMs would remove the problems related to liquid helium. However, zero helium boil-off MEG systems have been introduced recently [40]. This development clearly enhances the usability of MEG in hospitals, as the need for frequent transfers of liquid helium, requiring expertise and personnel, is eliminated.

2.3 A conventional signal processing and analysis pipeline of M/EEG data

Fig. 2.3 depicts various steps involved in a typical M/EEG signal processing and analysis pipeline for single-trial BAPD. In subsequent subsections, each of these steps are described in detail.

2.3.1 Data acquisition

EEG recording:

EEG recording involves electrodes for at least three different purposes, namely grounding, referencing, and recording. Fig. 2.2 (A) depicts EEG recording from a human subject who is conductively isolated from the ground of the power supply. The ground electrode is connected to the amplifier ground, which is isolated from the ground of the power supply. As described in Section 2.2.2, potential differences $V_1(t) - V_R(t)$ measured on the scalp are generated by brain current sources $P(r,t)$ (current dipole moments per unit volume) and by biological artefacts.

Environmental electric and magnetic fields can also generate scalp potentials, mostly due to capacitive coupling of body and electrode leads to ambient electromagnetic fields (e.g. from power lines and other electric equipment). EEG systems use differential amplifiers, which are designed to amplify the potential difference between pairs of scalp locations such that the output voltage E(t) is proportional to scalp potential differences generated within the body [41], that is,

$$E(t) \quad = \quad A\,[V_1(t) - V_R(t)] \tag{2.1}$$

where A is the total system gain typically due to several amplifier stages. The ground electrode that is placed on the scalp, nose, or neck provides a reference voltage to the amplifier to prevent amplifier drift.

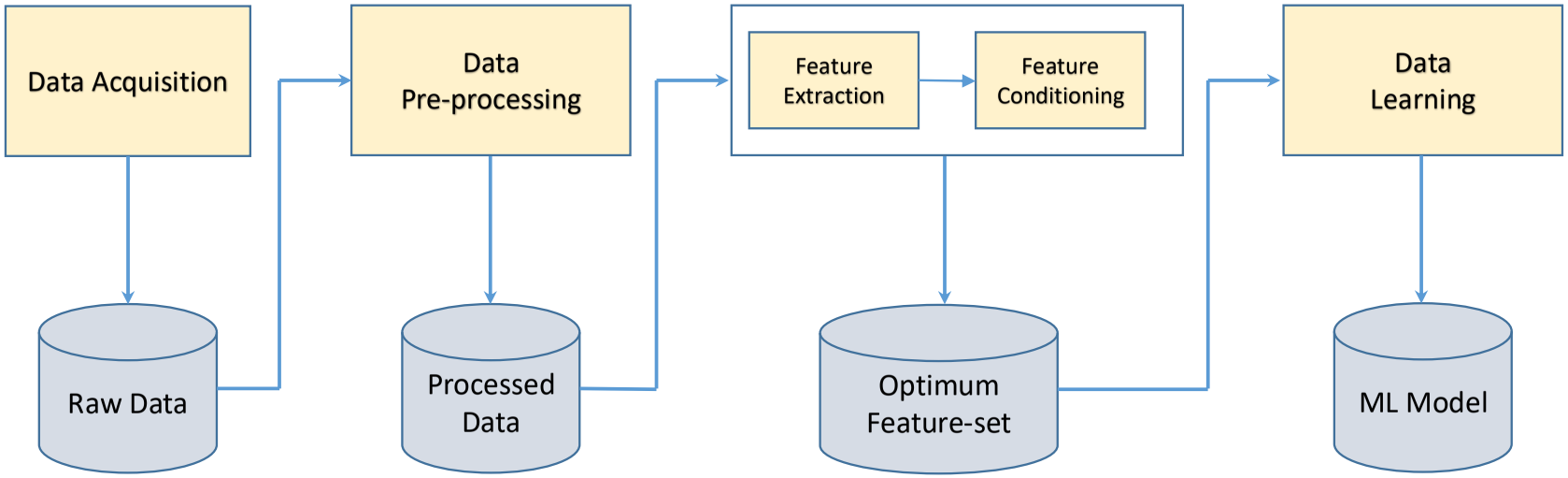

Figure 2.3: Schematic diagram representing a conventional signal processing and analysis pipeline of M/EEG data.

Traditional EEG practice provides guidelines for contact impedance, typically requiring impedance of less than 10 $K\Omega$ [42]. This can be achieved by abrading the scalp at the electrode site and using a conductive gel or paste between the electrode and the scalp. Another option is using sponge-saline electrodes instead of using conductive gel. When using modern amplifiers that have large input impedances (e.g. 200 $M\Omega$), electrode contact impedances of $30-50$ $K\Omega$ (relatively large compared to traditional guidelines) can easily be tolerated without degrading EEG quality [43]. The only noticeable effect is to increase power-line artefacts at 50 Hz (Europe, Asia, Africa, Oceania) or 60 Hz (North and South America), which can easily be removed from the data by using online analog filters or by offline processing with digital filters. Most commercial EEG electrode systems use Ag/AgCl electrodes. Au electrodes also minimise drift and show less high-frequency noise than Ag/ AgCl electrodes. Conductive-gel and sponge-saline electrodes are often referred to as wet electrodes. Because of the inconvenience and messiness of the typical electrode gels and the short useful lifespan of the electrode saline solutions, there has been much interest in recent years in developing dry electrodes, electrodes that do not require the low-impedance contact with the scalp that gel and mild skin abrasion provide to wet electrodes. The sensor material of a dry electrode can be an inert metal (e.g. platinum, gold, or stainless steel) or even an insulator. Whichever material is used, there is generally a capacitive coupling between the skin and the electrode [44, 45, 46, 47].

In most EEG practice, the potentials at all the other (typically $32-256$) electrodes are recorded with respect to one electrode selected as the reference electrode. Any particular choice of reference placement has advantages and disadvantages that depend on the locations of the sources generating the EEG signals. The positions of the electrodes are referred to collectively as the electrode montage. In practice, these vary considerably across laboratories. Standard electrode-placement strategies use the International $10-20$, $10-10$, and $10-5$ placement systems shown in Fig. 2.4 [48]. These montages are based

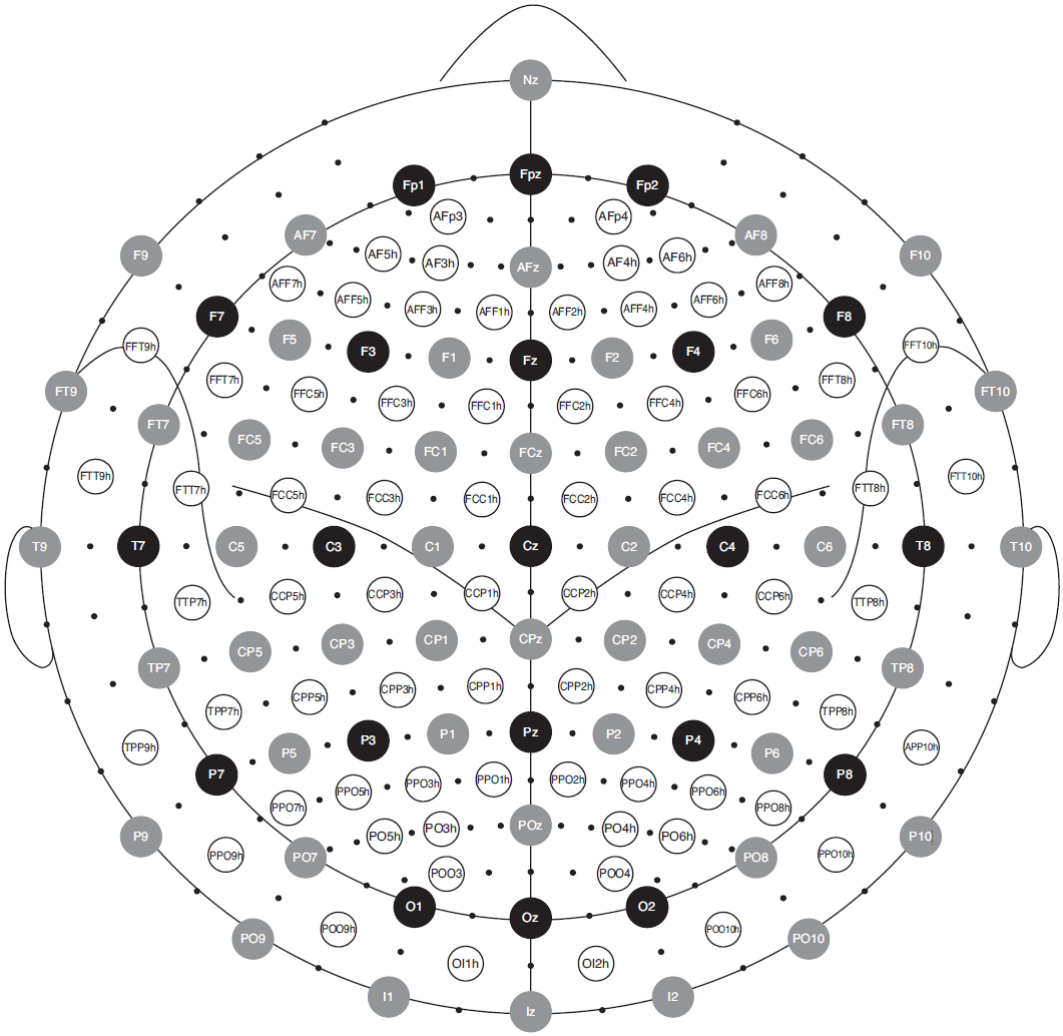

Figure 2.4: The standard 10−20, 10−10, and 10−5 electrode montages. The 10−20 montage is indicated by the 21 electrodes shown as black circles. The 10−10 montage (in total 74 electrodes) consists of the 21 electrodes of the 10−20 montage (black circles) plus 53 additional electrodes indicated in gray. The additional electrodes of the 10−5 montage are indicated by the black dots and the open circles. The 68 open circles and the 74 10−10 electrodes together comprise a 142-channel montage that provides a more complete and homogeneous coverage of the head. The nomenclature for the standard 10−20 and 10−10 and 10−5 extensions is indicated.

on systematic extensions of the standard clinical EEG 10−20 electrode montage [49], and they are widely (but not universally) used. The basis of these standard electrode placements is to define contours between skull landmarks (e.g. nasion and inion) and to subdivide the resulting contours in proportional distances. The standard 10−20 system uses proportional distances of 20% of the total length along contours between skull landmarks, whereas the 10−10 and 10−5 systems use 10 % and 5 % distances, respectively. Fig. 2.4 shows the standard 10−20 system consisting of 21 electrodes indicated by black circles.

MEG recording:

MEG methods record the small magnetic field generated by the brain using a SQUID magnetometer. SQUID devices were first used to detect the magnetic field of the brain in the 1970s [50] and are sensitive detectors of magnetic flux (see Fig. 2.2 (B)). When compared to EEG recording, MEG has several advantages and disadvantages. The spatial resolution of MEG decreases rapidly as a function of the depth of the brain sources [51]. Thus, the detectability of deep brain structure activities is still an open question [52, 53, 54]. Moreover, as the magnetic fields associated with the brain current sources are very small relative to the ambient magnetic field variations that are outside experimental control (e.g. fluctuations in the Earth's magnetic field), MEG recordings are performed in a specially shielded chamber, usually made of high-permeability mu-metal [31]. Superconductivity is essential to the function of the SQUID coils, so the coils are maintained at very low temperatures in a helium-containing insulated (Dewar) chamber. The main practical effect of this elaborate system is that the measurement point is about 1−2 cm above the scalp surface. This substantial distance from the sources of brain activity reduces spatial resolution significantly. Individual SQUID coils, called magnetometers, can be arranged in different configurations to accommodate different purposes. The most straightforward configuration is a single magnetometer.

An array of 100−200 magnetometers can provide coverage of the entire head. Each one detects only the radial component of the magnetic field generated by

brain sources. Another common coil configuration is an axial gradiometer, which consists of a pick-up coil and a compensation coil located above the pick-up coil. The two coils are wound in opposite directions to cancel noise produced by non-brain magnetic fields. Although both the simple magnetometer and the axial-gradiometer coil configurations have spatial resolution comparable to (but sometimes poorer than) EEG [55, 56, 57], they are both more sensitive than EEG to a particular subset of sources. Whereas EEG detects activity from both tangential and radial sources, MEG is sensitive to sources oriented tangentially to the detectors and is blind to sources pointed radially [12]. This property of MEG is identically valid in spherical models of the head and is approximately valid in realistic models that include the fields produced by return currents. MEG's preferential sensitivity for tangential sources has particular value in studies of primary sensory areas of the brain that are located in sulcal folds oriented tangentially to the MEG coils [31]. This preferential sensitivity to tangential sources accounts for the main practical distinction between EEG and MEG.

A recently developed MEG system implements a planar gradiometer; it consists of two adjacent coils (with parallel axes) wound in opposite directions. This configuration measures the gradient of the radial component of the magnetic field in one direction. The planar gradiometer strategy is similar to the bipolar EEG recording strategy and imparts to MEG a potentially much higher spatial resolution than is possible with conventional MEG. However, planar gradiometers only offer a real-world spatial-resolution advantage over axial gradiometers if they are used with a high-enough packing density in a the sensor helmet.

A major advantage of MEG over EEG is that MEG provides a true field measure at a specific point, whereas EEG measures the potential difference between two points on the head. Thus, MEG does not require the choice of a reference sensor. Reference selection is a critical factor in EEG recording since an improper choice can result in data that are misleading or even entirely useless. Furthermore, MEG is less distorted by the head openings and other tissue inhomogeneities that can distort EEG because current follows the paths of lowest resistance, such

irregularities may cause EEG electrodes to record substantial scalp currents produced by sources located far from the recording sites. These and other considerations such as SNR and electrode density must be taken into account when assessing the relative advantages and disadvantages of EEG and MEG for a particular application. Other practical issues, such as temporal filtering and analogue-to-digital conversion (ADC) are identical for EEG and MEG.

2.3.2 Data pre-processing

The first step of feature extraction is called signal conditioning or pre-processing. This step enhances the signal by pre-emptively eliminating known interference (i.e. artefacts) or irrelevant information, and/or by enhancing spatial, spectral, or temporal characteristics of the signal that are particularly relevant to the application. It is common to have some prior knowledge about the general signal characteristics relevant for a particular application, and this knowledge is used in pre-processing. Signal pre-processing can include a number of different procedures that can primarily be categorised as:

Referencing and surface Laplacian: These methods are primarily data-independent as their implementation is based on the fixed geometrical relationships to determine the transformation weights and thus are not dependent on the data being filtered [20]. These methods have certain local or global characteristics that, although somewhat generic, can be extremely useful in many applications. McFarland et al. (1997) describe the value of appropriate data-independent filtering for brain-computer interfaces (BCIs) [58]. A common-average reference (CAR) filter is realised by recording all channels with a common reference, computing at each time point the global mean of all the digitised channels, and then subtracting that mean from each channel. This tends to reduce the impact of artefacts that are similar across all channels (e.g. 50/60 Hz power-line interference). A SL filter is based on a computation of the second spatial derivative. If the channels have been recorded with a common reference, this computation is effectively equivalent to taking a central channel of interest

and subtracting the mean of all the channels at some fixed radial distance from this central channel. Although this simplified Laplacian filter is effective and commonly used, more elaborate Laplacian filters can be constructed based on the precise spatial-derivative derivation such as spline surface Laplacian (SSL) with finite-distance method (SS_F) [59], Hjorth Laplacian [14], and SSL with realistic head geometry (SS_R) [17]. Spatially adjacent channels tend to be highly correlated since they have similar positions relative to many brain sources. By eliminating this correlated activity, a Laplacian filter emphasises highly localised activity (i.e. an activity that is not the same at both locations). Thus, the fixed radial distance of the filter should be set based on the spatial characteristics of the activity of interest. A detailed description of the state-of-the-art referencing and SL filtering methods is provided in Section 2.4.

Frequency-range pre-filtering: Signals are often pre-filtered to eliminate frequencies that lie outside the frequency range of the brain activity most relevant to the application. Depending on the application and the available hardware, this pre-filtering can be performed before or after the signal is digitised. For example, because the observed signal power in EEG decreases as 1/frequency and the skull and scalp tissue provide additional signal attenuation, scalp-recorded EEG frequencies above 80 Hz have a very low SNR and thus may not be very useful for BAPD applications. However, for MEG, as the signal attenuation is not very prominent, higher signal frequencies can be utilised. Additionally, low-frequency drift produced by the amplifier is sometimes present in M/EEG and can distort signal visualisation. As a result, it is common at the beginning of M/EEG feature extraction to apply a highpass filtering at 0.5/0.1 Hz. In general, the width of the filter should be set conservatively to prevent unnecessary loss of information, which can also be beneficial for offline analysis of the signals.

Data decimation and normalisation: If the signal is digitised at a rate that is higher than the Nyquist rate required to capture the relevant activity, it may be advantageous to decimate the sampled signal to the minimum effective sampling rate for more efficient processing and storage. Decimation is the elimination of

samples in a periodic fashion. For example, the decimation of a signal by a factor of two will eliminate every other sample, effectively halving the sampling rate and the length of (i.e. the number of samples) the signal. However, just as with sampling in analogue-to-digital conversion, it is essential to avoid aliasing. To avoid aliasing, the signal should be low-pass filtered before decimation, with a cut-off frequency equal to one-half of the decimated sampling frequency.

The signal normalisation can be useful when one is comparing different signals that have differences in mean values, or dynamic (i.e. amplitude) ranges that are not relevant to the particular application. For example, EEG signals recorded over two brain areas often differ markedly in amplitude range, but if the signal dynamics within these ranges may be of primary interest for a given application and not the actual difference in the respective signal amplitude values, signal normalisation can be implemented. The most common way to normalise a set of signals is to subtract from each signal its mean value and then scale the resulting signals by dividing by its standard deviation. Normalisation can also be used to adjust signals that are affected by unintended electrode impedance differences. By converting the signals to the same scale, normalisation can potentially simplify the analysis and interpretation of the signals and the subsequent processing steps.

Removal of environmental interferences and physiological artefacts: Environmental interference is an artefact in brain-signal recordings not attributable to biological sources. It includes interference from environmental factors such as power-lines or other electrical/magnetic sources in the environment. This issue is highly prominent in case of MEG signal acquisition, as the brain magnetic fields are very minute (in range of 10^{-12} to 10^{-15} T) and can easily be distorted by environmental magnetic noise. Various denoising methods can be used to remove these inferences, e.g. a bandstop (or notch) filter at 50/60 Hz and its harmonics, signal-space separation (SSS), signal-space projections etc.

Physiological artefacts from sources such as the eyes (electrooculographic) (EOG), heart (electrocardiographic) (ECG), and muscles (electromyographic) (EMG) arise because these organs also rely on electric signalling, generating

current, and voltage differences that can significantly interfere with M/EEG signals [60, 61]. EMG activity is electrical activity produced by muscle contractions. It is typically manifested as a spectrally broadband activity that often varies substantially from moment to moment. EOG activity is the electrical activity generated by eye movements. For obvious reasons, this interference tends to be prominent in frontal M/EEG activity. Similarly, eye blinks create a large transient frontal pulse that can also affect more posterior channels. In EEG recording, EMG is typically the most significant artefact because it is often difficult to remove or even to fully recognise. Various signal processing methods such as ICA, PCA, SSS can be implemented to remove these artefacts.

2.3.3 Feature extraction and conditioning

After the initial signal conditioning step has optimised the signal by enhancing its most relevant features and/or reducing artefacts, the next step of signal processing measures or extracts the chosen features. This section introduces the process of feature extraction with emphasis on methods widely used and/or particularly appropriate for BCI applications. The methods are described in terms of processing a single channel, but they can be generalised to multiple channels. Measuring brain activity through EEG leads to the acquisition of a significant amount of data. To obtain the best possible performances, it is necessary to work with a smaller number of variables which describe some relevant properties of the signals. These variables are known as “features”. Features are generally aggregated into a vector known as a “feature vector” [62]. Thus, feature extraction can be defined as an operation which transforms one or several signals into a feature vector. The feature vector, which is comprised of the set of all features used to describe a pattern, is a reduced dimensional representation of that pattern.

The distributions and the relationships among the features can have a significant effect on the performance of the learning algorithm that follows feature extraction. These effects depend on the characteristics of the particular

learning algorithm. This section reviews common methods of feature-conditioning that can improve the performance of particular learning algorithms.

In signal conditioning, signal normalisation is commonly accomplished by subtracting the signal mean and scaling the signal amplitude to have unit variance (i.e. variance equal to 1). Likewise, features can also be normalised. Feature normalisation is advantageous when the features comprising a feature vector display differences in their means or dynamic ranges that are not relevant to a particular brain task. For example, the derivation of feature weights for a multiple-regression algorithm can be very sensitive to differing feature magnitudes. Features of greater magnitude will tend to dominate the results, even if their greater magnitude has no bearing on their usefulness.

Some feature-learning algorithms, such as Fisher's linear discriminant achieve optimum results when the input features have Gaussian distributions. Input features often are not natively Gaussian-distributed. For example, a feature defined as the magnitude of an FFT amplitude bin will likely not have a Gaussian or symmetric distribution since the lower range of the feature is bounded by zero and the upper range is unbounded. Moreover, the power of the EEG frequency spectrum is inversely proportional to frequency. In many cases, unimodal non-Gaussian distributed features can be shaped efficiently to be more Gaussian by applying a monotonically increasing nonlinear transformation. A monotonically increasing transformation guarantees that the transformed feature variables will have the same ordering as the original values with different spacing between the values.

Although specialised transforms can be derived for shaping known feature distributions into more Gaussian distributions, the simple log-normal transform shown below has proved useful for transforming a variety of general unimodal distributions to be more Gaussian. This transform is especially useful for M/EEG because it compensates for the decrease in power with increasing frequency and thus creates a more symmetric distribution. When the extracted features are

highly correlated, PCA and ICA can be applied to decorrelate the features, and/ or reduce the dimensionality of the feature vector. Effectively reducing the dimensionality of the feature vector can greatly simplify the training and effectiveness of the learning algorithm, particularly when few observations are available for training the learning algorithm.

2.3.4 Feature learning

As the extracted features represent indirect representations of the task/event specific mechanisms/states of the brain, they must be learned by the machine learning algorithms to generate appropriate information from them. The core of a learning algorithm is a model, which is a mathematical procedure typically comprised of a mathematical equation, set of equations, and/or mapping mechanism such as a lookup table. The model accepts the feature vector (i.e. the set of features) at a given time instant as its input and processes the feature vector to output appropriate information which can be further used to make decisions. Thus, the goal of the model is to describe the relationship between these features and a specific brain state in a form that is simpler than the data that are actually measured. The value of such a description is that it can be used to convert future observations to appropriate output (i.e. it can be generalised to new data).

The model parameters are commonly selected, or trained (also referred to as learned or parameterised) by using a set of training data. Each unit of training data (i.e. each observation) consists of a feature vector (or training sample) and its correct (i.e. intended) output (or training label). Through an iterative procedure, called supervised learning, the parameters are repeatedly adjusted until the model translates the feature vectors into output decisions that are as accurate as possible (i.e. as close as possible to the correct output). The accuracy of the model is evaluated with an objective function (also called a cost function or a fitness function). For instance, a common objective function is a mean-squared error (i.e. difference) between the model output and the correct output: the smaller this error, the more accurate the model. During the supervised learning

process, the feature vectors (i.e. the training samples) are processed by the model with some initial parameters (selected randomly or using a priori information), the objective function then compares the model outputs to the correct outputs (i.e. the training labels), and the model parameters are then updated based on the objective function; finally, the process is repeated until stopping criteria are satisfied (e.g. the mean-squared error is minimised).

With the fact that these models may have to operate in real time with certain applications such as BCIs, it is not sufficient to develop through post-hoc analysis a model that applies well to a given body of previously acquired data. Instead, the crucial requirement is that the model must apply to new data as well, that is, it must generalise. Its ability to generalise is tested (or validated) using an independent set of observations called testing (evaluation) data. Each unit of testing data (i.e. each observation) consists of a feature vector (i.e. testing sample) and its correct (i.e. intended) output (or testing label). Testing data are used to validate the model after its parameters have been fixed via training. In this validation, the testing data are processed by the model, and the model outputs are compared to the corresponding testing labels by using the same objective function employed for model training or some other measure of model accuracy. This model validation process is essential for evaluating how well a given model generalises to new observations. However, some models and training procedures are prone to overfitting, in which the parameterised model is tuned so precisely to the training data that subtle differences between the training data and the test data prevent it from processing the testing data accurately.

Feature learning models fall into two classes according to whether their outputs are discrete categories or continuous dimensions. Specifically, models are either discriminant functions (also called classification functions) or regression functions [63]. A discriminant function translates the observations (i.e. the feature vectors) into discrete categories of output (e.g. specific mental task). A regression function translates the observations into a continuous variable (e.g. constantly varying consciousness states of the brain). For the two-target (i.e.

two possible outputs) both kinds of models require that a single function is parameterised. However, for the five-target instance (i.e. with five possible outputs), the discriminant model requires that four functions be parameterised, while the regression model still needs that only a single function be parameterised.

2.4 Current referencing schemes and SL methods for pre-processing of EEG data

Scalp-recorded EEG activity can be the basis for non-muscular communication and control application using a BAPD system e.g. BCI [64, 65, 9]. EEG-based communication systems measure specific features of EEG activity (i.e. Brain rhythms) and use the results as control signals. Brain rhythms are not always apparent in 'monopolar" surface recordings, in part due to volume conduction of activity from cortical regions associated with other functions. For example, visual alpha rhythms from posterior regions may be volume conducted to the central electrodes where MI-related brain activities are typically recorded [66]. In addition, there are distinct effects associated with movements of specific body parts, such as the hands or feet. Movement or imagery involving the hand often produces desynchronization over areas associated with that hand and simultaneous synchronization over foot areas [67]. Thus, there may be several brain rhythms associated with movement or imagery of different body parts. Signal processing methods to separate the multiplicity of signals present at any single electrode can enhance the separability of patterns associated with distinct actions.

Section 2.3.2 presented the several ways to pre-process the M/EEG signals to enhance the SNR. In addition, the section covered a brief introduction of various referencing schemes and SL methods. This section provides a detailed description of these method.

2.4.1 Common reference

Scalp EEG signal acquisition systems use differential amplifiers, which take the measurements of two electrodes (i.e. the main channel and a reference channel) as input and generate a signal for the corresponding EEG channel as the difference between the two inputs with subsequent amplification. The choice of input electrodes to each amplifier is known as a montage. Fig. 2.5.A presents a schematic representation of CR method using an electrode grid and a non-scalp reference electrode. The most basic montage is CR, where the potential difference at each electrode in the montage is computed with a common reference, for instance, left mastoid, right mastoid or earlobe.

2.4.2 Common average reference

The CAR scheme can be implemented by subtracting the average potential of all EEG channels from scalp potential of each channel. Fig. 2.5.B presents a schematic representation of CAR method using an electrode grid. The target electrode (represented with red colour) is referenced to the a common average of rest of the electrodes (represented with green colour) present in the montage. The method enhances the SNR by reducing the noise common to all the channels [68]. If the scalp potentials are assumed to be generated by point sources, and the whole head is uniformly covered by EEG channels (symmetrically and equally spaced), the CAR transforms the scalp potential distribution into a zero-mean spatial potential distribution [68].

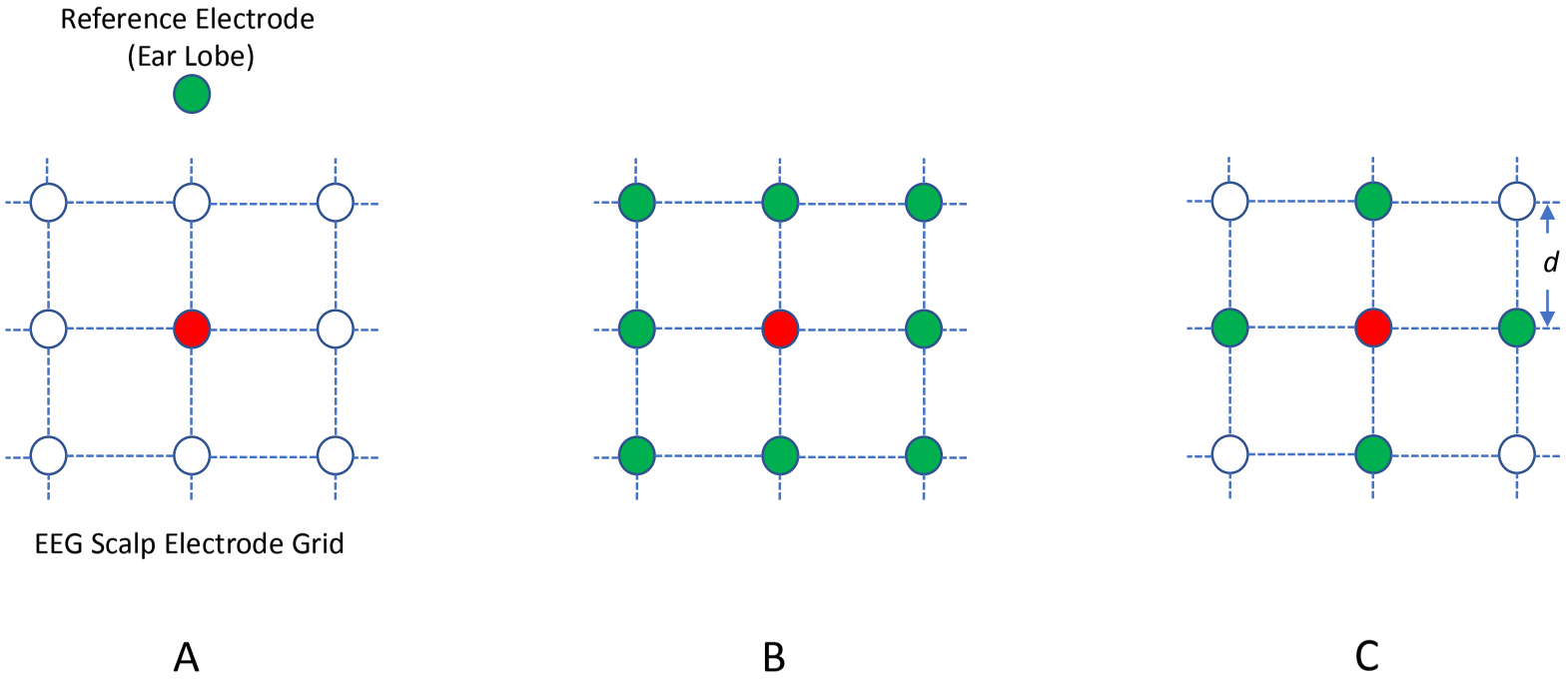

Figure 2.5: Schematic diagram representing various referencing schemes and Hjorth Laplacian method. (A) In CR method, the potential difference at target electrode (red colour) in the montage is computed with a common reference (green colour), for instance, earlobe. (B) In CAR method, target electrode (red colour)) is referenced to all other scalp electrodes (green colour). (C) In Hjorth laplacian method, target electrode (red colour) is referenced to the four next neighboring electrodes (green colour) while taking the distance into account.

Although the assumptions of uniform and complete channel coverage as well as point sources are generally difficult to satisfy in practice, the referencing scheme still provides nearly reference free scalp EEG recordings. The CAR montage can be implemented according to the equation,

$$b_i = a_i - \sum_{j=1}^{N}(a_j/N) \tag{2.2}$$

where $a_i \in \mathbb{R}^{1\times T}$ is the potential difference between i^{th} channel and a common reference, N is the number of channels, and T is the number of time samples in each channel data.

2.4.3 Hjorth Laplacian

The physical interpretation of SL can be provided by the following equation (see [20] for further explanation):

$$Lap_S(a_i) = \frac{\partial^2 a_i}{\partial x^2} + \frac{\partial^2 a_i}{\partial y^2} \tag{2.3}$$

where $a_i \in \mathbb{R}^{1\times T}$ is the potential difference between i^{th} channel and a common reference, and x and y are the Cartesian coordinates of the channel location.

The first Laplacian estimates in the literature were performed by Hjorth (1975), who presented an approximation to Eq. 2.3 based on finite difference estimation [14]. This method is conceptually simple and easy to implement, and for this reason still very popular. Fig. 2.5.C presents a schematic representation of Hjorth method using an EEG scalp electrode grid. The target electrode (represented with red colour) is referenced to the four next neighborhood electrodes (represented with green colour) present in the montage while considering the finite distance between the electrodes.

If the potential is measured in a regular rectangular grid, the SL $L_s(i,j)$ at grid point (i,j) can be estimated by averaging the acquired potentials $a(k,l)$ at the

direct neighbors of (i, j) using:

$$L_s = \frac{1}{d^2}(a_{i-1,j} + a_{i+1,j} + a_{i,j-1} + a_{i,j+1} - 4a_{i,j}) \tag{2.4}$$

where, d is the distance between the nodes in the grid.

Hjorth's estimation is based on two major assumptions. First, the surface of the scalp is locally approximately flat, thus the SL of the voltage at any electrode location can be given by Eq. 2.3. Second, the electrodes are placed at equal distance from each other, thus, forming a rectangular grid. This assumption results in a simple estimation of the SL provided in Eq. 2.4 using finite-difference method [69]. Thus, if the channels have been recorded with a common reference, this computation is effectively equivalent to taking a central channel of interest and subtracting the mean of all the channels at some fixed radial distance from this central channel. These radial distances provide the spatial filtering characteristics of the applied Laplacian. Thus, the Laplacian becomes less sensitive to signals with higher spatial frequencies with increase in the radial distance and vice-versa.

2.4.4 Finite-difference method on a triangulated $3D$ spherical surface

The SS_F method, presented by Oostendorp et al. [59], provides the approximation of SL operator on a triangulated $3D$ spherical surface. Thus, an interpolation for scalar functions on a rectangular grid of a planar surface is extended to the interpolation function on a closed three-dimensional triangulated surface.

Let's consider the SL estimated by a rectangular 2D grid, provided in Eq. 2.4. If the grid of known potential values is irregular, this $2D$ finite-difference method can be replaced by one of the methods proposed by Huiskamp [70], in which the value of the SL at electrode position lo can be estimated from appropriately weighted potential readings of the direct neighbors at positions l_i in a triangular grid, where $i \in \{1, \ldots, M\}$, and M is the number of direct neighbors. This approximation can

be expressed by:

$$L_s = \frac{4}{\bar{r}\eta} \sum_{i=1}^{M} \left(\frac{1-\cos(\phi_i^-)}{\sin(\phi_i^-)} + \frac{1-\cos(\phi_i^+)}{\sin(\phi_i^+)} \right) \cdot \frac{1}{r_i}(a_i - a_0) \tag{2.5}$$

where, r_i is the length of vector $\vec{r}_i = \vec{l}_i - \vec{l}_0$, $\bar{r}$ is the mean value of $\vec{r}_i$ over all M direct neighbors of $\vec{l}_0$. ϕ_i^- is the angle from $\vec{r}_{i-1}$ to $\vec{r}_i$ and ϕ_i^+ is the angle from $\vec{r}_i$ to $\vec{r}_{i+1}$. η is a normalization factor and given as:

$$\eta = \sum_{i=1}^{M} \left(\frac{1-\cos(\phi_i^-)}{\sin(\phi_i^-)} + \frac{1-\cos(\phi_i^+)}{\sin(\phi_i^+)} \right) \tag{2.6}$$

2.4.5 Spline surface Laplacian filtering for realistic head geometry

The SS_R method has the advantage of being readily applicable to the surfaces defined by MRI-based triangular meshes without the help of any intermediate representations, and it does not require any coordinate transformations as well [17]. The implementation of SS_R involves a two-step operation. The first step is to estimate a continuous potential distribution function $F(r)$ using the discrete inputs from various EEG electrode locations using a $3D$ polyharmonic spline interpolation scheme (Eq. 2.7), identical to the spherical spline Laplacian [12].

$$F(r) = \sum_{i=1}^{N} pK_{m-1}^{i}(r) + Q_{m-1} \tag{2.7}$$

where, $K_{m-1}^{i}(r)$ is a polyharmonic radial basis function, Q_{m-1} (osculating polynomial) acts as a smoothing function for the spline, and p is the spline coefficient.

In the second step, the SL operator ∇_s^2 is created over a defined underlying surface, using the Laplace-Beltrami operator ∇^2, which takes the form of the trace

of the function's Hessian

$$L_s(F) = \nabla_s^2(F) = tr\left[\nabla\nabla F\right] \tag{2.8}$$

where, $tr[.]$ is the trace operator.

By explicitly removing the surface normal component from the gradient of the function $F(r)$, the operator is restricted to the surface tangent plane. Further, SL is considered to be the negative of the resulting operator to facilitate visualization and source analysis [12].

$$\nabla_s^2(F) = -tr\left[\nabla(I - n'n)\nabla F\right] \tag{2.9}$$

$$\nabla_s^2(F) = -tr\left[\nabla\nabla F\right] + tr\left[\nabla(n'n)\nabla F\right] \tag{2.10}$$

The second term on the right side of the above equation can be further expanded as,

$$tr\left[\nabla(n'n)\nabla F\right] = n(\nabla\nabla F)n' + n(tr[\nabla n]).\nabla F + (\nabla F)'(\nabla n)n' \tag{2.11}$$

The three expanded terms on the right side of Eq. 2.11 utilise distinct levels of geometrical variations: information of surface normals n, the trace of the curvature tensor ∇n, and the complete form of geometry (i.e. Jacobian matrix of surface normals). Furthermore, for generating analytical expression of the SS_R the surface is discretised using triangular mesh form, where vertices and edges represent the continuous surface geometry.

On a general surface given by a triangular mesh, the interpolation points are defined on the vertices of each triangle. The vertex normal can be generated from the surrounding triangle face normal while the weighting of a particular triangle face normal is set to be inversely related to the face area of that triangle [71]. To estimate the Jacobian matrix at each triangle vertex, the one-ring neighbours of a particular vertex is determined at first, followed by calculation of the finite

difference of vertex positions and unit normal vectors on these vertices.

2.5 Common spatial patterns and Granger causality modelling

This section will cover two important methods of time-series modelling i.e. CSP and GCM. CSP is a mathematical procedure used in signal processing for transforming a multivariate signal (time-series data) into additive sub-components which have maximum differences in variance between two given windows [72]. GCM is a method for identifying directed functional ("causal") interactions from time-series data. These methods have been used in neuroscience previously for assessment of neural patterns associated with both intended and actual motor movements [73, 74].

2.5.1 Common spatial patterns

CSP method was firstly suggested for classification of multi-class MI-related EEG signals by H. Ramoser [75]. The primary idea is to use a linear transform to project the multi-channel EEG data into low-dimensional spatial subspace with a projection matrix, of which each row consists of weights of two-class signal matrices. CSP method is based on the simultaneous diagonalisation of the covariance matrices of both classes.

For effective use of the CSP algorithm, several parameters have to be specified, namely, the frequency for band-pass filtering of the EEG measurements, the time interval of the EEG measurements taken relative to the stimuli, and the subset of CSP filters to be used [76]. Typically, general settings such as the frequency band of 7–30 Hz, the time segment starting 1 s after cue, and 2 or 3 subset of CSP filters are used [76]. However, the performance of the CSP algorithm can be potentially enhanced by subjectspecific parameters [77]. Several approaches were proposed to address the issue of selecting optimal temporal frequency band for the CSP algorithm. These include, but not limited to, the Common Spatio-Spectral Pattern

(CSSP) which optimizes a simple filter that employed a one time-delayed sample with the CSP algorithm [78]; the Common Sparse Spectral-Spatial Pattern (CSSSP) which performs simultaneous optimization of an arbitrary Finite Impulse Response (FIR) filter within the CSP algorithm [79]; and the SPECtrally weighted Common Spatial Pattern (SPEC-CSP) algorithm [80] which alternately optimizes the temporal filter in the frequency domain and then the spatial filter in an iterative procedure.

For the purpose of simplicity, the mathematical background of the basic CSP algorithm is explained in the remaining section. CSP involves the extraction of log variance features of the band-limited M/EEG data after performing spatial filtering using CSP algorithm. The CSP method is highly successful in calculating spatial filters for detecting event-related desynchronisation/synchronisation (ERD/ERS) during MI tasks. The algorithm involves band-pass filtering of the scalp (or sensor) M/EEG signals followed by spatial filtering based on linear transformations that can be represented as:

$$Z_i = W^T E_i \tag{2.12}$$

where $E_i \in \mathbb{R}^{c \times N}$ denotes the band-pass filtered M/EEG signals from the i^{th} trial/segment; $Z_i \in \mathbb{R}^{c \times N}$ denotes the spatially filtered M/EEG data; $W^T \in \mathbb{R}^{c \times c}$ denotes the transpose of the CSP projection matrix; c is the number of channels; and N is the number of time-samples in one trial/segment.

The CSP algorithm computes the transformation matrix W to yield features whose variances are optimal for discriminating two classes of M/EEG measurements. Further, the m pair of CSP filters (i.e. first and last m) are selected as,

$$W_{csp} = (w_1 \dots w_m \, w_{c-m+1} \dots w_c) \tag{2.13}$$

and the filtered signal matrix of the i^{th} M/EEG trial is given by,

$$v_i = W_{csp}^T E_i = \left(v_i^1 \dots v_i^d\right)^T \tag{2.14}$$

where $d = 2m$. Further, the CSP feature vector for i^{th} trial (i.e. $x = (x_1, x_2, \dots, x_d)^T$) can be generated as,

$$x_j = \log\left(\frac{var\left[v_i^j\right]}{\sum_{j=1}^{d} var\left[v_i^j\right]}\right) \tag{2.15}$$

2.5.2 Granger causality modelling

GC analysis is a prediction-based approach that predicts statistical dependencies between a local measurement of neuronal activity and measurements of activity elsewhere in the past [81, 82]. It is a simple yet robust way to characterise the propagation of information along a network of sources. In neuroscience, the standard GC has been applied to various brain data types such as LFP [83, 84, 85], M/EEG/ERP [86, 87, 88, 89, 90, 91], fMRI (BOLD) [92, 93, 94, 95] and spike train [96, 97] data. The estimation in GC measures requires multivariate autoregressive (MVAR) modelling. The MVAR model is an extension of AR model for an arbitrary number of channels and works based on stochastic process theory and stationarity assumption. If the data are initially nonstationary, a range of methods can be considered to fulfill the stationarity assumption. Drifts and slow fluctuations can be removed by detrending (linear or piecewise), differencing, and/or high-pass filtering [98]. Oscillatory nonstationary features like electrical line noise can be removed by notch filtering or other methods. The data can also be windowed into shorter and possibly more stationary epochs [86, 99]. In addition, analysis can focus on limited data segments where stationarity applies. Whereas in most neuroscience contexts some combination of these steps will suffice, if nonstationarities persist, other more sophisticated approaches will be needed [87].

As the MVAR model allowed straight forward z-domain transformation, the GC

measures have been applied both in time- or spectral-domain. Moreover, GC method has been tested and developed for both linear [100, 84, 101] and nonlinear models [99, 102, 103].

In the following sections, the theory of linear MVAR modelling and linear GC in time- and pectral domains are discussed.

2.5.2.1 Multivariate Autoregressive model

An MVAR model for a set of L observed time-sampled series $x(t) \in \mathbb{R}^L$, with $1 \leq t \leq N$, N is the total number of samples, can be defined as follows [104]:

$$x(t) = \sum_{o=1}^{r} \beta^{(o)} \begin{pmatrix} x_1(t-o) \\ \vdots \\ x_L(t-o) \end{pmatrix} + \begin{pmatrix} q_1(t) \\ \vdots \\ q_L(t) \end{pmatrix} \tag{2.16}$$

where r is the model order and $\mathbf{q} = [q_1, \ldots, q_L]^T$ is a zero-mean white noise vector with normally distributed real-values. The auto-regression coefficient matrices $\beta^{(o)}$ are given by:

$$\beta^{(o)} = \begin{pmatrix} \beta_{1,1}^{(o)} & \cdots & \beta_{1,L}^{(o)} \\ \vdots & \ddots & \vdots \\ \beta_{L,1}^{(o)} & \cdots & \beta_{L,L}^{(o)} \end{pmatrix} \tag{2.17}$$

where $1 \leq o \leq r$. The matrix $\beta^{(o)} \in \mathbb{R}^{L \times L}$ reveals the linear interactions among multiple time-series at the time delay o. The coefficients β^o are usually determined by the recursive entropy-based Levinson-Wiggins-Robinson (LWR) algorithm [105] that is computationally more robust [106] than classical moment-based method (i.e. Yule-Walker algorithm) [107]. The autocovariance matrix can then be elicited from AR coefficients. For a reliable estimation using MVAR modelling, the total number of available data points (i.e. LN) must be significantly higher than the total number of estimated parameters (i.e. $L^2 r$) [104].

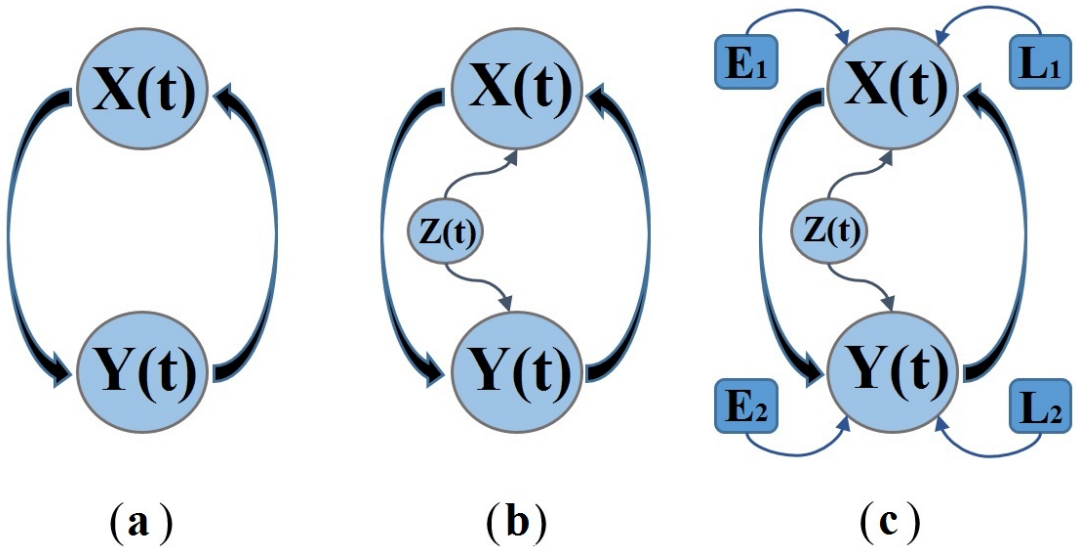

Figure 2.6: Schematic representation of the time-domain GCM approaches. (A) bivariate-GC (BGC), (B) conditional-GC (CGC), and (C) partial-GC (PGC)

The z-domain transformation of the model can be obtained as follows:

$$q(z) = \left(1 - \sum_{o=1}^{r} \beta^{(o)} z^{-o}\right) x(z); z = e^{-i2\pi f \delta t} \tag{2.18}$$

$$A(z) = 1 - \sum_{o=1}^{r} \beta^{(o)} z^{-o} \tag{2.19}$$

$$x(z) = A(z)^{-1} q(z) = H(z) q(z) \tag{2.20}$$

where $H(z)$ and $A(z)$ are the transfer function matrix and its inverse matrix, respectively.

2.5.2.2 Linear time-domain Granger causality

Time-domain GC has been developed under three main frameworks, bivariate -, conditional - and partial - GC, in order to describe the interactions among various data sources [101]. Fig. 2.6 shows the strategies of three GC approaches for dealing with two typical coupled sources $X(t)$ and $Y(t)$ that are mediated by

another source $Z(t)$ and confounded by unknown sources i.e. exogenous input E and latent variables L. Bivariate-GC (BGC) analysis is a straightforward technique that considers two contemporaneous observations (Fig. 2.6A). However, it may not be able to find the true causal effects when two sources are mediated by a third with different time delays [106]. The extended version, conditional GC (CGC) (Fig. 2.6B), provides an unambiguous dissociation of couplings among sources by taking into account all the measured variables [108]. However, the CGC measure is only able to find the interactions of measurable variables, while in situations that are more realistic there may be unknown effects, e.g. exogenous and endogenous inputs, which can confound accurate causal influences [106, 101]. Partial-GC (PGC) was introduced by controlling the aforementioned confounding influences [84]. It is a modification of the standard GC measure that have added terms based on residual correlations between the predicted and the conditional variables (Fig. 2.6C).

The mathematical formulations of GC measures are provided in the following description. Based on GC rules, if the prediction error of one source activity could be improved by taking the previous knowledge of another time series into account, then the latter is said to have a causal influence (i.e. GC) on former [82]. The mathematical formalism of the three GC types for a two-dimensional stationary joint time series is schematically exhibited in Fig. 2.7.

The BGC is applied in pairwise situations. Fig. 2.7A schematically shows two stationary time series P(t) and Q(t), which are jointly interactive. If the prediction error of P(t+1) using o previous values of P(t) and Q(t) (i.e. complete model, Eq. 2.23) is less than the prediction error using only the series P(t) (i.e. reduced model, Eq. 2.21), then Q(t) is said to have a causal influence (Granger-cause) on P(t) ($\zeta^1_{Q\to P}$, Eq. 2.25). Similarly, if the prediction error of Q(t) in the complete model is less than that in the reduced, then P(t) is said to Granger-cause Q(t) ($\zeta^1_{P\to Q}$) [100].

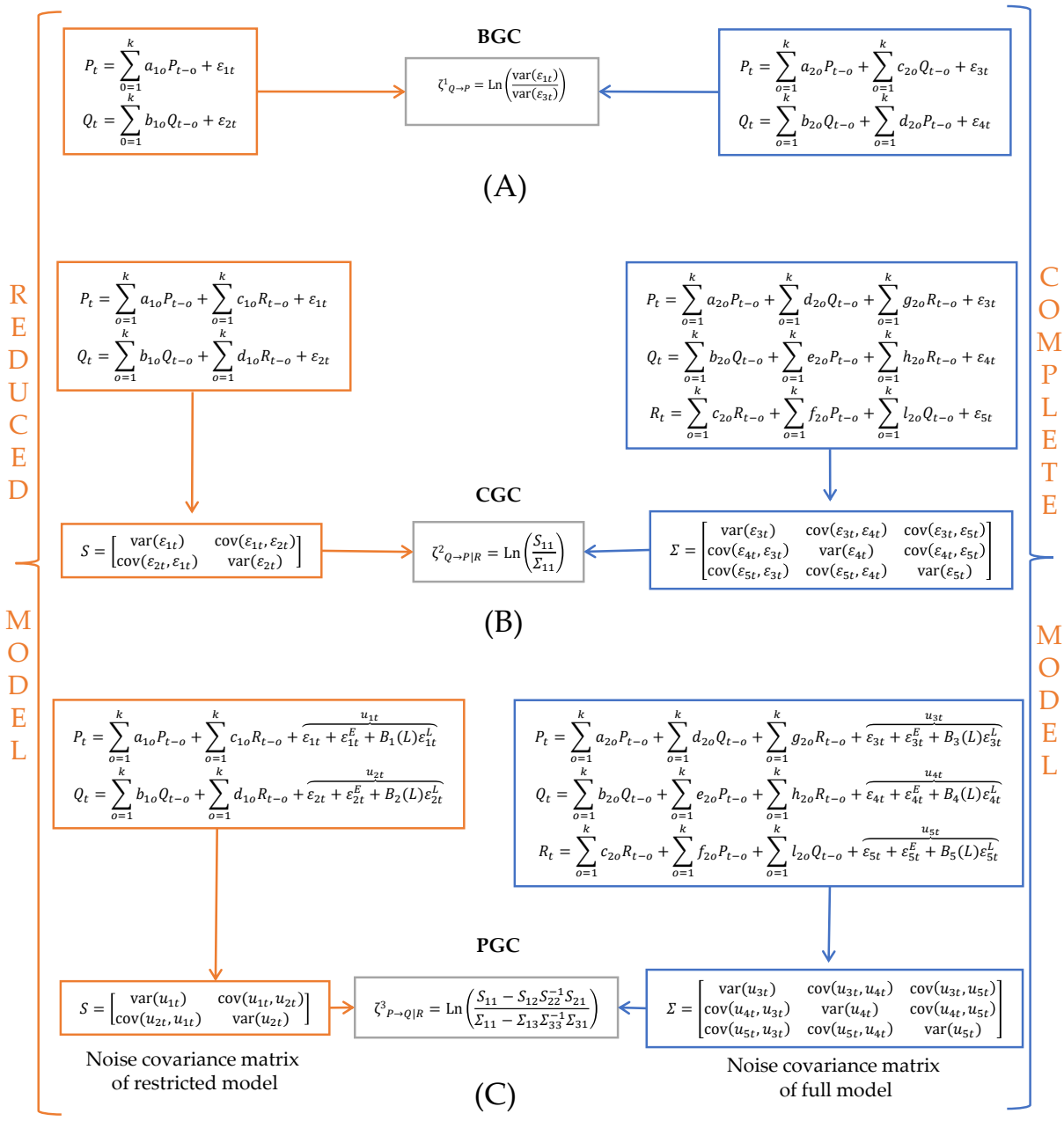

Figure 2.7: Mathematical representation of the time-domain GCM approaches. (A) bivariate-GC (BGC), (B) conditional-GC (CGC), and (C) partial-GC (PGC)

$$P(t) = \sum_{o=1}^{k}(a_{(1,o)}P(t-o)) + \epsilon_1(t) \quad (2.21)$$

$$Q(t) = \sum_{o=1}^{k}(b_{(1,o)}Q(t-o)) + \epsilon_2(t) \quad (2.22)$$

$$P(t) = \sum_{o=1}^{k}(a_{(2,o)}P(t-o)) + \sum_{o=1}^{k}(c_{(2,o)}Q(t-o)) + \epsilon_3(t) \quad (2.23)$$

$$Q(t) = \sum_{o=1}^{k}(b_{(2,o)}Q(t-o)) + \sum_{o=1}^{k}(d_{(2,o)}P(t-o))\epsilon_4(t) \quad (2.24)$$

$$\zeta^1_{Q\to P} = ln\left(\frac{var(\epsilon_1(t))}{var(\epsilon_3(t))}\right) \quad (2.25)$$

$$\zeta^1_{P\to Q} = ln\left(\frac{var(\epsilon_2(t))}{var(\epsilon_4(t))}\right) \quad (2.26)$$

The CGC, an extension of BGC, can be used for more than two time series, namely, when two time series are mediated by a third source. Thus, in the presence of such intervening influence, CGC compares the prediction error between the reduced model (Eq. 2.27) and complete model (Eq. 2.29) when it is conditioned by a third, measurable series R(t). As shown in Fig. 2.7B, the causal influence of Q(t) on P(t) given R(t) ($\zeta^2_{Q\to P|R}$) is defined by the log-ratio of residual variance matrices of the reduced and complete model ($ln\left(\frac{X_{1,1}}{Y_{1,1}}\right)$ in Eq. 2.34). Thus, one variable causally influences a second variable if the prediction error variance of the first is reduced after including the second variable in the model, with all other variables included in both cases.

$$P(t) = \sum_{o=1}^{k}(a_{(1,o)}P(t-o)) + \sum_{o=1}^{k}(c_{(1,o)}Q(t-o)) + \epsilon_1(t) \quad (2.27)$$

$$R(t) = \sum_{o=1}^{k}(b_{(1,o)}R(t-o)) + \sum_{o=1}^{k}(d_{(1,o)}Q(t-o)) + \epsilon_2(t) \quad (2.28)$$

$$P(t) = \sum_{o=1}^{k}(a_{(2,o)}P(t-o)) + \sum_{o=1}^{k}(d_{(2,o)}Q(t-o)) + \sum_{o=1}^{k}(g_{(2,o)}R(t-o)) + \epsilon_3(t) \quad (2.29)$$

$$Q(t) = \sum_{o=1}^{k}(b_{(2,o)}Q(t-o)) + \sum_{o=1}^{k}(e_{(2,o)}P(t-o)) + \sum_{o=1}^{k}(h_{(2,o)}R(t-o)) + \epsilon_4(t) \quad (2.30)$$

$$R(t) = \sum_{o=1}^{k}(c_{(2,o)}R(t-o)) + \sum_{o=1}^{k}(f_{(2,o)}P(t-o)) + \sum_{o=1}^{k}(l_{(2,o)}Q(t-o)) + \epsilon_5(t) \quad (2.31)$$

Thus, the noise covariance matrices for the reduced and complete model can be obtained as:

$$X = \begin{bmatrix} \text{var}(\epsilon_1(t)) & \text{cov}(\epsilon_1(t), \epsilon_2(t)) \\ \text{cov}(\epsilon_2(t), \epsilon_1(t)) & \text{var}(\epsilon_2(t)) \end{bmatrix} \quad (2.32)$$

$$Y = \begin{bmatrix} \text{var}(\epsilon_3(t)) & \text{cov}(\epsilon_3(t), \epsilon_4(t)) & \text{cov}(\epsilon_3(t), \epsilon_5(t)) \\ \text{cov}(\epsilon_4(t), \epsilon_3(t)) & \text{var}(\epsilon_4(t)) & \text{cov}(\epsilon_4(t), \epsilon_5(t)) \\ \text{cov}(\epsilon_5(t), \epsilon_3(t)) & \text{cov}(\epsilon_5(t), \epsilon_4(t)) & \text{var}(\epsilon_5(t)) \end{bmatrix} \quad (2.33)$$

Finally, the directional connectivity measure from $Q(t)$ to $P(t)$ conditioned over $R(t)$ can be estimated as :

$$\zeta^2_{Q\to P|R} = ln\left(\frac{X_{1,1}}{Y_{1,1}}\right) \quad (2.34)$$

$$\zeta^2_{P\to Q|R} = ln\left(\frac{X_{2,2}}{Y_{2,2}}\right) \quad (2.35)$$

The concept of PGC, provided by Guo et al. [84], is based on eliminating the effects of exogenous (environmental) input and latent variables during the estimation of conditional GC. Initially, the representations of exogenous

(environmental) input and latent variables are considered during the MVAR modelling of the data. Later, their effect is mitigated by partitioning the noise covariance matrices generated from the model. For generating a mathematical expression for PGC, similar to case of BGC and CGC, let's consider two time-series as $P(t)$ and $Q(t)$ representing M/EEG data from two electrodes for which causality analysis must be performed (see Fig. 2.7C). Also, consider another time series representing the data from a third electrode (i.e. a common input) as $R(t)$. Further, two separate MVAR models are considered, firstly for predicting the values of $P(t)$ from its previous values and the common input (i.e. reduced model, Eq. 2.36) and secondly for predicting the values of $P(t)$ from the previous values of itself, $Q(t)$ and the common input (i.e. complete model, Eq. 2.38). The reduced model can be presented as:

$$P(t) = \sum_{o=1}^{k}(a_{(1,o)}P(t-o)) + \sum_{o=1}^{k}(c_{(1,o)}R(t-o)) + \epsilon_1(t) + \epsilon_1^E(t) + \beta_1(L)\epsilon_1^L(t) \tag{2.36}$$

$$R(t) = \sum_{o=1}^{k}(b_{(1,o)}R(t-o)) + \sum_{o=1}^{k}(d_{(1,o)}P(t-o)) + \epsilon_2(t) + \epsilon_2^E(t) + \beta_2(L)\epsilon_2^L(t) \tag{2.37}$$

where o is the model order, $\epsilon_i(t)$, $\epsilon_i^E(t)$, and $\beta(L)\epsilon_i^L(t)$ are the prediction errors related to the model, exogenous inputs (E) and latent variables (L), respectively. Likewise, the complete model can be represented as:

$$P(t) = \sum_{o=1}^{k}(a_{(2,o)}P(t-o)) + \sum_{o=1}^{k}(b_{(2,o)}Q(t-o)) + \sum_{o=1}^{k}(c_{(2,o)}R(t-o)) + \epsilon_3(t) + \epsilon_3^E(t) + \beta_3(L)\epsilon_3^L(t) \tag{2.38}$$

$$Q(t) = \sum_{o=1}^{k}(d_{(2,o)}P(t-o)) + \sum_{o=1}^{k}(e_{(2,o)}Q(t-o)) + \sum_{o=1}^{k}(f_{(2,o)}R(t-o)) + \epsilon_4(t) + \epsilon_4^E(t) + \beta_4(L)\epsilon_4^L(t) \tag{2.39}$$

$$R(t) = \sum_{o=1}^{k}(g_{(2,o)}P(t-o)) + \sum_{o=1}^{k}(h_{(2,o)}Q(t-o)) + \sum_{o=1}^{k}(i_{(2,o)}R(t-o)) + \epsilon_5(t) + \epsilon_5^E(t) + \beta_5(L)\epsilon_5^L(t) \tag{2.40}$$

For ease of notation, let's define the collective prediction error as:

$$\mu_i(t) \quad = \quad \epsilon_j(t) + \epsilon_j^E(t) + \beta_j(L)\epsilon_j^L(t) \tag{2.41}$$

with $1 \leq j \leq 5$.

Thus, the noise covariance matrices for the reduced and complete model can be obtained as:

$$X \quad = \quad \begin{bmatrix} \text{var}(\mu_1(t)) & \text{cov}(\mu_1(t), \mu_2(t)) \\ \text{cov}(\mu_2(t), \mu_1(t)) & \text{var}(\mu_2(t)) \end{bmatrix} \tag{2.42}$$

$$Y \quad = \quad \begin{bmatrix} \text{var}(\mu_3(t)) & \text{cov}(\mu_3(t), \mu_4(t)) & \text{cov}(\mu_3(t), \mu_5(t)) \\ \text{cov}(\mu_4(t), \mu_3(t)) & \text{var}(\mu_4(t)) & \text{cov}(\mu_4(t), \mu_5(t)) \\ \text{cov}(\mu_5(t), \mu_3(t)) & \text{cov}(\mu_5(t), \mu_4(t)) & \text{var}(\mu_5(t)) \end{bmatrix} \tag{2.43}$$

Finally, the directional connectivity measure from $Q(t)$ to $P(t)$ conditioned over $R(t)$ can be estimated as:

$$\zeta^3_{Q \to P|R} \quad = \quad ln \left(\frac{X_{1,1} - X_{1,2} X_{2,2}^{-1} X_{2,1}}{Y_{1,1} - Y_{1,3} Y_{3,3}^{-1} Y_{3,1}} \right) \tag{2.44}$$

$$\zeta^3_{P \to Q|R} \quad = \quad ln \left(\frac{X_{2,2} - X_{2,1} X_{1,1}^{-1} X_{1,2}}{Y_{2,2} - Y_{2,3} Y_{3,3}^{-1} Y_{3,2}} \right) \tag{2.45}$$

2.5.2.3 Linear spectral-domain Granger causality

Spectral (frequency-domain) GC is generally measured using elements of transfer matrix $H(z)$ of MVAR, where H is derived by applying z-transform to the causal effects of time-domain GC [109]. The main advantage of spectral GC is the robustness against different levels of noise. Indeed, the Fourier transform equally rescales the residuals of the reduced and complete model, therefore, leaving them GC invariant [90]. Considering Eq. 2.19 and 2.20, the (auto/cross) spectra matrix can be estimated as:

$$S(z) = \quad H(z) \sum H^*(z) \tag{2.46}$$

where $H(z)$ is the transfer function, z denotes z-transform, $\sum$ is covariance of the residuals, and * is complex conjugation and matrix transposition. According to [109, 108], the pairwise (unconditional) spectral GC for two sample P(t) and Q(t) time series can be defined as,

$$\zeta_{Q \to P|R}(z) \quad = \quad ln \left(\frac{|S_{11}(z)|}{|S_{11}(z) - H_{12}(z) \sum_{22|1} H_{12}^*(z)|} \right) \tag{2.47}$$

where $\sum_{ij|o} = \sum_{ij} - \sum_{io} \sum_{oo}^{-1} \sum_{oj}$ denotes a partial covariance matrix and $S_{11}(z)$ is the auto-spectrum of $P(t)$-series. Theoretically, the time-domain causality can be decomposed by frequency components hence the average of spectral causality over all frequencies should give rise to causality in time-domain [106].

Furthermore, there are two other popular spectral connectivity estimators based on MVAR modelling, i.e. partial directed coherence (PDC) [110, 111] and directed transfer function (DTF) [112]. Their estimations can be obtained according to the following equations:

$$\textbf{PDC}_{j \to i}(z) = \frac{|A_{ij}(z)|}{\sqrt{A_{:j}^T(z) A_{:j}(z)}} \tag{2.48}$$

$$\textbf{DTF}_{j \to i}(z) = \frac{|H_{ij}(z)|}{\sqrt{H_{i:}(z) H_{i:}^T(z)}} \tag{2.49}$$

2.6 Applications of neuronal activation pattern detection using M/EEG in the fields of communication, control and stroke rehabilitation

M/EEG have been extensively used for various applications such as clinical decision making, rehabilitative and restorative interventions, communication and control, and cognitive training. This section discusses the scope of these applications and related previous research work.

2.6.1 Communication and control

The ability to communicate - whether by speech, email, text message, or even a simple head nod or smile - is central to human interaction. For people who have severe communication disabilities despite intact cognition, M/EEG-based BCI technology is poised to have a profound impact. One clinical condition, locked-in syndrome (LIS), is commonly identified as the most immediate target for neuroimaging-based BCI researchers. LIS can result from a variety of clinical etiologies, including: acute events such as ischemic or hemorrhagic infarction of the brainstem or motor neuron disease, most notably amyotrophic lateral sclerosis (ALS) [113, 114].

For people with incomplete LIS, early EEG-based BCI systems using evoked potentials to choose among items in a matrix or to provide unidimensional or multidimensional cursor control have already been shown to enable selection of letters or words on a screen [115, 9]. BCIs of this kind are currently in use by a small number of people with advanced ALS [116].

For people with total LIS (e.g. some people with advanced ALS and on chronic mechanical ventilation), there has not yet been a successful demonstration of BCI use. Although it is possible that this reflects the limitations of BCI systems attempted thus far and/or the dearth of sufficiently meticulous studies. It has also

been suggested that the complete LIS state, as defined above, exists only transiently, since the state of complete de-efferentation might quickly lead to diminished goal directed behavior [117]. Nevertheless, with extensive training, completely locked-in patients are able to modulate their SCPs which can be sufficient to generate control signals for moving a cursor on a computer screen [118]. On similar lines, Birbaumer et al. developed a communication application involving selection of virtual keyboard letters using EEG-driven cursor movement [64]. The study involved validation of the proposed system with two patients at advanced stages of ALS wherein a mean typing rate of 2 characters per minute was achieved during a message typing task.

EEG-based virtual keyboard applications also utilised other types of control signals, such as classification of three cognitive tasks [119] and detection of eye blinks [120] to select the commands or characters. A letter speller was also designed using a standard Graz-BCI systems [121]. Apart from these features, P300 event-related brain potentials are also very popular in BCI-based speller applications. P300-based BCI systems have been sufficiently suitable for ALS patients, in particular those are in the early and middle stages of the disease [122]. P300-based systems have advantage over others as the brain responses occur spontaneously and consequently do not require substantial training. Moreover, recent advancement with P300-based spellers have resulted in the development of commercial applications available to the general public [123].

Movement restoration, such as grasping, is feasible in physically-disabled patients through functional electrical stimulation (FES)-guided neuroprostheses. FES is capable of eliciting artificial muscle contractions which can be implemented for voluntary actions (see [124] for a review). A tetraplegic patient was able to control paralyzed hands to grasp a cylinder wherein the FES was guided by the beta bursts generated through foot movement imagery [125]. A combined FES-robot based training system using user's residual EMG signals was developed for facilitating an effective wrist control of a stroke patient [126].

Although FES has been proven to be an effective way to restore movement, it requires the use of residual movements, which are not possible in severely impaired patients. For this reason, some groups have started to explore other approaches to control the neuroprostheses such as using the control signals generated directly from the features of M/EEG activations such as MI-related features and ERPs. MI-related features (i.e. ERD/ERS) were exploited effectively to control a hand orthosis by tetraplegic patients, whose residual upper-limb muscle activity was restricted to the left biceps, due to an upper spinal cord injury [127, 128].

Multi-class MI (i.e. left-right hands MI, foot movement, and idle state) has been explored for wheelchair control applications using both synchronous and asynchronous BCI systems in virtual as well as real-world environments [129, 130, 131]. Moreover, an EEG-based human-robot interface has been explored with autonomous navigation system wherein steady-state visually evoked potential (SSVEP) brain responses were utilised to design a smart wheelchair system for disabled people, who have impairments in their arms and legs [132, 133]. A brain signal controlled neuroprosthetic device was developed using four-class SSVEPs for the reestablishment of the grasp motor function for people with spinal cord injuries [134]. This system enabled operation of four different movements corresponding to the four different frequencies of LEDs flickering. In similar lines, MEG-based evoked potentials were utilised to trigger rehabilitative devices such as upper limb exoskeletons and digit fingers in order to restore the grasping motor tasks in paralysed patients [29, 135].

2.6.2 Stroke rehabilitation

Extensive brain plasticity can occur during spontaneous recovery after stroke. Human studies have provided evidence of brain changes during natural recovery of motor function after stroke [136, 137, 138, 139]. Even in regions distant from the infarction, Graziadio et al. (2012) reported positive correlation between the recovery index and degree of symmetry within both lesioned and nonlesioned

corticospinal systems [140]. There is also evidence for other kinds of changes during natural recovery, including reorganization of cortical excitability and motor maps [141, 142, 143, 144], changes in the functional and effective brain connectivity [145, 146], and rerouting of ipsilesinal and contralesional hemispheric connections [147, 148].

In addition to the plastic changes occurring during spontaneous motor recovery, several studies have demonstrated restorative intervention-dependent brain plasticity resulting from specific training after neural injury. These restorative interventions may involve physical activity (e.g. physical therapy, constraint-induced movement therapy, gait therapy) [149, 150], cognition tasks (e.g. motor imagery (MI), mirror therapy, virtual and augmented reality) [151, 152, 153, 154, 155], device-driven (e.g. robotics, BCI) [156, 157, 158, 159], sensory stimulation (e.g. vagal nerve stimulation, passive limb movement, and electrical stimulation) [160, 161], brain stimulation (e.g. repetitive transcranial magnetic stimulation, transcranial direct current stimulation, and epidural cortical stimulation) [162, 163, 164], and pharmacological interventions [165].

BCI systems involving M/EEG-based BAPD can also be useful in supplementing standard neurorehabilitation therapies so as to improve the functional outcomes of the target population. Physical, occupational, and/or speech and language therapy are commonly used in stroke rehabilitation. Recognizing the brain's capacity for activity-dependent plasticity, newer rehabilitative therapies seek to modify injured brain areas or to encourage non-injured brain areas to assume the functions of injured areas [138, 166, 167]. BCIs might contribute to these goals by encouraging the return of brain activity that can enable voluntary control of the limbs, and/or by strengthening existing functional neural pathways by pairing movement intentions with actual movements (e.g. assisted therapeutic exercise) [168].

M/EEG-based BCI training can also be applied to the problem of motor recovery after neural injury. While conventional therapies for treating motor

impairments after stroke, other CNS trauma, or disease rely on exercise of the limbs, M/EEG-based training offers a different approach to motor-recovery therapy. Broetz et al. [169] proposed a combination of MEG and EEG-based BCIs. Initially, the MEG-based BCI was used to boost rehabilitation training success. Later, the user continued rehabilitation training with an EEG-based BCI; a more affordable technology than MEG. The results of this study suggest that the combination of BCI training with goal-directed active physical therapy improves the motor abilities of chronic stroke patients. In similar studies, the effectiveness of a combination of BCI training and physiotherapy for stroke rehabilitation was confirmed [170, 8]. These studies encourage further research on the role of BCIs in brain plasticity and post-stroke recovery. Taken as a whole, these studies provide abundant evidence of the extent and complexity of plasticity associated with recovery after injury. It is thus intriguing to consider that, by focusing training directly on brain activity, M/EEG-based BCI systems might induce or guide plasticity that results in the recovery of motor control.

Frequently repeated, skilled motor actions, particularly those employing precise temporal coordination of multiple muscle activations and joint movements, can induce changes in sensorimotor areas of the brain. Current therapeutic methods based on such repetition focus on improving limb movements, and any associated induced brain plasticity occurs ostensibly in response to the limb motor practice and the sensory afferent input it induces. Thus, BCIs, which can focus on changing brain activity itself, may offer a more direct and effective avenue for inducing brain plasticity that improves motor function. BCIs might provide a powerful new approach to improving motor function after CNS trauma or in disease.

2.7 Open challenges in the research field of M/EEG analysis

2.7.1 EEG data pre-processing

The overall performance of EEG-based BCI system depends on various factors, e.g. pre-processing of the raw brain signals, extraction of information (features) related to the mental task, translation of the features into control commands, and finally the application of the control commands to the output device (i.e. controlling a process). Most of the previous research studies focused on feature extraction algorithms and their optimisation for the overall performance improvement although pre-processing operations can affect the performance of the system significantly [171, 172, 173]. The complex multi-dimensional EEG data recorded at scalp level provide a direct inference of the electrical activity associated with a sizable neuronal population of the brain cortex. Volume conduction (VC) results from mixing of the spatio-temporal information generated at the cortical sources of the brain as the tissues and bone structure between the human cortex and the scalp induce superimposition of electrophysiological dynamics of the EEG signal [11, 12].

Several measures can be applied for minimising the effect of VC at the scalp level EEG recordings. Different referencing schemes (e.g. CR, bipolar, CAR) and Laplacian filtering methods (e.g. Hjorth, SSL methods) have been implemented earlier for this purpose [13, 14, 15, 16, 17] (for further details refer to [18]). Apart from these, ICA [174], PCA [175], and advanced source localisation techniques (i.e. beamforming, sLORETA) [176, 177] have been utilised for enhancement of the BCI performance. Additionally, recent studies using source localisation techniques have shown that the linear inverse transforms can be applied in real time and have shown significant improvement in the MI task classification performance of M/EEG-based BAPD systems [178, 179, 180].

Prior research studies that involve qualitative comparison of different spatial transformation methods often restrict their analysis to different algorithms or

different parameters for the same algorithm (e.g. different parameters of current source density (CSD) estimation, source imaging techniques, or different ICA algorithms) [19, 20, 21]. Other published works emphasise the theoretical perspectives while comparing different referencing schemes or Laplacian filtering methods, with little or no consideration of their impact on the performance of M/EEG-based BAPD systems (e.g. BCIs) [181, 182]. Although the findings of these studies may contribute significantly to the optimisation of the algorithms, limited information has been provided for the BCI researchers regarding the achievable improvement in the classification accuracies using these methods. A recent study showed enhancement of binary classification accuracies during MI task with CAR implementation as compared to CR [183]. However, the study involved preliminary analysis (only five subjects and two classes) and did not include spline based Laplacian methods, which recently attracted a lot of EEG-based studies [19, 20, 15, 59]. Thus, there is an urgent need for an empirical evaluation of the effect of the currently available referencing schemes and SL methods on single-trial classification of EEG signals.

2.7.2 Low performance with connectivity-based features for M/EEG-based single-trial detection

Most of the current M/EEG-based BCI systems involving MI detection rely on task-specific changes in the sensorimotor EEG rhythms (ERD and ERS), which involve kinaesthetic imagination of a particular motor action without its actual execution [184, 185, 186]. Although promising results and achievements have been reported in the literature [187], there remain many challenges and barriers to the use of this technology reliably and efficiently for the intended beneficiaries [22]. One of the probable reasons for the lower accuracies of MI-based BCI systems is the use of static channel derived features (e.g. band-power (BP), autoregressive (AR), CSP, and wavelets), which may not contain information about interactions among different brain regions, while it is well known that multiple brain regions dynamically interact in accomplishing a mental

task. Thus, it is reasonable to assume that the connectivity of spatially distributed regions could provide additional useful discriminant features for the classification of brain responses evoked during imagery tasks.

Over the last few years, several research groups attempted to implement connectivity-based BCI systems [22, 23, 24, 25, 26] using different measures to map the interactions between distinct brain regions (e.g. transfer entropy [188], coherence, directed transfer function (DTF) [112], and partial directed coherence (PDC) [110]). A recent study implemented several vector autoregressive (VAR) model-based methods for the realisation of MI-based BCI system [25]. The empirical findings provided low classification accuracies for most of the methods when compared to BP features. In this case, the connectivity between scalp electrodes failed to provide robust distinction among various MI tasks.

Investigations of the connectome associated with imagination (i.e. MI) as well as the execution of motor tasks revealed the manifestation of induced activations and information flows at various cerebral structures, including, the primary motor areas (M1), the premotor cortex (PMC), and the supplementary motor areas (SMA) [189]. These cortical areas are located in close vicinity to each other making estimation of the MI task specific causal interactions a challenging task, in particular at scalp level analyses, due to the VC effect. Furthermore, single-trial connectivity estimations become inherently more difficult due to a lack of sufficient EEG data for this type of analysis. These confounding factors lead to the low performance of connectivity-based MI-BCI systems. Thus, the current literature showed a major research challenge in terms of finding a novel approach to improve the performance of single-trial functional connectivity-based BCI systems.

2.7.3 Neurophysiological validation of BCI based upper-limb neuro-rehabilitation for stroke patients

Recovery of movement related functions after stroke and its assessment are highly crucial for restoring activities of daily living of the patients. Majority of the

stroke survivors have upper limb (UL) associated impairment symptoms in chronic stage [190]. Many patients show some degree of spontaneous (autonomous) UL motor recovery during initial months following a stroke, however, in general, this is inadequate recovery in terms of physical outcomes [191, 192]. Therapeutic interventions of stroke survivors using M/EEG-based BCI system, in particular with MI-based paradigms have been effectively implemented previously [8, 193, 194, 28, 195, 196, 197, 29, 27] (see a recent review [198]).

The rationale behind using the MI-related M/EEG-BCI systems for stroke rehabilitation is that the mental workload associated with MI involves the brain areas that govern UL movement execution [199, 65]. Moreover, recent advancements in the M/EEG-driven stroke rehabilitation showed the significant efficacy of visual and proprioceptive feedback and robotic UL exoskeletons along with MI [200, 27, 195]. Furthermore, several other studies reported successful implementation of BCI-driven exoskeletons for attaining functional recovery in patients with post-stroke hand paresis [196, 201, 202]. These studies involved various types of end-effector based haptic and kinesthetic feedback systems to improve the clinical parameters of post-stroke motor recovery e.g. a haptic knob [195], MIT Manus [28], and a custom-made orthotic device [203, 204, 205]. While an increasing number of studies have shown significant alterations in neural activations and functional connectivity networks related to the mental imaginary tasks and/or attempted movements of an impaired upper extremity with the use of neural signal driven-robotic devices [203, 206, 200, 207], it still remains unclear whether and to what extent the underlying neurophysiological mechanisms are affected during a UL stroke rehabilitative intervention using an MI-related EEG-driven hand-exoskeleton.

There are three major constraints of the currently available functional connectivity-based studies implemented for validation of the clinical efficacy of M/EEG-based rehabilitative interventions. Firstly, the majority of them are focused on the reorganisation of brain networks during the MI task, and thus,

include the issue of controlling for effort and performance when stroke patients with varying motor deficits are under consideration [168, 208, 209]. Secondly, the comparisons are drawn on the difference between the functional brain networks obtained at the pre- and post-intervention states, and thus, failed to observe the continuously changing patterns in the brain networks during the course of the rehabilitative intervention [200, 210]. Lastly, no previous study attempted to examine brain network-based neurophysiological changes for a multi-modal UL rehabilitation intervention involving the simultaneous implementation of MI, BCI, visual and proprioceptive feedbacks, and robotic hand-exoskeleton. Thus, there is a pressing need to examine the brain functional networks that are correlated with the motor recovery during a longitudinal multi-modal UL stroke rehabilitative intervention.

2.8 Summary

This chapter has provided a review of two often used neuroimaging techniques i.e. EEG and MEG along with the currently available computational algorithms that are implemented for analysis and modelling of the M/EEG data. In particular, special emphasis is given to various pre-processing methods (i.e. EEG referencing schemes and SL methods), feature extraction methods (i.e. CSP and Granger causality based connectivity features), and application of single-trial BAPD with M/EEG signals. Furthermore, based on this literature review, three open research challenges have been identified to further improve the computational analysis of M/EEG signals in pursuit of performance enhancement of M/EEG-based BAPD systems. Firstly, despite the availability of various referencing schemes and SL methods for EEG, there is no empirical evaluation of their impact on the performance of single-trial EEG-based BAPD systems. Secondly, over the last few years, several studies showed the potential of functional connectivity features to be useful for single-trial BCI systems, however, the performance of these systems are still not sufficient to be used for practical application. Moreover, the majority of these studies showed significantly poor classification accuracies of FC features

as compared to the features derived from intra-channel signals. Lastly, there is a compelling need to study the patterns of functional brain networks associated with the motor recovery during a longitudinal brain-machine interface-driven UL stroke rehabilitative intervention. These challenges motivate to research towards handling these issues associated with current M/EEG-based BAPD systems that opens a prospect of novel contributions towards advancing the computational analysis and modelling of M/EEG data. Furthermore, Chapter 3, 4, and 5 of this thesis aim to address these open challenges by considering each of them separately.

Chapter 3

Current source density estimation enhances the discriminability of motor-imagery related brain responses

3.1 Introduction

Electroencephalographic oscillations, recorded over the scalp, can be the basis of alternative modes of communication and control, in particular as brain activation pattern detection (BAPD) systems (e.g. brain-computer interfaces (BCIs)) [64, 211, 212]. Non-invasive electroencephalography (EEG)-based BCI systems acquire neural signals at scalp level, analyse them to extract specific features (patterns) of brain activity that are related to the voluntary imagery/execution mental tasks, detect the related tasks from the extracted features, and finally utilise the detection outcomes as control signals that are further relayed to efferent devices. During the past few decades, EEG-based BAPD systems attracted significant research interests due to the relative ease of conducting experiments, inexpensiveness, and minimal risk to the participants. In general, there are two ways to generate the mental task specific features. First, in

the case of active BCI paradigms, features of the spontaneous brain signals generated during the performance of endogenous tasks, for instance, motor-imagery (MI), emotion imagery, and mental arithmetic tasks are considered [213, 214]. Second, in case of reactive BCI paradigms, brain potentials generated in response to the specialised external stimulations (e.g. P300, steady-state evoked potentials, and evoked potentials) are utilised [215, 216]. The former approach of BCI implementation is highly prevalent, in particular, the MI-related BCI systems which is one of the most explored M/EEG-based paradigms [217, 218, 219].

This chapter aims to target the open challenge presented Section 2.7.2 of Chapter 2. In particular, it undertakes an empirical evaluation of the effect of the currently available referencing schemes and surface Laplacian (SL) methods on single-trial classification of EEG signals and includes two different studies. The first study aims to evaluate the impact of two referencing schemes: common reference (CR) (left mastoid) and common average referencing (CAR), and three spherical surface Laplacian (SSL) filtering methods: current source density (CSD) [15, 220], SSL with finite-difference method (SS_F) [59], and SSL using realistic head model (SS_R) [17], on the classification performance of the MI-based BCI systems. The raw EEG signal was pre-processed separately using the above mentioned five methods, and support vector machine (SVM) classifier has been implemented on features generated by the filter-bank common spatial pattern (FBCSP) algorithm. The performance is evaluated for both binary and multi-class classification tasks. Furthermore, the effect of reducing the number of the channels at the pre-processing level and the feature extraction level has also been studied. Based on the results of the first study, the analysis is further extended in the second study. The extended analysis involved estimation of the effect of CSD on the discriminability of single-trial directed functional connectivity features related to the EEG signals during four MI tasks. Both studies involved same EEG dataset. In particular, the classification performance of the time-domain partial Granger causality (PGC) measures with and without performing CSD

pre-processing are compared.

The further sections of the chapter are organised as follows: Section 3.2 provides a detailed description of the EEG dataset and the algorithms implemented in both the studies. Section 3.3 presents data processing and analysis pipeline, and the results of study I. Section 3.4 presents data processing and analysis pipeline, and the results of study II. Section 3.5 provides a detailed review of the outcomes and impact of the studies undertaken in this chapter. Section 3.6 summarizes the findings of this chapter.

3.2 Materials and methods

3.2.1 EEG dataset

The BCI competition-IV [221], dataset 2A is a publically available MI related EEG dataset. The dataset comprised of 4 classes of MI tasks (i.e. left hand movement imagery, right hand movement imagery, both feet movement imagery, and tongue movement imagery) from nine healthy participants, namely [A01-A09]. Two sessions, one for training and one for evaluation, were recorded from each participant. The EEG data were acquired with 22 monopolar EEG channels (with left mastoid as the reference and right mastoid as the ground) and three monopolar electrooculogram (EOG) channels.

3.2.2 Estimation of current source density

Spherical spline interpolation method, presented by Perrin et al. [15, 220], was implemented for the estimation of scalp-level CSD values from the raw EEG data. The following expressions formally define the estimation of CSD:

Let's assume an EEG data with N number of electrodes with v_i be the amplitude estimated for i^{th} electrode. Now, the first step is to calculate the function $g(\cos(L_i, L_j))$, also known as G matrix, using the following mathematical

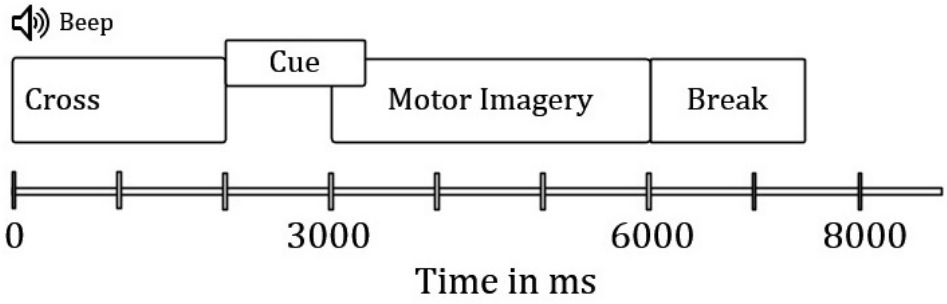

Figure 3.1: The task-timing of the experimental paradigm for dataset-2A. Trial duration is 6 s with a break of 1.5 s between trials. Trial start is indicated with an acoustic beep and appearance of the fixation symbol. After 2 s, participants are cued for the MI task to be performed.

expressions:

$$g(x) = \frac{1}{4\pi}\sum_{p=1}^{\infty}\left(\frac{2p+1}{p^q(p+1)^q}\right)\cdot E_p(x) \tag{3.1}$$

$$\cos(L_i, L_j) = 1 - \frac{(X_{L_i} - X_{L_j})^2 + (Y_{L_i} - Y_{L_j})^2 + (Z_{L_i} - Z_{L_j})^2}{2} \tag{3.2}$$

where, (X, Y, Z) are cartesian coordinates; L_i and L_j are spherical projections of i^{th} and j^{th} electrodes; q is the spline flexibility index and $E_p(x)$ is the Legendre polynomial of degree p. The second step is to estimate the transformation constants $k_i s$ using the solutions of the following equations:

$$\begin{aligned}(G+\lambda)K + Dk_0 &= V \\ D'K &= 0\end{aligned} \tag{3.3}$$

where $D' = [1, 1, \ldots, 1]$, $K' = [k_1, k_2, ..., k_N]$, $V' = [v_1, v_2, ..., v_N]$, $G = g(\cos(L_i, L_j))$, and the value of λ (smoothing constant) is equals to 1.0e - 5. We have selected a default value for λ as the splines performed best at this value

(see [15, 220] for further details). Similar to Eq. 3.1, the function $h(cos(L_i, L_j))$, also known as H matrix, can be estimated using:

$$h(x) = -\frac{1}{4\pi}\sum_{p=1}^{\infty}\left(\frac{(2p+1)^2}{p^q(p+1)^q}\right)\cdot E_p(x) \tag{3.4}$$

where x is $\cos(L_i, L_j)$ and can be generated using Eq. 3.2. Finally, the CSD estimates can be generated using:

$$U(L) = \sum_{i=1}^{N} k_i h(cos(L, L_i)) \tag{3.5}$$

Thus the EEG transformation process using CSD method involves three major steps. The first step is to generate two transformation matrices termed G and H using Eqs. 3.1 and 3.4. These transformation matrices depend only on the number and relative position of surface locations included in the EEG montage (i.e. their cosine distances), which can be estimated using Eq. 3.2. For this reason, these matrices have to be computed only once for any given EEG montage. Therefore, they have no impact on the duration of the calibration process. The second step is to calculate the constant vector (K) using Eq. 3.3. The length of the constant vector is equal to the number of electrodes in the EEG montage. The final step is to compute the CSD values for each EEG channel data using Eq. 3.5.

3.2.3 Finite-difference method on a triangulated $3D$ spherical surface

The SS_F method, presented by Oostendorp et al. [59], provides the approximation of SL operator on a triangulated $3D$ spherical surface (cf. Chapter 2, Section 2.4.4). Thus, an interpolation for scalar functions on a rectangular grid on a planar surface is extended to the interpolation function on a closed three-dimensional triangulated surface. This method is elaborately described in Section 2.4.4 of Chapter 2.

3.2.4 Spline surface Laplacian filtering for realistic head geometry

The SS_R method has the advantage of being readily applicable to the surfaces defined by MRI-based triangular meshes without the help of any intermediate representations, and it does not require any coordinate transformations as well [17]. The complete mathematical expressions and implementation of SS_R is presented in Section 2.4.5 of Chapter 2.

3.2.5 Time-domain partial Granger causality analysis

The concept of PGC, provided by Guo et al. [84], is based on eliminating the effects of exogenous (environmental) input and latent variables during the estimation of conditional GC. The representations of exogenous (environmental) input and latent variables are considered during the multivariate autoregressive (MVAR) modelling of the data. Later, their effect is mitigated by partitioning the noise covariance matrices generated from the model. The method is already described in Section 2.5.2.2 of Chapter 2 along with other variants of time-domain GC.

3.2.6 Filter bank common spatial patterns

The filter bank CSP (FBCSP) is a widely used feature extraction algorithm. FBCSP is an extension of the CSP algorithm, where n different bandpass filters are used at the first stage to decompose the data into multiple frequency bands in the temporal domain [222]. In the subsequent stage, CSP is typically used to create spatial filters for detecting event-related desynchronisation/synchronisation (ERD/ERS) within each frequency band. The mathematical concept behind CSP is described previously in Section 2.5.1 of Chapter 2. A total of 10 bandpass filters in MI-related frequency range are used (i.e. [$8-12$ Hz], [$10-14$ Hz], [$12-16$ Hz],...,[$26-30$ Hz]) for creating the filter bank.

3.3 Study I: Evaluation of the impact of various pre-processing schemes on classification of MI-related tasks

This analysis involves experimental evaluation of the impact of two referencing schemes: CR (left mastoid) and CAR, and three SSL filtering methods: CSD [15, 220], SS_F [59], and SS_R [17], on the MI-based BCI classification performance using a four class dataset.

3.3.1 Signal processing pipeline

According to Fig. 3.2 (b) in the MI related EEG-based BCI, the following steps have been implemented for the BAPD of four MI tasks: raw EEG signal acquisition, pre-processing, feature extraction (i.e. temporal and spatial filtering), and classification. Initially, the raw EEG signals from the complete set of 22 channels have been considered and then pre-processing has been performed to improve the spatial resolution using each of the following methods (see Fig. 3.2 (a)): CR, CAR, CSD, SS_F, and SS_R. For SS_R, the default head MRI model provided with the SSLtool toolbox [17] has been utilised. Further, in the feature extraction stage, a bandpass filter bank has been applied to decompose the EEG signals into different frequency bands (FBs) by employing an 8^{th} order, zero-phase forward and reverse bandpass Butterworth filter. A total of 10 bandpass filters with overlapping bandwidths, including [8−12 Hz], [10−14 Hz], [12−16 Hz], [14−18 Hz], [16−20 Hz], [18−22 Hz], [20−24 Hz], [22−26 Hz], [24−28 Hz], [26−30 Hz], are used to process the data from 10 EEG channels (represented with gray colour in Fig. 3.2 (a)). Later, spatial filtering has been performed on each FB, which helps to maximise the divergence of bandpass filtered signals under one class and minimise the divergence for the other class. In the MI-related BCI systems, both physical and imaginary movements cause growth of bounded neural rhythmic activity known as ERD/ERS.

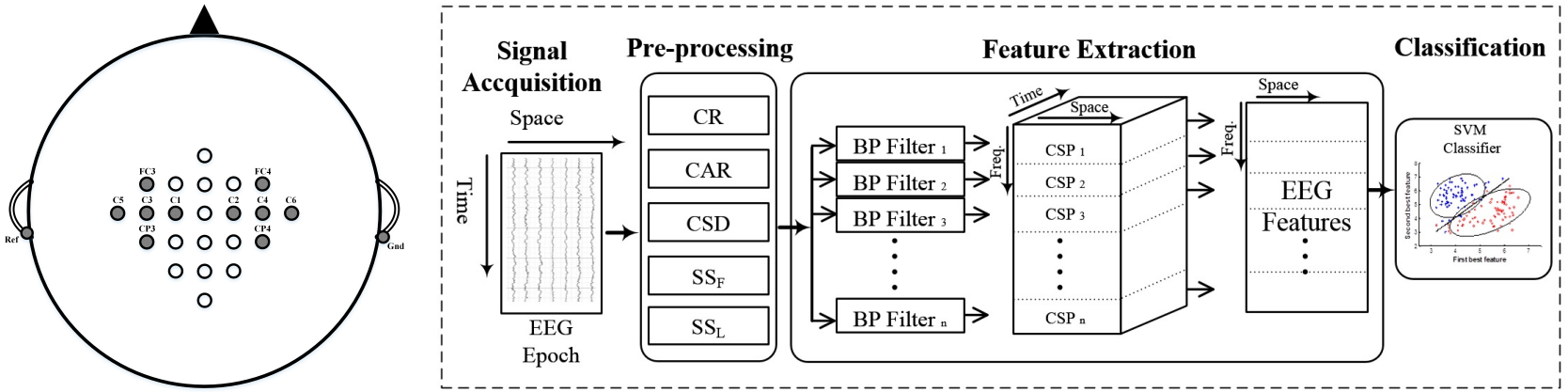

Figure 3.2: (**a**) Montage of the acquired EEG data representing the 22 sensors used for pre-processing, and the 10 sensors (gray in colour) used for feature extraction. (**b**) EEG signal analysis pipeline involved in study I with an overview of the different processing steps.

The CSP algorithm is widely used for calculating the spatial patterns for detecting ERD/ERS [222]. Each combination of the bandpass filter and CSP algorithm calculates the discriminative features that are distinct to the particular frequency range. After doing CSP filtering, the discriminating features have been extracted using a time window of 3 s after the cue onsets. This particular time segment is responsible for capturing the MI related ERD/ERS activities. The features obtained after applying CSP algorithms from all FBs are merged to create the set of input features for training/testing a classifier. Finally, the performance is obtained by measuring the accuracies for both two-class (i.e. the six pairwise binary classification tasks over four MI classes), and four-class BCI approaches using a linear SVM classifier. As the focus here is to evaluate the effect of various pre-processing methods on the performance of a MI-related BCI system, implementation of other classifiers e.g. linear discriminant analysis (LDA) or multiple classifiers is out of scope of the current study. Moreover, to avoid the possible bias caused by complex classifier designs e.g. multi-kernal, non-linear kernal, we have opted for a linear SVM model.

For the four-class approach, features were generated in one-versus-rest condition and four linear SVM classifiers were implemented for estimation of classification accuracies. The classifier was on the features of the first session data and performance was evaluated on the features of second session data. Moreover, the whole process was repeated for three different configurations of channel selection (i.e. 22/22, 22/10, and 10/10). We thus use the couple (N_{s0}/N_{s1}) to denote the number of sensors that are used for pre-processing (N_{s0}) and for feature extraction (N_{s1}).

The computational work has been performed on an Intel Core i7-4790 with 16 GB of memory, using in-house programs written in MATLAB V8.1 (The Mathworks, Natick, MA). The Matlab codes for implementing three SSL methods have been obtained from publicly available toolboxes (CSD toolbox [223], SSLtool [17], and Fieldtrip [224]).

3.3.2 Results

3.3.2.1 Spatial and temporal analysis

To study the topographical responses of the methods, we implemented a similar approach published in a recent study [225]. Bivariate Pearson's correlation coefficients (R) between class target (i.e. a dummy variable, coded -1 and $+1$) and bandpower features in μ (8$-$12 Hz) and β (13$-$30 Hz) frequency bands for each electrode have been generated. These values were estimated for each binary task pair, subject, and session for 3 s of the MI-related period. Further, group averaged R^2 values (across subjects and sessions) were estimated and scalp plotted over the 22 channel EEG montage for all the pairwise binary classification tasks and referencing methods in μ and β frequency bands (see Fig. 3.3). The maplimit for all the topoplots within a pairwise binary task is kept same for making the plots comparable across various referencing methods and frequency bands. Fig. 3.3 depicts higher values of correlation for CAR, CSD, SS_F and SS_R as compared to CR.

Moreover, for most of the pairs of classes, CSD topographic plots showed relatively darker yellow colour spots as compared to other methods. This evidently suggests that CSD provided better spatial localisation and higher values of R^2. Furthermore, time evolution plots of the averaged and normalised envelopes of EEG signals (for μ and β frequency bands) from C3 and C4 EEG channel for the four imagery classes are presented in Fig. 3.4. Here, we included EEG data segment from 0 to 6 s from each trial, including both the rest state (i.e. from 0s to 3s) and MI state (i.e. from 3s to 6s). The envelope of the time series has been obtained using absolute values of Hilbert transformed signals. The envelope plots show better separability between two classes for the three Laplacian methods (i.e. CSD, SS_F, SS_R) and CAR methods as compared to CR. It is worth noting that the common-reference data appears to show an artefact at the beginning of the trial (see the left-most column of Fig. 3.4).

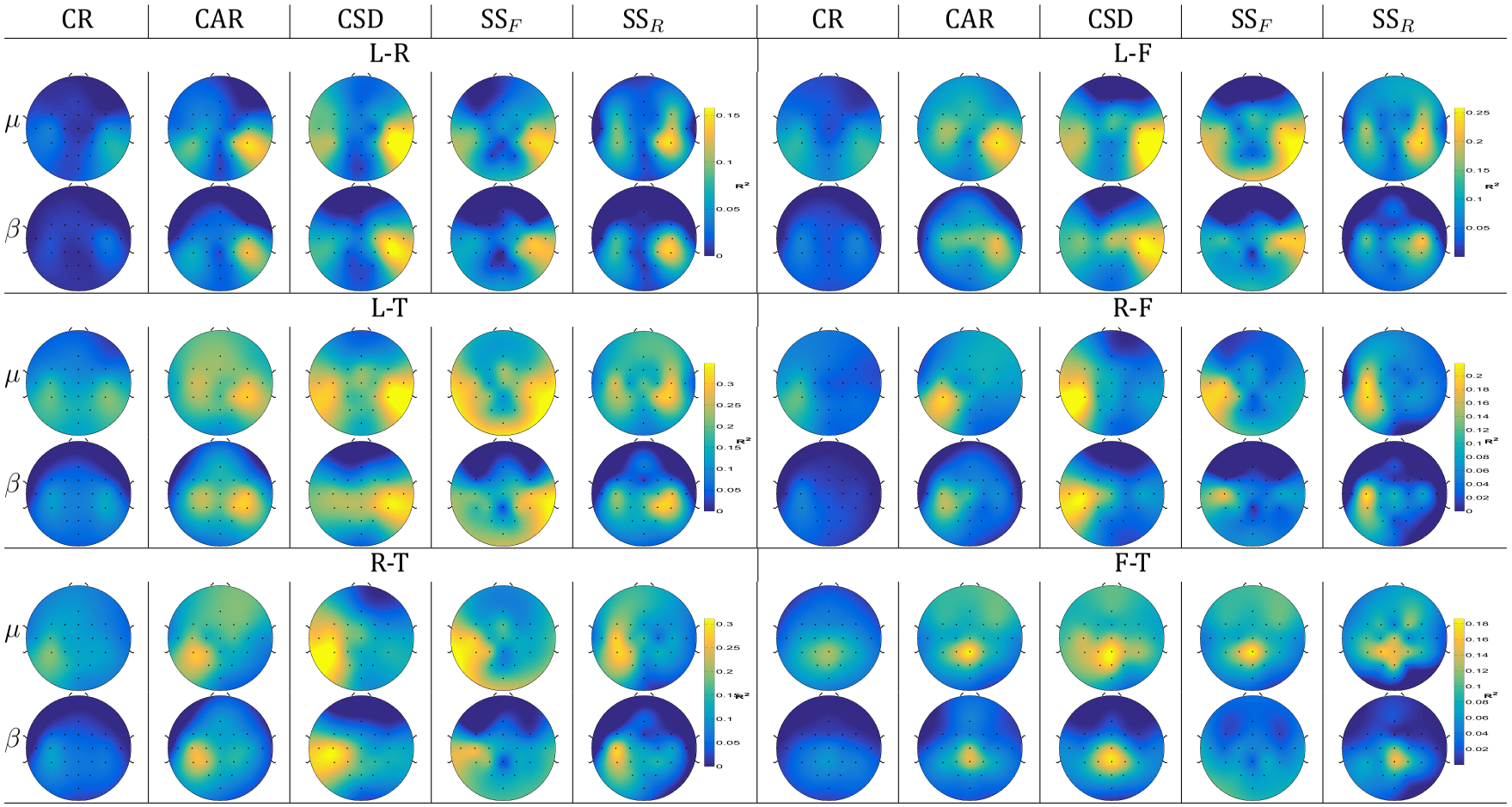

Figure 3.3: Topographical plots representing the grand average correlation values (R^2) between average bandpower values (within μ-band (8-12Hz) and β-band (13-30Hz)) for six binary classification tasks and five referencing methods. R^2 values were averaged over subjects and sessions and scalp plotted for all 22 electrodes.

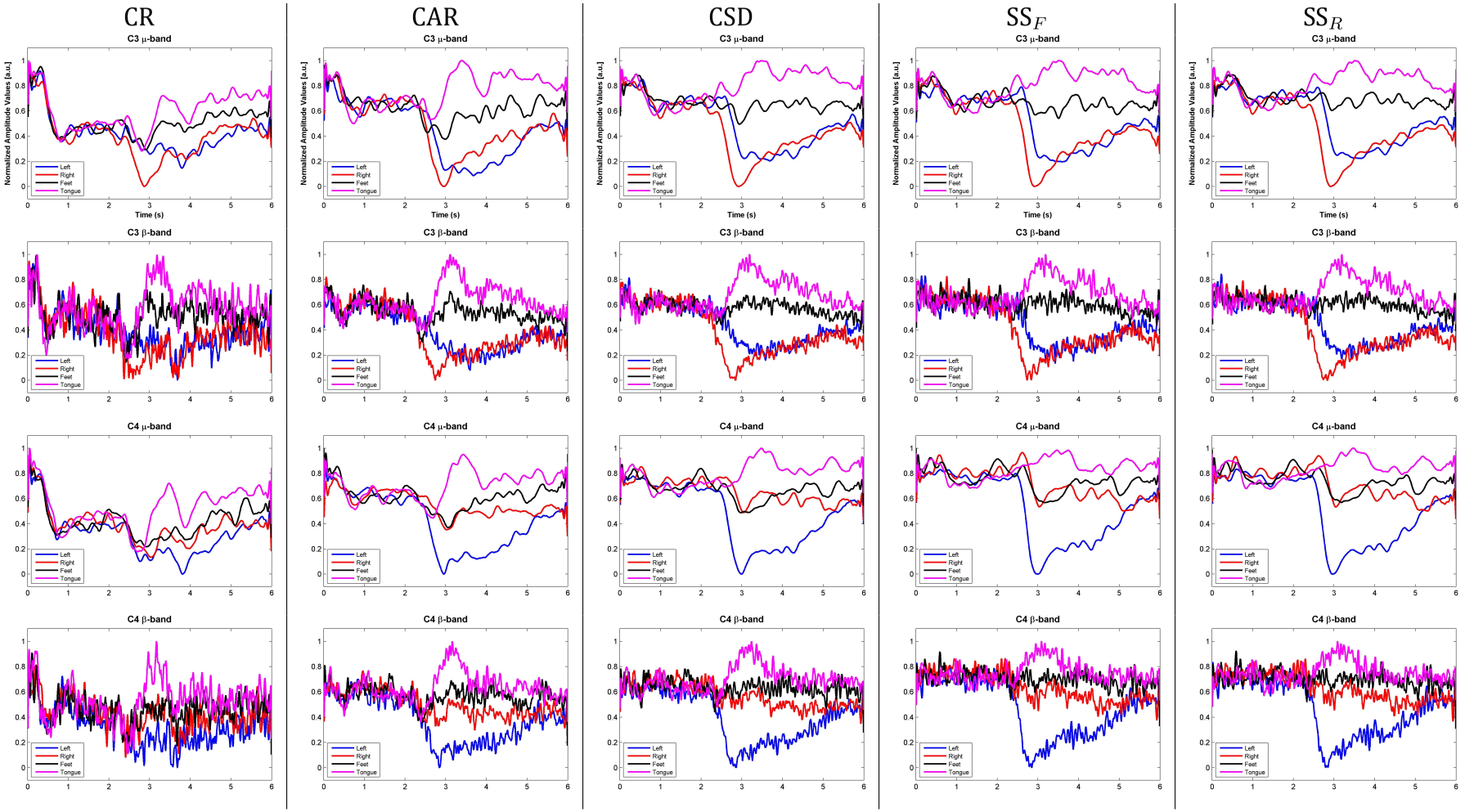

Figure 3.4: Time-Evolution plots of the bandpassed EEG signal envelopes for the μ-band and β-band of the C3 and C4 channels for the four imagery tasks. The envelopes have been computed for both rest state and MI state (0 to 6 s). The values are normalised between 0 and 1. [a.u.: arbitrary units]

3.3.2.2 BCI performances

The SVM-based classification accuracies (in %) for each pairwise binary classification task are presented in Tables 3.1. Here, the CR method has been selected as a baseline method for pairwise comparisons with other methods. Wilcoxon signed rank test reveals a statistically significant ($p < 0.05$, FDR corrected for multiple comparisons) difference between the baseline method and CSD for all the binary classification tasks except for left vs tongue whereas CAR, SS_F, and SS_R failed to provide consistent results (see Tables 3.1). Furthermore, the differences between the six binary classifications tasks were evaluated to examine if there exists a combination of two MI tasks among the four that would emerge better than others, but this evaluation showed no statistically significant difference across the six binary classification results. Table 3.2 provides the grand mean (SD) (across six binary tasks) of classification accuracies for the five referencing schemes. The subject-wise comparative results showed CSD as the better method with highest classification accuracies for eight out of nine subjects (see Table 3.2).

The overall performance across subjects and the six binary classification tasks is 78.75 ± 11.81%, 79.33 ± 11.53%, 82.36 ± 11.04%, 77.48 ± 12.23%, and 78.06 ± 11.93% for CR, CAR, CSD, SS_F and SS_R methods, respectively. By considering all the six binary tasks together, i.e. with 54 samples for each pre-processing method, pairwise comparisons indicate a significant difference between the baseline and the CSD method ($p<10e-8$). The classification accuracies for four-class BCI approach are presented in Table 3.3. The average performance across nine subjects is 52.55 ± 12.66%, 53.51 ± 11.12%, 58.14 ± 9.64%, 52.74 ± 10.49%, and 52.28 ± 9.59% for CR, CAR, CSD, SS_F and SS_R methods, respectively where the chance level accuracy is 25%. Here, the CR method has been selected as a baseline method for pairwise comparisons with other methods. Wilcoxon signed rank test reveals a statistically significant difference between the baseline method and CSD ($p = 0.0039$) whereas other comparisons failed to provide significant differences. Moreover, CSD enhances

the over-all four-class BCI accuracy by more than 5%.

Table 3.1: Classification accuracy (in %) for the configuration (22/10): Six pairwise binary classification results obtained by using linear SVM classifier. Statistical significance ($p - values$) has been estimated using Wilcoxon signed rank test.

Subj.	Left vs. Right					Left vs. Feet					Left vs. Tongue				
	CR	**CAR**	**CSD**	**SS**$_F$	**SS**$_R$	**CR**	**CAR**	**CSD**	**SS**$_F$	**SS**$_R$	**CR**	**CAR**	**CSD**	**SS**$_F$	**SS**$_R$
A01	90.97	91.67	93.06	91.67	88.19	97.22	96.53	97.92	95.83	87.50	88.19	92.36	93.06	95.83	96.53
A02	61.11	61.81	68.06	59.03	56.94	75.00	74.31	81.94	69.44	75.00	72.22	68.75	72.22	65.28	65.28
A03	90.97	87.50	93.06	90.28	93.75	86.81	88.19	90.28	88.89	94.44	93.75	91.67	93.75	88.89	87.50
A04	69.44	70.83	77.08	77.08	67.36	75.00	83.33	87.50	79.17	75.00	86.11	88.89	87.50	88.89	89.58
A05	70.83	72.22	72.22	65.97	60.42	65.28	63.19	68.06	64.58	65.97	75.69	75.00	77.08	71.53	62.50
A06	65.28	62.50	65.97	64.58	64.58	70.83	68.75	70.83	70.83	65.97	66.67	66.67	70.83	65.28	65.97
A07	68.75	70.83	78.47	64.58	80.56	81.94	85.42	88.89	83.33	84.03	94.44	90.28	90.28	90.28	84.03
A08	92.36	95.14	97.22	95.83	95.83	75.00	79.17	77.08	77.08	87.50	83.33	79.86	84.03	68.06	76.39
A09	90.28	86.81	90.28	86.81	76.39	90.97	76.39	91.67	83.33	86.81	97.22	95.14	97.92	93.06	97.22
Mean	77.78	77.70	**81.71**	77.31	76.00	79.78	79.48	**83.80**	79.16	80.25	84.18	83.18	**85.19**	80.79	80.56
SD	12.99	12.68	11.87	14.12	14.53	10.26	10.21	10.05	9.93	10.17	10.66	10.85	9.81	12.88	13.53
***p*-value**	-	0.979	0.006	0.624	0.478	-	0.949	0.004	0.869	0.820	-	0.307	0.176	0.122	0.154

Subj.	Feet vs. Tongue					Right vs. Feet					Right vs. Tongue				
	CR	**CAR**	**CSD**	**SS**$_F$	**SS**$_R$	**CR**	**CAR**	**CSD**	**SS**$_F$	**SS**$_R$	**CR**	**CAR**	**CSD**	**SS**$_F$	**SS**$_R$
A01	75.69	73.61	76.39	76.39	70.14	93.75	96.53	95.14	95.14	94.44	97.92	97.92	97.92	97.22	98.61
A02	77.78	75.69	83.33	63.89	79.86	68.75	76.39	90.28	68.75	68.75	66.67	69.44	70.83	64.58	70.83
A03	65.97	78.47	70.14	77.08	79.86	86.11	89.58	86.81	80.56	70.83	97.22	95.14	97.22	89.58	88.19
A04	68.06	71.53	68.06	67.36	70.83	83.33	87.50	93.75	90.28	90.97	76.39	86.11	84.72	84.72	72.22
A05	59.03	59.72	66.67	55.56	61.11	64.58	65.28	66.67	72.22	62.50	69.44	73.61	72.22	64.58	70.83
A06	63.89	63.19	70.83	61.81	64.58	73.61	72.92	74.31	70.83	59.03	60.42	65.28	65.28	65.97	67.36
A07	77.78	76.39	79.86	78.47	76.39	95.14	97.22	97.92	96.53	96.53	89.58	97.22	94.44	90.97	97.92
A08	85.42	84.03	87.50	70.83	71.53	72.22	74.31	77.78	82.64	77.08	65.28	62.50	68.06	56.94	86.11
A09	86.81	74.31	92.36	77.78	83.33	62.50	64.58	65.97	61.11	77.08	93.75	92.36	96.53	86.81	77.08
Mean	73.38	72.99	**77.24**	69.91	73.07	77.78	80.48	**83.18**	79.78	77.47	79.63	82.18	**83.02**	77.93	81.02
SD	9.67	7.48	9.12	8.24	7.41	12.22	12.58	12.31	12.47	13.78	15.00	14.45	13.89	14.76	12.04
***p*-value**	-	0.333	0.004	0.071	0.720	-	0.003	0.001	0.273	0.793	-	0.131	0.008	0.278	0.765

Table 3.2: Average classification accuracies (in %) for five referencing schemes across six binary tasks. The grand mean, SD and $p - values$ are estimated by considering all the six binary tasks and nine subjects together (i.e. 54 accuracy values). Statistical significance has been estimated using Wilcoxon signed rank test.

Subj.	CR	CAR	CSD	SS_F	SS_R
A01	90.62	91.44	**92.25**	92.01	89.24
A02	70.25	71.06	**77.78**	65.16	69.44
A03	86.81	88.43	**88.54**	85.88	85.76
A04	76.39	81.37	**83.10**	81.25	77.66
A05	67.48	68.17	**70.49**	65.74	63.89
A06	66.78	66.55	**69.68**	66.55	64.58
A07	84.61	86.23	**88.31**	84.03	86.57
A08	78.94	79.17	81.94	75.23	**82.41**
A09	86.92	81.60	**89.12**	81.48	82.99
Grand Mean	78.76	79.33	**82.36**	77.48	78.06
SD	11.81	11.53	11.04	12.23	11.92
***p*-value**	-	0.2067	**1.29e-08**	0.1067	0.4779

3.3.2.3 Impact of altered number of channels at preprocessing stage and feature extraction stage

The performances of three channel-selection configurations (i.e. (22/10), (10/10), and (22/22)) at the pre-processing stage and feature extraction stage, have been evaluated for CAR, CSD, SS_F, and SS_R, and the results are depicted in Fig 3.5 and Fig 3.6. The mean classification accuracies across the six binary classification tasks, for each configuration, are $79.33 \pm 11.53\%$, $76.20 \pm 11.89\%$, and $75.96 \pm 12.40\%$ for CAR; $82.36 \pm 11.05\%$, $79.69 \pm 11.99\%$, and $77.67 \pm 13.54\%$ for CSD; $77.48 \pm 12.23\%$, $75.46 \pm 12.74\%$, and $76.45 \pm 13.07\%$ for SS_F; $78.06 \pm 11.93\%$, $75.68 \pm 13.02\%$, and $77.27 \pm 12.82\%$ for SS_R. Pairwise comparisons with false discovery rate (FDR) multiple comparison correction indicated that the (22/10) system provides the best performance for both CAR and CSD while (22/22) results in worst performance. Although for SS_F, the pattern is different as we found no statistically significant difference between (22/10) and (22/22) whereas (10/10) configuration performed worst. Besides, SS_F's performance is significantly better in (22/10) when compared with

Table 3.3: Classification accuracy (in %) for the configuration (22/10): 4-class classification results obtained by using linear SVM classifiers in one-versus-rest configuration. The chance level accuracy is 25%. Statistical significance ($p - values$) has been estimated using Wilcoxon signed rank test.

Subj.	CR	CAR	CSD	SS_F	SS_R
A01	65.97	**68.05**	67.70	63.54	66.31
A02	36.46	43.06	**49.65**	44.79	42.71
A03	57.99	51.74	58.33	**59.03**	53.13
A04	50.35	57.99	**58.68**	44.79	56.60
A05	37.50	42.36	**48.26**	36.81	40.28
A06	37.85	42.71	**43.40**	42.01	40.97
A07	60.42	61.81	**66.32**	58.33	60.42
A08	56.94	44.44	58.68	**63.19**	48.96
A09	69.44	69.44	**72.22**	62.15	61.11
Mean	52.55	53.51	**58.14**	52.74	52.28
SD	12.66	11.12	9.64	10.49	9.59
***p*-value**	-	0.5313	**0.0039**	1	0.9141

(10/10). For SS_R, however, we found no significant differences across the three configurations.

3.3.2.4 Impact of the position of CSD in the EEG signal processing pipeline

The impact of the performance related to the position of CSD in the EEG signal processing pipeline was evaluated by comparing different feature extraction approaches: 1) FBCSP only, 2) CSD on the raw signal followed by FBCSP, 3) bandpass filtering followed by CSD on each frequency band and then CSP, 4) same as 3 but without CSP, i.e. with bandpower features only, and 5) CSD on the raw EEG data followed by bandpower feature extraction. The variations of performance in relation to the place of CSD in the signal processing pipeline are depicted in Fig. 3.7, by considering the set of 22 channels for pre-processing, and 10 channels for classification. In the approach 4 and 5, i.e. without CSP, the number of features is therefore 100. Across the six binary classification tasks, the average accuracy is $78.75 \pm 11.82\%$, $82.36 \pm 11.05\%$, $80.92 \pm 11.13\%$, $70.64 \pm 11.15\%$, and $70.90 \pm 11.66\%$ with the five feature extraction approaches. Post-hoc analyses with a Wilcoxon signed rank test indicated that the approach 2,

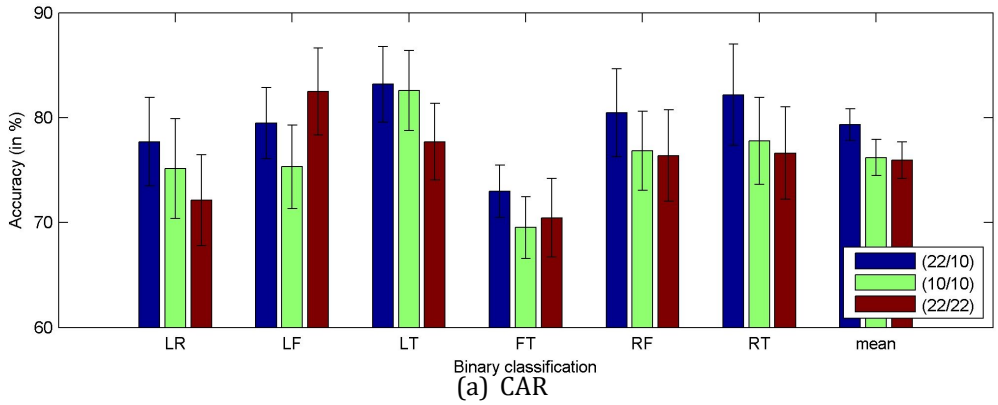

(a) CAR

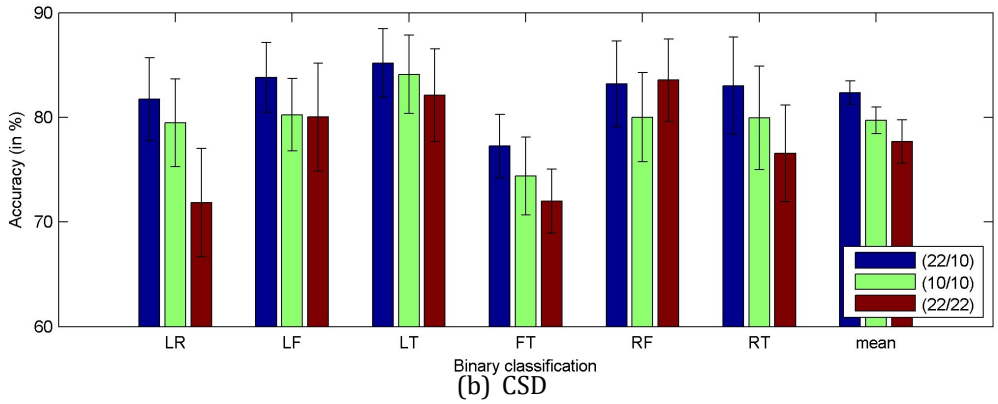

(b) CSD

Figure 3.5: Performance variation with different channel combinations during pre-processing and classification for CAR and CSD methods. The couple (Ns0/Ns1) denotes the number of sensors used for pre-processing (Ns0) and for feature extraction (Ns1). The error bars represent the standard error across subjects.

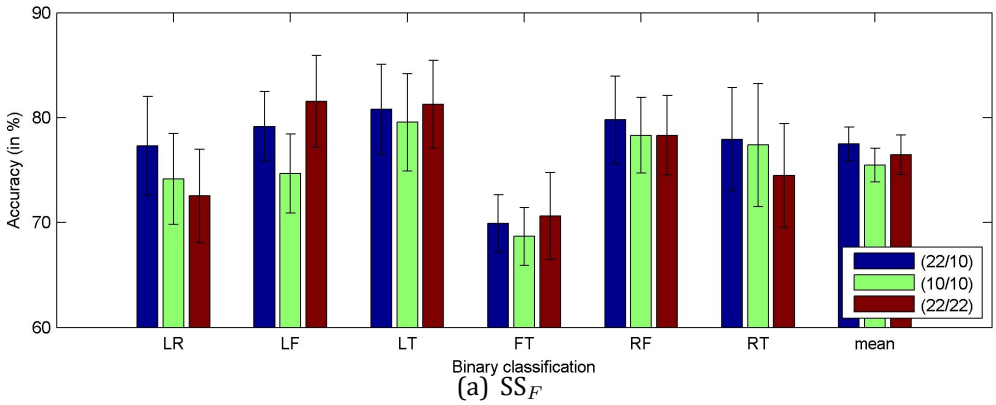

(a) SS_F

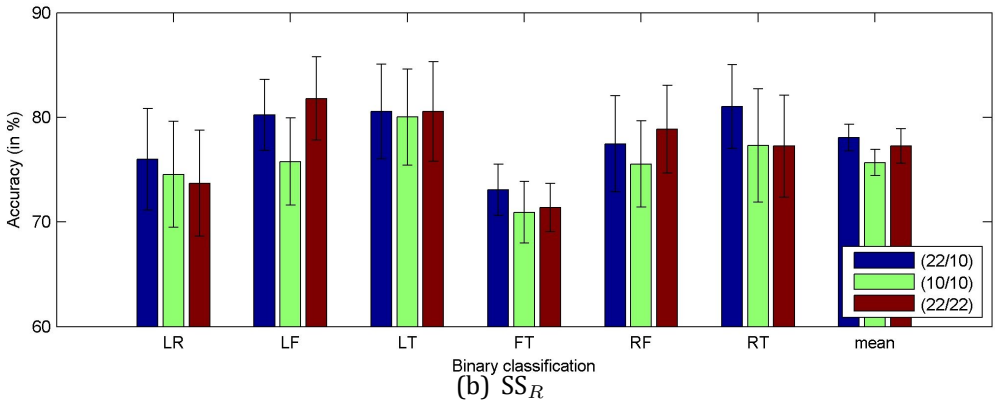

(b) SS_R

Figure 3.6: Performance variation with different channel combinations during pre-processing and classification for SS_F and SS_R methods. The couple (Ns0/Ns1) denotes the number of sensors used for pre-processing (Ns0) and for feature extraction (Ns1). The error bars represent the standard error across subjects.

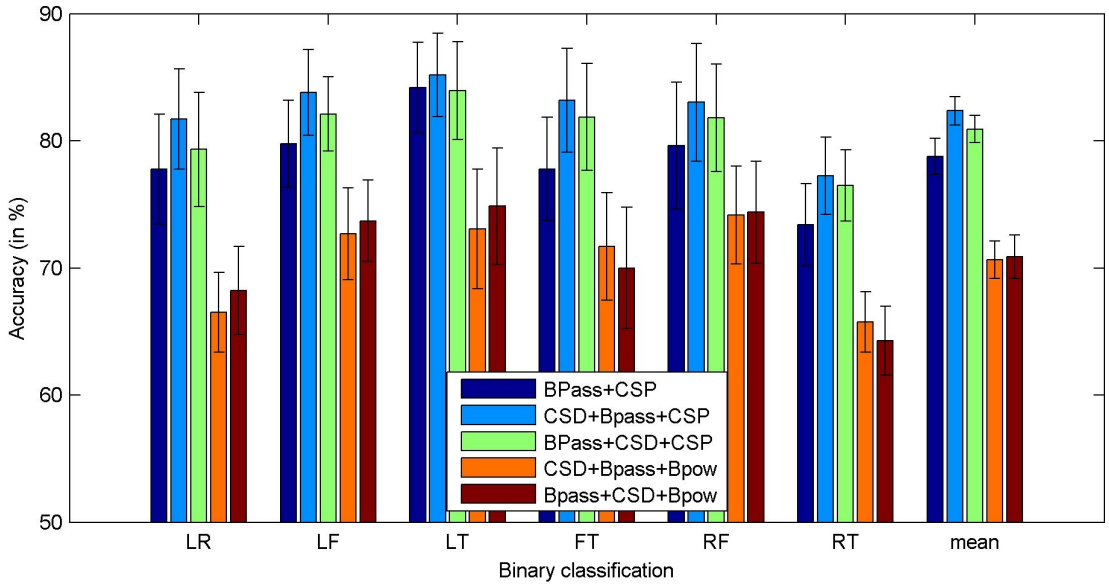

Figure 3.7: Difference of performance in relation to the position of CSD in the feature extraction pipeline. The error bars represent the standard error across subjects.

i.e. to apply CSD on the raw signal, provides the best performance among all five approaches. Without CSP, there was no difference between applying CSD after or before bandpass filtering. Finally, the results confirm the impact of CSP in the increase of the classification accuracy.

3.4 Study II: Evaluation of the impact of CSD on classification of brain connectivity features

In this analysis, we have utilised the EEG-based BCI dataset presented in Section 3.2.1 to estimate the effect of CSD on the discriminability of single-trial directed functional connectivity features related to four different MI tasks.

3.4.1 Signal processing pipeline

According to Fig. 3.8, the following steps have been implemented for this analysis: pre-processing (i.e. CSD and bandpass filtering), feature extraction (i.e. PGC measures), and classification. The initial step was the estimation of scalp CSD values from the raw EEG data. The remaining processing steps were performed separately for the raw EEG data and CSD processed data. Next, the data were bandpassed in the lower gamma (γ) frequency band (25$-$40 Hz) using a 4^{th} order, zero-phase forward and backward bandpass Butterworth filter as our recent study showed better separability of MI related connectivity values for this frequency band. For further analysis, we have selected seven EEG channels (i.e. FC1, FC2, C3, CZ, C4, CP1, and CP2) over the motor cortex region. Furthermore, the data related to the imagery tasks (i.e. 3000 ms to 6000 ms) were extracted from each trial. The extracted data were segmented using a sliding window (segment length 1000 ms and 500 ms overlap) approach. Thus, we obtained 5 segments from each trial. The windowing strategy can effectively reduce the probability of spurious causal effects due to non-stationarity in EEG signal. Time-domain PGC method was implemented with the multi-segment data to estimate the causal interactions between the scalp channel data. The coefficients of the MVAR model were estimated using the Levinson-Wiggins-Robinson (LWR) algorithm [105]. Schwarz bayesian information criterion (SBIC) [226] was used for the estimation of the optimal value of the model order o.

The analysis provides 42 ($N_s * N_s - N_s$, with $N_s = 7$ being the number of sensors) non-zero directed connectivity measures for each trial. Furthermore,

SVM classifier was incorporated to evaluate the classification performances (i.e. area under the ROC curve (AUC)) of the six binary classification tasks. The complete analysis was performed for two conditions: Firstly, the inter-session condition where the classifier was trained and evaluated on feature-sets of S01 and S02, respectively. Secondly, the intra-session condition where 10 times 10-fold cross-validation (CV) was performed for S01 and S02 separately. The computational work has been performed on an Intel Core i7-4790 with 16 GB of memory, using in-house programs written in MATLAB V8.6 (The Mathworks, Natick, MA).

3.4.2 Results

The performance is evaluated with 6 binary classifications tasks (i.e. left vs right (L↔R), left vs feet (L↔F), left vs tongue (L↔T), right vs feet (R↔F), right vs tongue (R↔T), and feet vs tongue (F↔T)) for each condition and sub-condition. Fig. 3.9 and 3.10 provide the mean AUC values with six classification tasks and their grand mean values for session S01 and S02 (intra-session condition), respectively. For this analysis, CSD provided statistically significant improvements of 12.54% ($p = 0.00014$) and 13.92% ($p = 0.00017$) in overall performances (i.e. grand mean AUCs) of session S01 and S02, respectively. The average (±SD) AUC values obtained across nine subjects for session S01 are 0.65 ± 0.11, 00.68 ± 0.09, 0.66 ± 0.15, 0.64 ± 0.09, 00.63 ± 0.15, and 0.61 ± 0.10 and session S02 are 0.67 ± 0.14, 00.70 ± 0.14, 0.66 ± 0.14, 0.64 ± 0.10, 00.65 ± 0.13, and 0.61 ± 0.08 for L↔R, L↔F, L↔T, R↔F, R↔T, and F↔T.

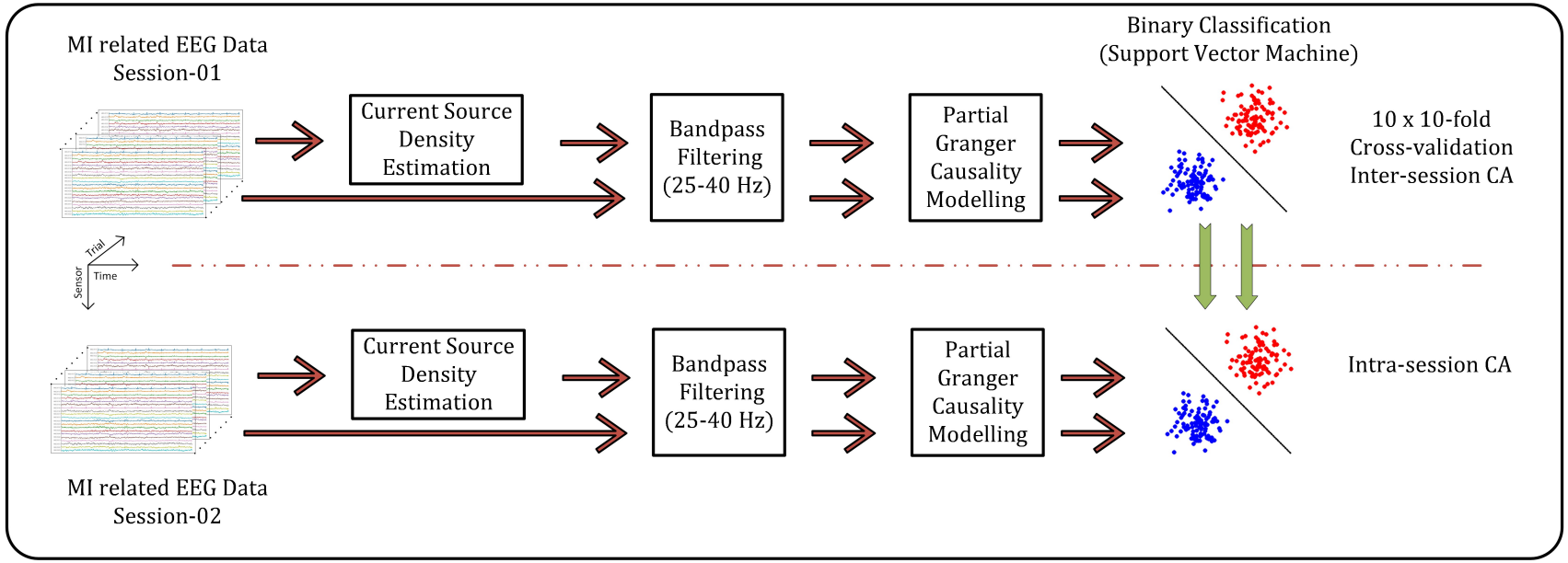

Figure 3.8: EEG signal analysis pipeline involved in study II with an overview of the different processing steps.

For inter-session analysis, the mean AUC values with six classification tasks and their grand mean value are presented in Fig. 3.11. For this condition, CSD provided statistically significant improvements of 20.28% ($p = 0.00007$) in overall performance (i.e. grand mean AUCs). The average ($\pm$SD) AUC values obtained across nine subjects are 0.69 ± 0.14, 00.73 ± 0.13, 0.73 ± 0.14, 0.68 ± 0.10, 00.71 ± 0.12, and 0.64 ± 0.07 for L$\leftrightarrow$R, L$\leftrightarrow$F, L$\leftrightarrow$T, R$\leftrightarrow$F, R$\leftrightarrow$T, and F$\leftrightarrow$T.

3.5 Discussion

Pre-processing methods are often overlooked, and the focus for improving MI-based BCI has been mainly on feature extraction techniques that maximise the difference between two classes. Although, with the present study, we found that the feature extraction methods do play a major role in improving classification accuracy, implementing efficient pre-processing techniques can further enhance the performance of a BCI system. In the first study, five different pre-processing methods, namely, CR, CAR, CSD, SS_F, and SS_R, have been compared to address their effect on the performance of FBCSP based MI-related BCI system. More particularly, we have shown that CSD provides an improvement of about 3% (in case of two-class approach) and 6% (in case four-class approach) compared to the widely used common average referencing scheme. Moreover, the study also estimates the effect of varying the number of EEG channels distinctly during pre-processing stage and feature extraction stage. As we included various distinct algorithms in our signal processing pipeline (i.e. CSD, bandpass filtering, and CSP) which can be positioned in several ways, the impact of all possible combinations, for instance, changing the position of CSD (the winning pre-processing method) and utilising the technique with and without FBCSP on the performance of MI-related BCI has also been studied. In this analysis, we have not considered the discrete methods such as the Hjorth's Laplacian [14], which is a planar scheme (i.e. subtracting the linearly-weighted potential of the nearest neighbours) as the estimates fail at the edges of a two-dimensional montage, effectively reducing the number of channels with available EEG data [19, 227]. Thus, implementation of

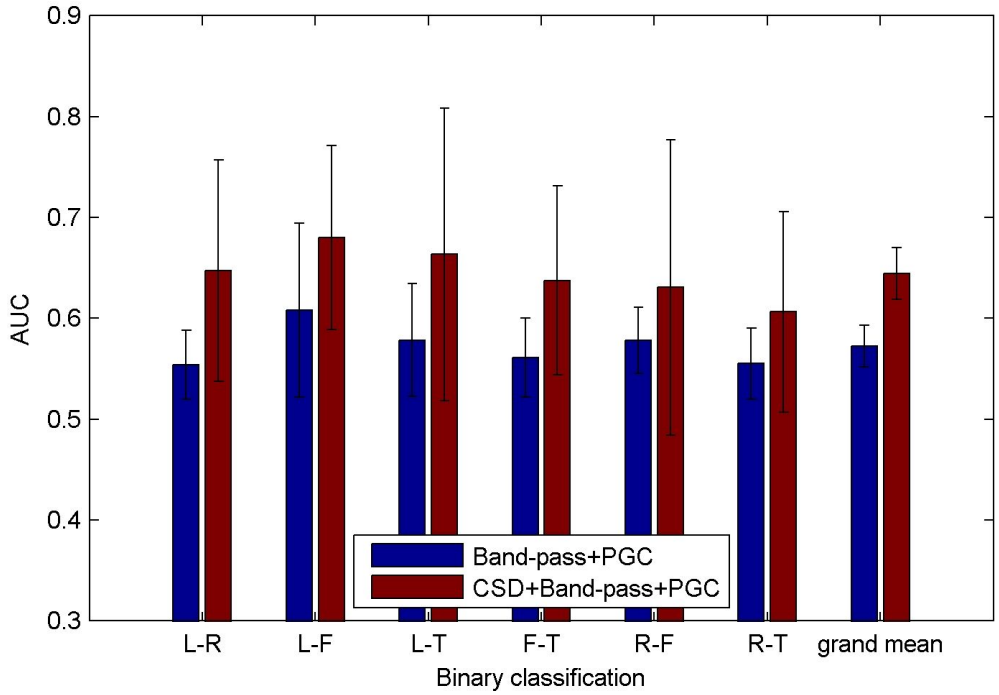

Figure 3.9: Mean AUC measures obtained from 10 times 10-fold CV with Session S01 data for six pairwise comparisons. Each tick on x-axis provides mean AUCs for the band-passed data and CSD processed band-passed data. The error bar for each of the six pairwise comparison represents the standard deviation (SD) across 9 subjects whereas the error bar for grand mean is the SD across 6 comparisons.

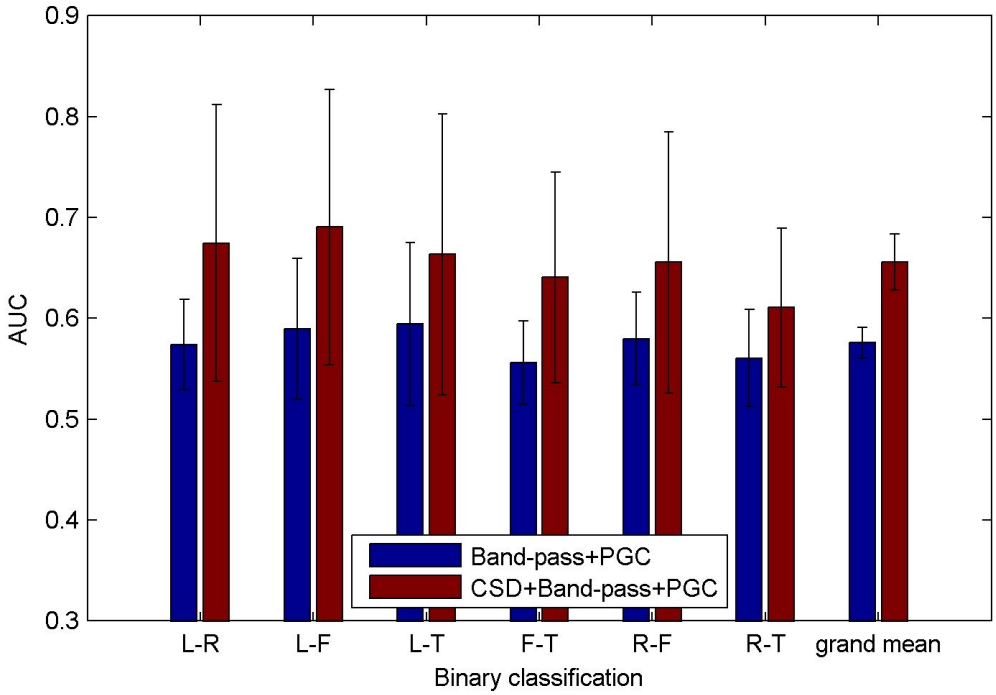

Figure 3.10: Mean AUC measures obtained from 10 times 10-fold CV with Session S02 for six pairwise comparisons. Each tick on x-axis provides mean AUCs for the band-passed data and CSD processed band-passed data. The error bar for each of the six pairwise comparison represents the standard deviation (SD) across 9 subjects whereas the error bar for grand mean is the SD across 6 comparisons.

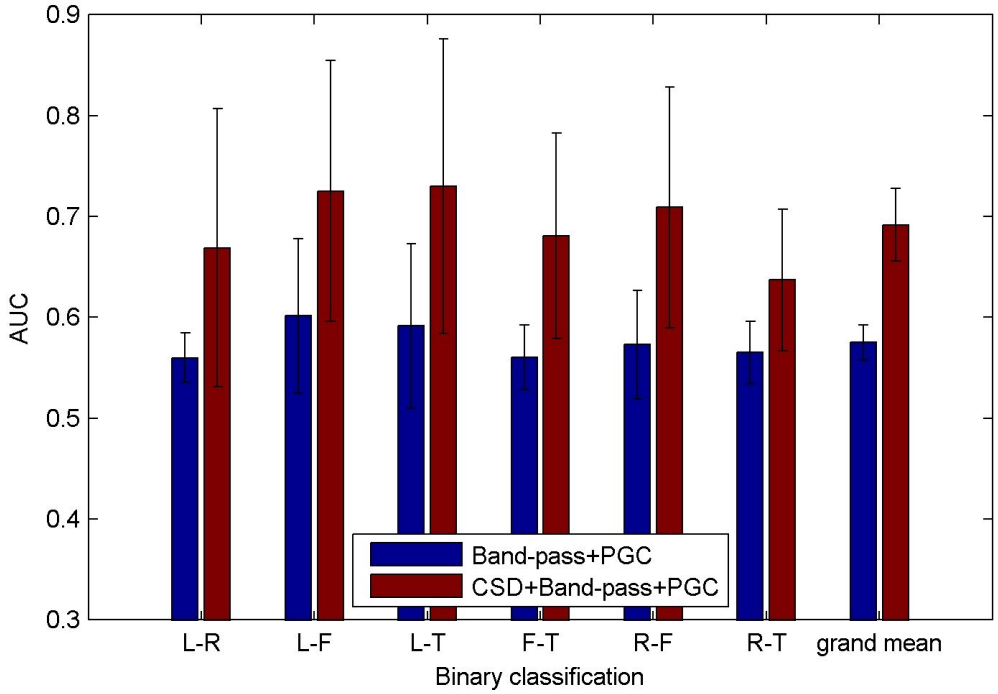

Figure 3.11: Mean AUC measures obtained from training with data of session S01 and evaluation with session S02 for six pairwise comparisons. Each tick on x-axis provides mean AUCs for the band-passed data and CSD processed band-passed data. The error bar for each of the six pairwise comparison represents the standard deviation (SD) across 9 subjects whereas the error bar for grand mean is the SD across 6 comparisons.

Hjorth's Laplacian may restrict the analysis as the availability of the pre-processed EEG channels will not be uniform across the different competing methods. Nevertheless, a study involving empirical comparison of various spatial filtering methods showed better performance of CAR as compared to small Laplacian method [58]. To extend our analysis, in the second study, we explored the effect of CSD estimation on the discriminability of single-trial directed functional connectivity features related to the EEG signals during four MI tasks.

The first study presented in this chapter yielded several major outcomes. The comparative analysis of all the six binary classification tasks and four-class classification approach for (22/10) combination showed better performance of CSD method as compared to other methods. Furthermore, the performance differences are statistically significant in five out of six comparisons. A recent study also reported a better performance of CSD as compared to SS_F and CAR method for counteracting muscular noise in scalp EEG signals [182]. Grand averaged (across all subjects and all binary classification tasks) analysis of performances showed CAR and CR as better pre-processing methods as compared to SS_F and SS_R. The results related to the impact of the number of channels for pre-processing and feature extraction (classification) indicated three key findings. First, choosing a large number of channels at pre-processing stage (possibly whole scalp coverage) and confining to the motor cortex related channels during feature extraction, yielded better classification accuracies for all the Laplacian methods as compared to other combinations. Second, the efficiency of all the methods reduced significantly with a decrease in the number of channels considered during the pre-processing (e.g. from (22/10) to (10/10)), showing the importance of acquiring the signal with a large number of channels. Third, the number of channels for classification should be reduced after the Laplacian methods as the inclusion of all the channels add redundant information to the classifier (the performance of the (22/10) was better than (22/22)). The study involving variation in the position of CSD method in EEG signal processing pipeline displayed that applying the bandpass filtering before CSD decreased the

classification accuracies in all six comparisons and hence supported the utilisation of CSD as the first step in the pipeline. Finally, CSD with FBCSP enhanced the grand mean accuracy by approximately 17% as compared to CSD without CSP. Furthermore, the results obtained from the second study confirmed significant improvements in the discriminability of the connectivity features using CSD as a pre-processing method for both inter- and intra-session conditions. Our findings complement a recent study which showed that better interpretation of the brain networks can be obtained through CSD processed EEG data [181]. The analysis found a significant reduction in the number of spurious connections with CSD [181].

3.6 Summary

VC may result in diminished separability of the EEG features for distinct cognitive tasks/processes and hence, severally affect the performance of the M/EEG-based BAPD systems. Thus, new robust pre-processing methods have to be proposed to improve the accuracy of single-trial command detection. In this chapter, the estimation of CSD is introduced as an essential pre-processing step for EEG analysis. It is shown that CSD significantly improves the distinction of related brain responses and has performed better than other referencing schemes (i.e. CR and CAR) and SSL methods (i.e. SS_F and SS_R). In addition, it is shown that selecting a large number of channels at pre-processing stage (possibly whole scalp coverage) and confining to the motor cortex related channels during feature extraction, yielded better classification accuracies for all the Laplacian methods as compared to other combinations. Furthermore, a significant improvement in the discriminability of the connectivity-based features has been achieved by introducing CSD as a pre-processing method. However, the classification accuracies with FC features are still not high enough to be suitable for a practical application. Thus, further exploration of the M/EEG FC-based features for single-trial BAPD should be undertaken. Chapter 4 addresses this limitation by introducing FC features related to mixed imagery tasks i.e. a combination of MI

and cognitive imagery (CI).

Chapter 4

Single-trial effective brain connectivity patterns enhance discriminability of mental imagery tasks

4.1 Introduction

Electroencephalography (EEG) based brain activation pattern detection (BAPD) systems (e.g. brain-computer interface (BCI)) can be implemented for a wide variety of communication and control purposes, such as controlling a cursor, wheelchair or prosthesis [228], operating virtual keyboards [229], and navigation through virtual environments [230]. These systems assert a strong positive impact on disabled users in terms of improvement in quality of life and facilitating communication with their close environment. In addition, they offer alternative means of communication for healthy users in the form of EEG controlled entertainment systems such as computer games and music [231, 232] as well as hybrid BCI systems [233]. Moreover, recent studies have shown that the use of BCI can affect neural plasticity during the period of cognitive/rehabilitative training [234], and possibly contribute to the enhancement of motor

rehabilitation for stroke patients [8]. Thus, the development of this technology benefits several research domains, e.g. medical and healthcare, neuro-marketing, entertainment and games, smart environments, and security.

The human brain has been divided into different areas based on their anatomical and physiological characteristics [235]. These areas are connected to each other to form functional brain networks that are dynamically employed to perform various sensorimotor and cognitive tasks. Analyzing these network connectivities (i.e. connectome) and their dynamics during different brain states may provide a better understanding of physiological mechanisms related to them. However, functional connectivity evaluations are unable to provide exact information regarding the directionality of the interaction, i.e. whether the information flow is from a brain area A to another area B, or vice-versa. Effective connectivity analysis can derive better relationships between two areas of interest by providing directed interactions. Therefore, effective connectivity is a relevant measure for better assessing the induced physiological variations in the brain occurring during imagery tasks. The results presented in Section 3.4.2 of Chapter 3 showed significant improvement in the performance of brain connectivity features for motor-imagery (MI) tasks using the current source density (CSD) method, however, the area under the ROC curve (AUC) values (range: 0.67 to 0.73) were still low for a practical implementation of such system.

Investigations of the connectome associated with imagination (i.e. MI) as well as the execution of motor tasks revealed the manifestation of induced activations and information flows at various cerebral structures, including, the primary motor areas (M1), the premotor cortex (PMC), and the supplementary motor areas (SMA) [189]. These cortical areas are located in close vicinity to each other making estimation of the MI task specific causal interaction a challenging task, in particular at scalp level analyses, due to the volume conduction (VC) effect. Furthermore, single-trial connectivity estimations become inherently more difficult due to a lack of sufficient EEG data for this type of analysis. These confounding factors lead to the low performance of connectivity-based MI-BCI

systems.

This chapter undertakes the research challenge presented in Section 2.7.2 of Chapter 2 and investigates the effect of imagery task type on the performance of EEG-based BAPD system which uses features of multivariate autoregressive (MVAR) model based connectivity estimates. In particular, the single-trial directed functional connectivity features are estimated to elucidate the interaction among the EEG signals during various MI (i.e. left hand imagery, right hand imagery, feet imagery, and tongue imagery) and cognitive imagery (CI) tasks (word generation imagery, spatial navigation imagery, and subtraction imagery). The rationale behind the proposed work is that CI tasks involve activations of distinct regions of the brain that are relatively far from each other compared to those associated with MI tasks.

The study undertaken in this chapter involved implementation of time-domain partial Granger causality (PGC) [84] along with two frequency domain GC measures (i.e. partial directed coherence (PDC) [110] and directed transfer function (DTF) [112]) on the two publicly available datasets. Thus, we included three different methods belonging to MVAR based modelling of time-series data. As the major aim of this study is to test the hypothesis that CI based connectivity features can provide better separability than MI-based features, an exhaustive discussion of different connectivity measures in the analysis is out of the scope of this chapter. Nevertheless, several previous studies have compared various connectivity measures with both simulated and empirical datasets [25, 236, 237]. Furthermore, we compared the PGC results with a state-of-the-art feature extraction method for BCI, i.e. log variance after spatial filtering using common spatial pattern (CSP) method.

The remainder of this chapter proceeds as follows: Section 4.2 describes the feature extraction methods, BCI datasets, data processing and analysis pipeline, and performance evaluation. Next, Section 4.3 presents the results obtained from the analysis. Finally, the results are discussed in Section 4.4, and Section 4.5 summarises the findings of this chapter.

4.2 Materials and methods

4.2.1 Multivariate autoregressive model

Given a univariate time series, its consecutive measurements contain information about the process that generated it. An attempt at describing this underlying order can be achieved by modelling the current value of the variable as a weighted linear sum of its previous values. This is an Autoregressive (AR) process and is a very simple, yet effective, approach to time series characterisation. The order of the model (i.e. the number of preceding observations used) and the weights characterise the time series. MVAR models extend this approach to multiple time series so that the vector of current values of all variables is modelled as a linear sum of their previous values [104]. The detailed description of the MVAR model is presented in Section 2.5.2.1 of Chapter 2.

4.2.2 Time-domain partial Granger causality analysis

The concept of PGC, provided by Guo et al. [84], is based on eliminating the effects of exogenous (environmental) input and latent variables during the estimation of conditional GC. The method is already described in Section 2.5.2.2 of Chapter 2 along with other variants of time-domain GC.

4.2.3 Common spatial pattern filtering

This method involves the extraction of log variance features in particular frequency bands after spatial filtering using CSPs. The CSP method is highly successful in calculating spatial filters for detecting ERD/ERS during MI tasks. The mathematical concept related to CSP is described previously in Section 2.5.1 of Chapter 2.

4.2.4 EEG dataset-1

The BCI Competition IV dataset 2A has been analysed to investigate causal interactions during various MI tasks [221]. The dataset comprised of EEG signals

acquired from nine healthy participants using a cue-based paradigm (see Fig. 4.1.A) during two sessions on different days. The MI tasks included four different classes: left hand MI (class 1), right hand MI (class 2), both feet MI (class 3), and tongue MI (class 4). Each data acquisition session consisted of 6 runs where each run comprised of 48 trials (12 trials for each class). Thus the complete study involved 576 trials from both sessions. The total trial length was 7.5 s with variable inter-trial duration. The data were acquired from 25 channels (22 EEG channels along with three monopolar EOG channels) with a sampling frequency of 250 Hz and bandpass filtered between 0.5 Hz to 100 Hz (notch filter at 50 Hz). Reference and ground were placed at the left and right mastoid, respectively.

Table 4.1: Participant details: The ID, age in years, months since occurrence and the type of event are shown for each individual of dataset-2. ASIA: American Spinal Injury Association

ID	Age	Month	Event
P1	42	6	Locked-in syndrome due to brainstem stroke
P2	31	5	Locked-in syndrome due to brainstem stroke
P3	33	2	Spinal cord injury C5, ASIA C
P4	40	255	Spinal cord injury C5, ASIA A
P5	57	5	Hemorrhagic stroke (HS) in left hemisphere
P6	43	27	Spinal cord injury C5, ASIA C
P7	20	6	HS parieto-temporal, right central no cranium
P8	36	53	Spinal cord injury C5, ASIA A
P9	38	15	Spinal cord injury C4, ASIA A

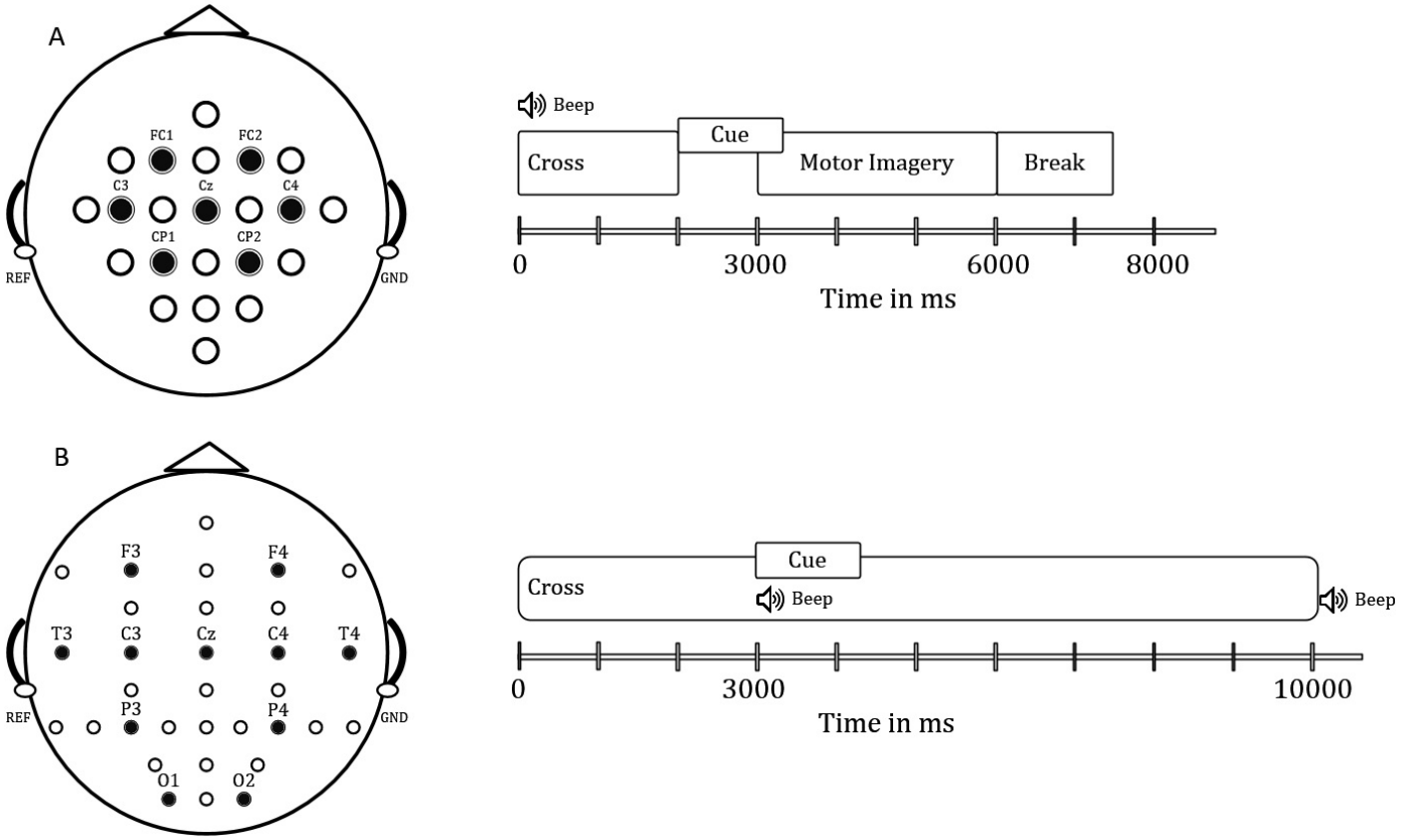

Figure 4.1: **(A)** EEG channel montage and timing of the experimental paradigm for dataset-1.Trial duration is 6 s with a break of 1.5 s between trials. Trial start is indicated with an acoustic beep and appearance of the fixation symbol. After 2 s, participants are cued for the MI task to be performed. **(B)** EEG channel montage and timing of the experimental paradigm for dataset-2. Trial duration is 10 s with a break of 2.5−3.5 s between trials. Trial start is indicated with the appearance of the fixation symbol, and the cue remains from 3 to 4.25 s. The appearance of the cue is indicated with an acoustic beep.

4.2.5 EEG dataset-2

The mental imagery-based BCI dataset has been previously analysed [238] for pairwise comparison of BCI performances during various imagery tasks. The dataset comprised of EEG signals acquired from nine participants with severe motor disabilities using a cue-based paradigm (see Fig. 4.1.B) during two sessions on different days. Demographic details of the participants are summarised in Table 4.1. For further exploration, readers are referred to the original study in [238]. The mental tasks included five different classes: word generation imagery (class 1), mental subtraction imagery (class 2), spatial navigation imagery (class 3), right hand MI (class 4), and both feet MI (class 5). The dataset consists of two different session and each session consists of 8 runs resulting in 200 trials (40 trials for each class). Thus the complete dataset includes 400 trials from both sessions. The total trial length was 10 s with variable inter-trial duration. The data were acquired from 30 EEG channels with a sampling frequency of 256 Hz and bandpass filtered between 0.5 Hz to 100 Hz (notch filter at 50 Hz) (see Fig. 4.1.B). Reference and ground were placed at the left and right mastoid, respectively. This dataset is publicly available at http://bnci-horizon-2020.eu/database/data-sets.

4.2.6 Data pre-processing and analysis

MVAR based connectivity methods are sensitive to volume conduction, thus the first step of data pre-processing involved the estimation of CSD for both datasets using the spherical spline method [220]. A recent study showed that CSD estimation improves the interpretability of connectivity results by reducing the number of spurious interactions [181]. In addition, the results presented in Section 3.4.2 of Chapter 3 showed significant improvement of classification performance by using CSD for MI tasks. Next, the channels that were noisy or severely contaminated with artefacts were interpolated for dataset-2 followed by exclusion of the bad trials. The information regarding the faulty EEG channels and noisy trials is provided in [238]. However, for dataset-1, no such information is

present, so all the available trials were considered for the analysis. For the three connectivity methods, the features were generated for delta (δ) ($1-4$ Hz), theta (θ) ($4-8$ Hz), alpha (α) ($8-12$ Hz), beta (β) ($13-25$ Hz), lower gamma (γ) ($25-40$ Hz), and wide-band ($1-40$ Hz) frequency bands whereas for CSP we included a wideband approach ($8-30$ Hz) as incorporated in the original research article [238]. Bandpass filtering was applied by employing an 8^{th} order, zero-phase forward and backward bandpass Butterworth filter. For further analysis, seven channels (C3, FC1, CP1, Cz, FC2, CP2, and C4) related to the motor-cortical areas were selected for dataset-1. Likewise, for dataset-2, 11 channels (F3, F4, T3, C3, Cz, C4, T4, P3, P4, O1 and O2) were selected for considering the frontal, temporal, central, parietal, and occipital areas of the cortex. The motive behind this implementation was to select a common network for all imagery classes.

Furthermore, the data related to the imagery tasks were extracted from each trial and for both datasets (i.e. 3000 ms to 6000 ms for dataset-1 and 3000 ms to 10000 ms for dataset-2). The extracted trials were segmented using a sliding window starting from 3000 ms to the end of the trial. For dataset-1, we extracted segments of length 1000 ms with 500 ms overlap while for dataset-2, the segment size was 2000 ms with an overlap of 500 ms. Thus, we obtained 5 and 11 segments from each trial for dataset-1 and dataset-2, respectively. The windowing strategy can effectively reduce the probability of spurious causal effects due to non-stationarity in EEG signal [86]. A longer segment may lead to better model fitting, but they are frequently non-stationary. The implemented segment lengths provided a better trade-off between satisfactory model fitting and local stationarity. The optimal size of the data segment and overlap window were obtained using a threshold criterion based on the outcomes of Kwiatkowski–Phillips–Schmidt–Shin (KPSS) test [239] (for time-series stationary testing) and Durbin-Watson whiteness test [240] (for MVAR model consistency testing). The Moreover, to counter the issues related to inter-segment variations and non-stationarity, processes of detrending and demeaning of the data were

performed wherein the average was subtracted from each segment separately along with the division of each segment by the standard deviation.

The coefficients of the MVAR model for multi-trial data were estimated using the Levinson-Wiggins-Robinson (LWR) algorithm [105]. The application of MVAR modelling for connectivity analysis requires estimation of the model order (MO) (i.e. the number of time-lags). The time-lags for an MVAR is the number of lags (previous values) of all the variables in the system to be used as regression predictors for each variable. This process is highly crucial for the correct estimation of the connectivity networks. If the MO is too high, overfitting occurs and may introduce spurious links in the network. If the MO is too low, the fitted model may fail to capture the essential dynamics of the data resulting in the exclusion of the existing links [241]. A previous study examined empirically the effect of incorrect MO selection on estimated functional connectivity networks with both simulated and real-world datasets [242]. Furthermore, the study compared the performances of various criteria available for estimating the correct MO and it suggested a cautious usage of these criteria. In this study, we implemented the Schwarz bayesian information criterion (SBIC) [226] and the Akaike information criterion (AIC) [243] for estimating the optimal value of the MO p. The expressions for these two methods are given as follows:

$$AIC(p) = \log[\det(\Sigma)] + \frac{2pL^2}{N} \tag{4.1}$$

$$SBIC(p) = \log[\det(\Sigma)] + \log(N)\frac{pL^2}{N} \tag{4.2}$$

where Σ is the estimated noise covariance matrix, L is the number of EEG channels, and N is the number of data samples. Furthermore, the MO was selected for the measure provided minimum values. During the analysis of optimum MO, we found 8 as the best MO for most of the segments (more than 75%) for dataset-1, and 10 for the majority of cases (more than 85%) for dataset-2. Hence to ensure the analysis was unbiased, we set these MO values for the complete analysis. Furthermore, we implemented two different techniques to

confirm the legitimacy of applied regression models. Durbin-Watson whiteness test [240] has been used for approximating whiteness of uncorrelated residuals. The model consistency assesses the proportion of the correlation structure that is shared by the real data and "simulated" data generated from the MVAR model. A higher consistency value (i.e. $\geq$ 80) provides a confirmatory indication for the rejection of the null hypothesis. Moreover, validation of the model was confirmed using the Ding method [86] by checking the consistency of the correlation structure. The Ding consistency test provided a higher value (nearly equal to 1), which shows that the selected MVAR model has effectively predicted the time series.

For CSP based analysis, two pairs of components (i.e. m=2) were selected for binary classification tasks. For computational assignments related to data processing, we used MATLAB (V8.1), and for estimation of single-trial connectivity and CSP features, we implemented the algorithms with in-house scripts using functions from GCCA (V2.9) toolbox [244] and HERMES toolbox [245].

4.2.7 Performance evaluation

Single-trial connectivity features were utilised to perform a total of 16 binary classification tasks for both datasets. The binary classification tasks included left-right (L−R), left-feet (L−F), left-tongue (L−T), right-feet (R−F), right-tongue (R−T), and feet-tongue (F−T) for dataset-1 and word-subtraction (W−S), word-navigation (W−N), word-hand (W−H), word-feet (W−F), subtraction-navigation (S−N), subtraction-hand (S−H), subtraction-feet (S−F), navigation-hand (N−H), navigation-feet (N−F), and hand-feet (H−F) for dataset-2. A Bayesian linear discriminant analysis (BLDA) classifier was trained on the feature sets from the data of one session (i.e. training set) while the evaluation was performed on the feature set generated from the data of the second session (i.e. evaluation set). BLDA was selected for the machine learning implementation to keep this part similar with the previous study that published

the CSP results with the same dataset [238]. This allowed us not only to replicate their results but also to compare the performance with the connectivity features. For the selection of the best time segment and the optimal number of features, cross-validation was performed during the training phase. Consequently, the computational load during the evaluation phase was efficiently reduced. We measured the classification performance with the AUC for each binary classification task [246]. Furthermore, to evaluate the best connectivity measures for each pairwise binary classification task, Pearson's correlation coefficients were estimated using data from both sessions. The absolute values of class correlation coefficients $|r(i,j,s)|$ and their significance estimators ($p-values$: $p(i,j,s)$) of each connectivity index with their corresponding dummy class labels l were estimated for each pair of classes, all segments, all subjects, and both datasets. The dummy class label is a numeric value that indicates whether a trial contains class-1 ($l=1$) or class-2 ($l=-1$) of the binary classification task. For instance, the dummy label l can be set to +1 for left-hand MI (class-1) and -1 for right-hand MI (class-1) or vice-versa. Thus, $|r(i,j,s)|$ indicates how strongly a connectivity measure can distinguish between both types of imagery classes for a channel pair (i,j) during a time segment s.

4.3 Results

This section presents several outcomes of the above analysis. Firstly, the classification performance of the three directed brain connectivity measures (i.e. PGC, PDC, and DTF) are provided for various frequency bands. Secondly, a comparative analysis is presented for PGC and CSP. Lastly, analysis of class-correlation coefficients associated with PGC connectivity features is presented for both the datasets.

4.3.1 Performance comparison of PGC, PDC, and DTF for different frequency bands (δ, θ, α, β, lower γ, and wide-band).

Fig. 4.2 presents the mean AUC values (across nine subjects) for PGC, PDC, and DTF for δ band ($1-4$ Hz), θ band ($4-8$ Hz), α band ($8-12$ Hz), β band ($13-25$ Hz), lower γ band ($25-40$ Hz), and wide-band ($1-40$ Hz) in 16 pairwise binary classification tasks involving both datasets. The first six comparisons (from left-hand side) belong to dataset-1 while the next ten comparisons belong to dataset-2. Furthermore, we compared the grand mean AUCs (across 16 binary classification tasks) for the three methods and found no statistically significant differences in δ, θ, α, β, and wide-band ($1-40$ Hz). Also, the grand mean AUC values were lower than 0.65 for all three methods for these frequency bands. Thus, the results show weak discrimination power of connectivity based features for binary classification tasks. However, interestingly, PGC performed better than PDC and DTF for the lower γ band. In this frequency band, the grand mean AUCs($\pm$ SD) for PGC, PDC, and DTF are 0.72($\pm$ 0.06), 0.62($\pm$ 0.03), and 0.62($\pm$ 0.3), respectively. In 15 out of the 16 binary classification tasks, PGC provided higher AUC values than PDC and DTF. Thus, the lower γ band with PGC provided the best classification results for both MI and CI binary tasks. The overall statistical analysis showed PGC in lower γ band performed significantly better than all the other combinations ($p < 0.025$, FDR corrected for multiple comparisons).

4.3.2 Performance comparison of PGC and CSP

The performances corresponding to PGC (in lower γ band) and a state-of-the-art signal processing technique (i.e. CSP + log variance) are presented for both datasets in Tables 4.2 and 4.3. For simplified presentation, we denote the PGC method by M_1, and CSP algorithm by M_2 in the results. For dataset-1, the statistical analysis shows significantly better performance of CSP for all six binary

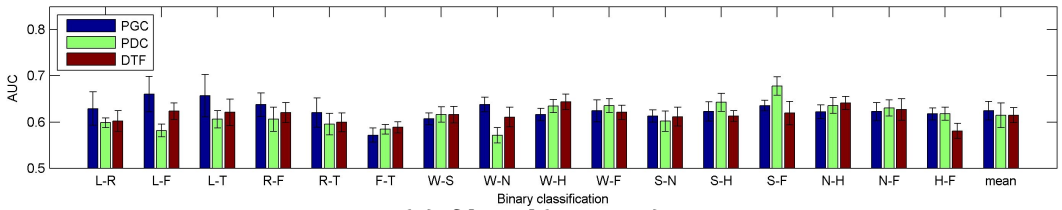

(a) δ band(1−4 Hz)

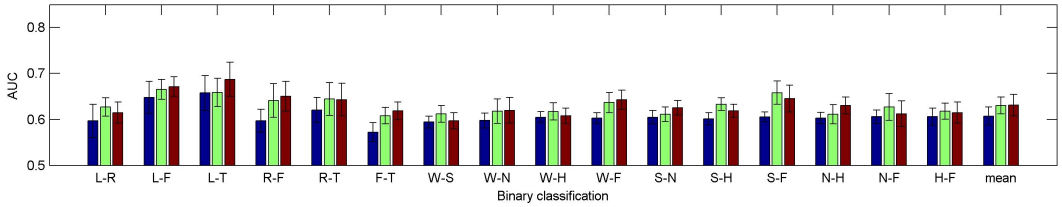

(b) θ band(4−8 Hz)

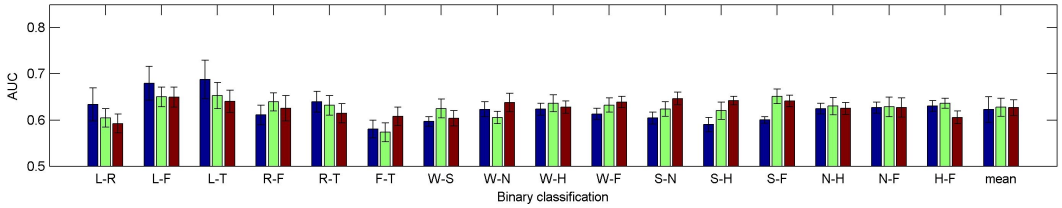

(c) α band(8−12 Hz)

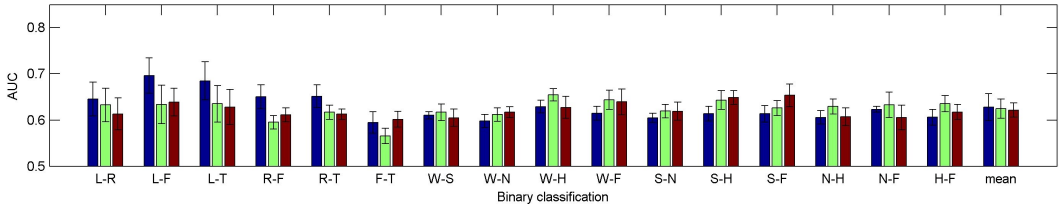

(d) β band(13−25 Hz)

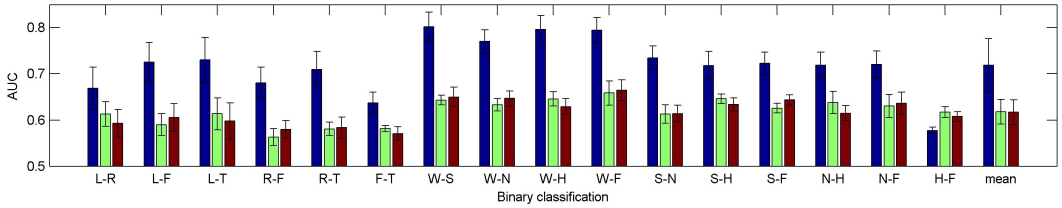

(e) Lower γ band(25−40 Hz)

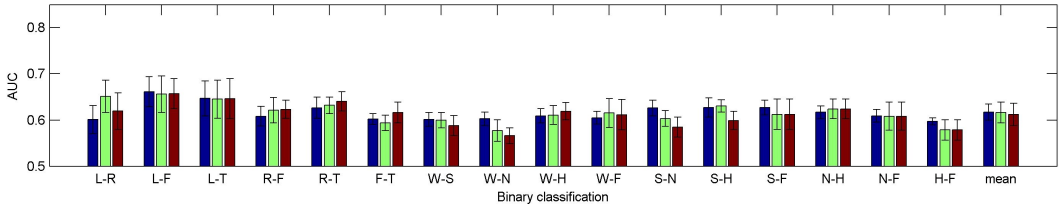

(f) Wide-band(1−40 Hz)

Figure 4.2: Mean AUC measures for PGC, PDC, and DTF with 16 pairwise comparisons for: **(a)** δ band(1−4 Hz),**(b)** θ band(4−8 Hz), **(c)** α band(8−12 Hz), **(d)** β band(13−25 Hz), **(e)** lower γ band(25−40 Hz), and **(f)** wide-band(1−40 Hz). The first six comparisons from left side belong to dataset-1 while the rest belong to dataset-2. The error bars represent the standard error across subjects.

classification tasks ($p < 0.05$). For dataset-2, the mean AUCs of eight out of ten binary classification tasks are better in the case of PGC however we found statistically significant differences in two cases only, i.e. W$-$S ($p = 0.039$) and W$-$N ($p = 0.01$), where improvements of 14$\%$ and 10$\%$ in mean AUC($\%$) are obtained, respectively. Furthermore, we compared the performance of different MI pairs for PGC results. The comparative analysis for dataset-1 (with FDR corrected p-value (p=0.026)) shows some interesting results wherein both L$-$F ($p = 0.004$) and L$-$T pair ($p = 0.023$) provided significantly better AUCs ($\%$) as compared to F$-$T. Besides, the MI task pair F$-$T had the worst overall performance whereas L$-$F and L$-$T performed best among the six binary classifications. For dataset-2, group statistical analysis (with FDR corrected $p - value = 0.025$) showed significantly better performance of PGC during W$-$S, W$-$H, and W$-$F as compared to S$-$N (p=0.021, p=0.011, p=0.019), S$-$H (p=0.007, p=0.003, p=0.007), S$-$F (p=0.007, p=0.004, p=0.004), N$-$H (p=0.004, p=0.007, p=0.007), N$-$F (p=0.011, p=0.003, p=0.007), and H$-$F (p=0.004, p=0.007, p=0.004).

Additionally, the outcome for W$-$H (p=0.011) is significantly better than W$-$N. In terms of average AUC($\%$) values, W$-$H and W$-$S performed best and H$-$F performed worst among all ten binary classification tasks. This analysis followed the most practical classification procedure for a BCI setting, i.e. training and evaluation with data from different sessions. However, to further explore the performances of the two competing methods and to evaluate the variations between two sessions, we estimated the 10-fold cross-validation results for the data of session-1 and session-2 separately, and for the combined data of session-1 and session-2. The mean AUCs across subjects for session-1, session-2, and combined data are presented for both datasets in Fig. 4.3(a) for the CSP method and in Fig. 4.3(b) for the PGC method. Although we found a slight increase in the grand mean AUC values for session-2 compared to session-1, the difference is not statistically significant. Moreover, for all three cases, CSP outperformed PGC for dataset-1 involving MI tasks while the latter outperformed CSP for dataset-2

involving both CI and MI tasks.

Furthermore, we estimated the outcomes by combining PGC and CSP features together. BLDA classifier was trained on the collective feature set of session-1 data and evaluated with combined feature-set of session-2 data. The mean AUC values (across all subjects) generated with CSP, PGC, and the combined features are presented for dataset-1 and dataset-2 in Fig. 4.4 and Fig. 4.5, respectively. Here, we compared the performance of the combined feature set with the best approach found for each dataset, i.e. CSP for dataset-1 and PGC for dataset-2. For both datasets, we found no statistically significant difference during the comparisons. However, the difference between the grand mean AUC values with the combined feature set and PGC is higher for dataset-2 compared to the difference between combined and CSP features.

Table 4.2: Comparison of the AUC (%) between PGC in lower γ (M_1) and the log-variance of CSP features (M_2) approach for the dataset 1.

Subjects	1		2		3		4		5		6		7		8		9		Mean±SD	
	M_1	M_2	M_1	M_2	M_1	M_2	M_1	M_2	M_1	M_2	M_1	M_2	M_1	M_2	M_1	M_2	M_1	M_2	M_1	M_2
L-R	73	92	51	67	82	99	56	79	63	66	54	73	59	79	74	99	91	97	67 ± 14	83 ± 14
L-F	88	99	61	78	81	93	66	83	60	63	61	68	68	95	70	85	96	98	73 ± 13	85 ± 13
L-T	94	99	52	72	81	96	67	85	64	74	60	74	75	92	70	97	95	99	73 ± 15	88 ± 11
R-F	88	99	69	83	81	96	64	92	62	67	59	69	68	98	61	91	60	66	68 ± 10	84 ± 14
R-T	93	100	60	72	88	99	65	89	64	72	61	71	71	95	72	92	65	86	71 ± 12	86 ± 12
F-T	61	67	60	78	76	74	58	75	58	66	58	69	65	77	63	86	74	82	64 ± 7	75 ± 7

Table 4.3: Comparison of the AUC (%) between PGC in lower γ (M_1) and the log-variance of CSP features (M_2) approach for the dataset 2.

Subjects	1		2		3		4		5		6		7		8		9		Mean±SD	
	M_1	M_2	M_1	M_2	M_1	M_2	M_1	M_2	M_1	M_2	M_1	M_2	M_1	M_2	M_1	M_2	M_1	M_2	M_1	M_2
W-S	63	79	73	62	89	70	82	69	87	76	72	62	85	66	91	56	80	57	80 ± 9	66 ± 8
W-N	58	58	81	69	79	79	73	71	79	67	80	71	81	68	80	64	81	58	77 ± 8	67 ± 7
W-H	57	56	82	66	82	73	75	83	80	96	86	63	81	56	86	68	86	83	80 ± 9	71 ± 14
W-F	61	68	79	70	78	65	76	80	81	83	86	73	79	67	88	66	88	76	79 ± 8	72 ± 7
S-N	59	65	80	66	71	73	64	66	76	69	72	55	81	77	78	62	80	60	73 ± 8	66 ± 7
S-H	51	90	64	57	80	65	70	75	74	82	77	63	76	65	80	76	74	85	71 ± 9	73 ± 11
S-F	57	89	66	58	75	66	72	71	73	76	74	52	78	64	82	81	74	63	72 ± 7	69 ± 12
N-H	58	62	72	53	60	63	71	81	74	77	70	55	80	60	82	63	79	67	72 ± 8	65 ± 9
N-F	57	68	76	60	59	56	73	89	77	60	69	75	80	60	81	59	76	76	72 ± 9	67 ± 11
H-F	58	58	60	54	61	57	54	60	57	77	59	60	58	52	57	52	56	65	58 ± 2	60 ± 8

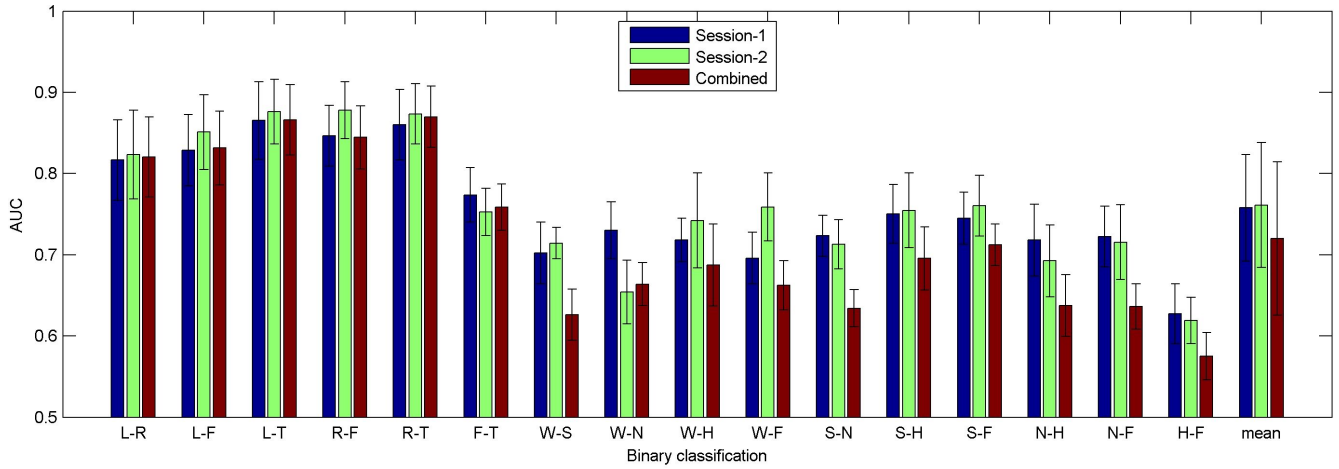

(a) CSP

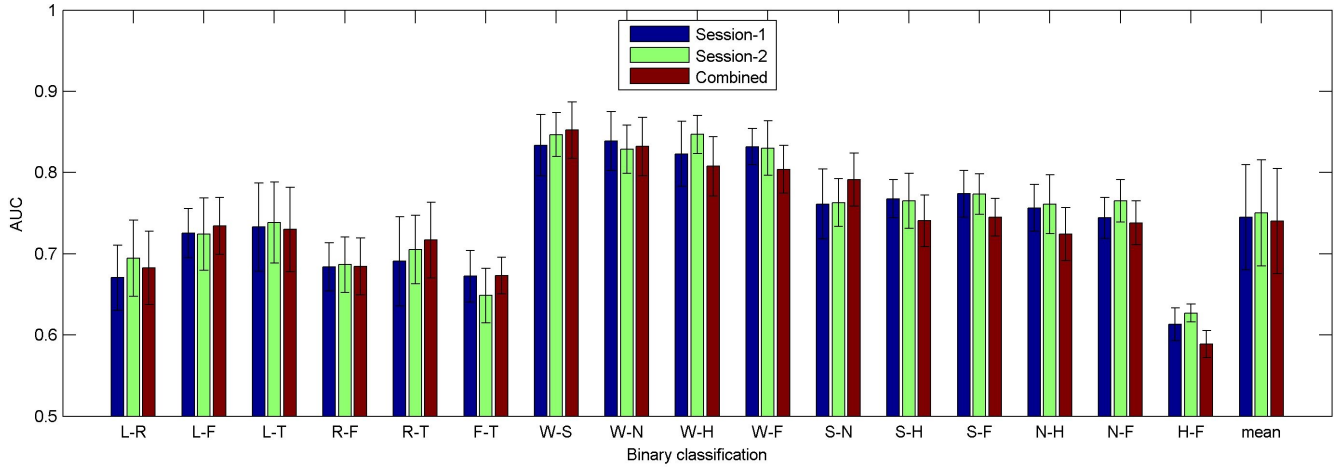

(b) PGC

Figure 4.3: Mean AUC measures (across subjects) estimated by 10-fold cross validation classification with session-1, session-2, and the combined data involving 16 pairwise comparisons for: **(a)** CSP method, and **(b)** PGC method. The first six comparisons from the left side belong to dataset-1 while the rest belong to dataset-2. The error bars represent the standard error across subjects.

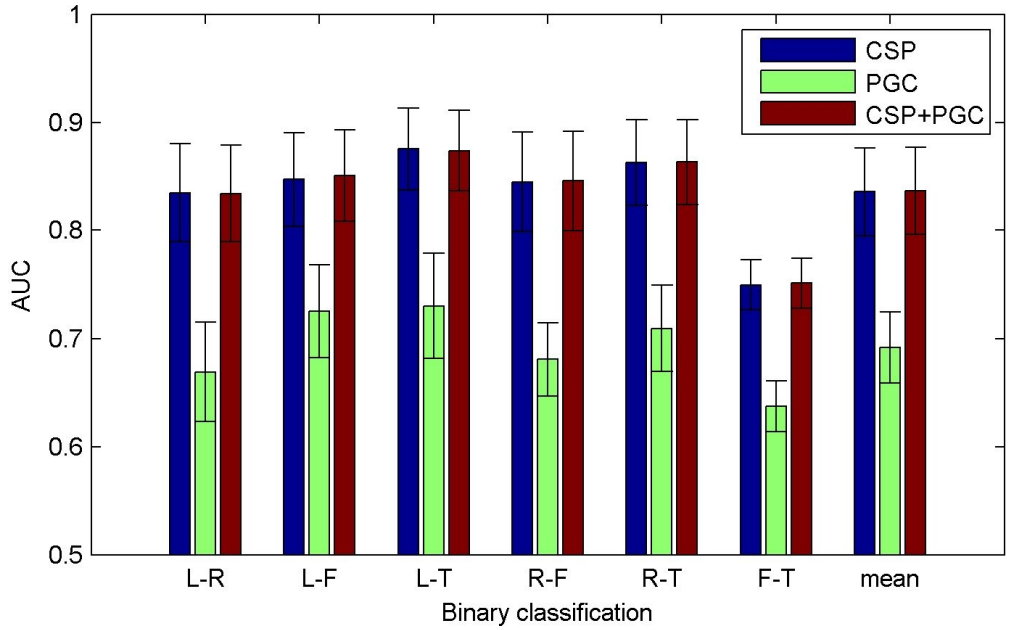

Figure 4.4: Mean AUC measures (across subjects) estimated for dataset-1 involving six pairwise binary comparisons with only CSP features, PGC features, and with combination of CSP and PGC features. The error bars represent the standard error across subjects.

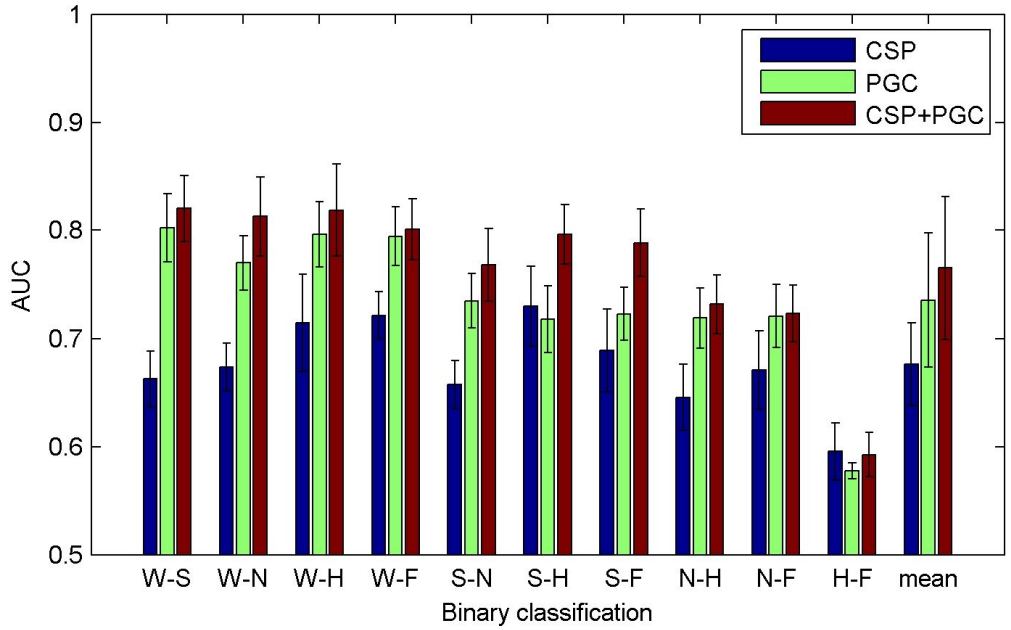

Figure 4.5: Mean AUC measures (across subjects) estimated for dataset-2 involving ten pairwise binary comparisons with only CSP features, PGC features, and with combination of CSP and PGC features. The error bars represent the standard error across subjects.

Table 4.4: Directed connectivities with statistically significant class-correlation coefficients ($r > 0.5$ and $p < 0.00045$, Bonferroni corrected) for each binary classification task on dataset-2.

	Relevant Connectivities
W-S	(P3→F4), (C4→C3), (C3→Cz), (C4↔Cz), (C3→C4), (F4→T4)
W-N	(C3→F4), (P3→F4), (T4→C4), (C4→T4), (P3→T4), (F4→P3), (C4→P3)
W-H	(Cz→F3), (Cz→F4), (P3→F4), (C3→Cz), (C4→Cz), (F3→C4), (T4↔C4), (C3→P3), (C3→P4), (C3→O1), (C3→O2)
W-F	(P3→F3), (F4→T3), (F4→C3), (P3→C3), (F3→C4), (P3→C4), (P3→T4), (P3→P4), (F4→O1)
S-N	(C4↔Cz), (T4↔C4), (P3↔T4)
S-H	(Cz→F3), (C4→C3), (T4→C3), (P4→C3), (F3→Cz), (C3→O1)
S-F	(Cz↔F3), (C4→C3), (T4→Cz), (C3→O1), (C3→O2), (Cz→O2)
N-H	(O2→F4), (P3→C3), (T4→Cz), (P3→Cz), (O2→C4), (O2→O1)
N-F	(O2→F4), (O2→C4), (T4→P3), (O2→P3), (O2↔O1)
H-F	Nil

4.3.3 Class-correlation analysis of the connectivity features

The absolute values of the class-correlation coefficients were averaged across all subjects and both sessions for each dataset separately. Next, for each pairwise comparison, the averaged values of these estimates were normalised between 0 and 1 to evaluate the significance of different connectivity indices within each binary classification task. Finally, the class-correlation matrices were generated using the normalised estimates. These normalised estimates are presented in Fig. 4.6 and Fig. 4.7 for six pairwise comparisons of dataset-1 and ten pairwise comparisons of dataset-2, respectively. Each matrix element represents directional connectivity from the i^{th} column (source) to the j^{th} row (sink). Table 4.4 illustrates the significant connectivity indices with $r > 0.5$ for various binary classification tasks for dataset-2.

Furthermore, we scrutinised the indices with majority voting criterion, i.e. selected only those features which maintain the r-value threshold (i.e. 0.5) for at least 5 subjects out of 9. We found no connectivity feature above the set threshold and the voting criterion for dataset-1. However, we can assess the most contributing connectivity features for dataset-1 with Fig. 4.6, for instance, CP1$\rightarrow$C4, C3$\rightarrow$FC1, and C4$\rightarrow$Cz for L$-$R, CP1$\rightarrow$C4, C3$\rightarrow$C4, and C3$\rightarrow$CP1 for L$-$F, C3$\rightarrow$C4, Cz$\rightarrow$C4, and C3$\rightarrow$CP1 for L$-$T, C3$\rightarrow$Cz, and C3$\rightarrow$FC1 for R$-$F, C3$\rightarrow$FC1, and Cz$\rightarrow$C3 for R$-$T, and finally CP1$\rightarrow$FC1, Cz$\rightarrow$CP2, Cz$\rightarrow$C4, Cz$\rightarrow$CP1,and Cz$\rightarrow$FC1 for F$-$T. For dataset-2, we found a significant association of frontal scalp area with W$-$S, W$-$N, W$-$H, and W$-$F binary classification tasks. Likewise, the parietal area is more associated with W$-$N, W$-$H, and W$-$F while occipital area seems to be more activated during N$-$H, N$-$F, and S$-$F. Interestingly, central area electrodes contributed to almost all the binary classification tasks. Temporal lobe contributed majorly to W$-$N, S$-$N, and W$-$F binary classification tasks. However, we found no significant connectivity indices for the H$-$F binary classification task.

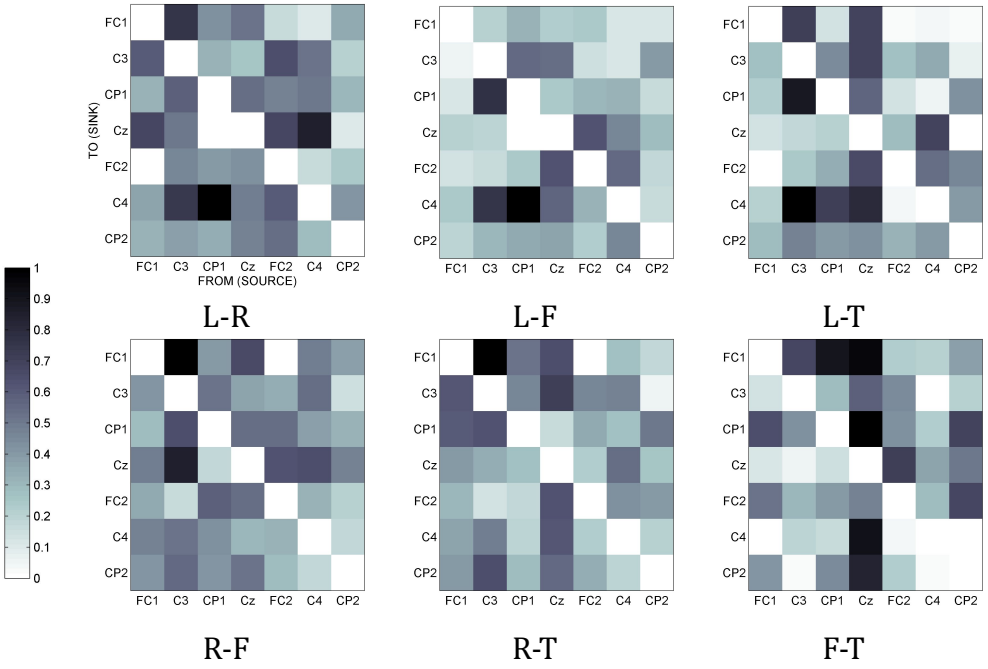

Figure 4.6: Class-correlation matrices for each pairwise comparison for dataset-1. The absolute values of the class correlation coefficients for all subjects and sessions were averaged and normalised between 0 and 1 for each binary classification task pair separately. Each matrix element represents directional connectivity feature from the i^{th} column (source) to the j^{th} row (sink).

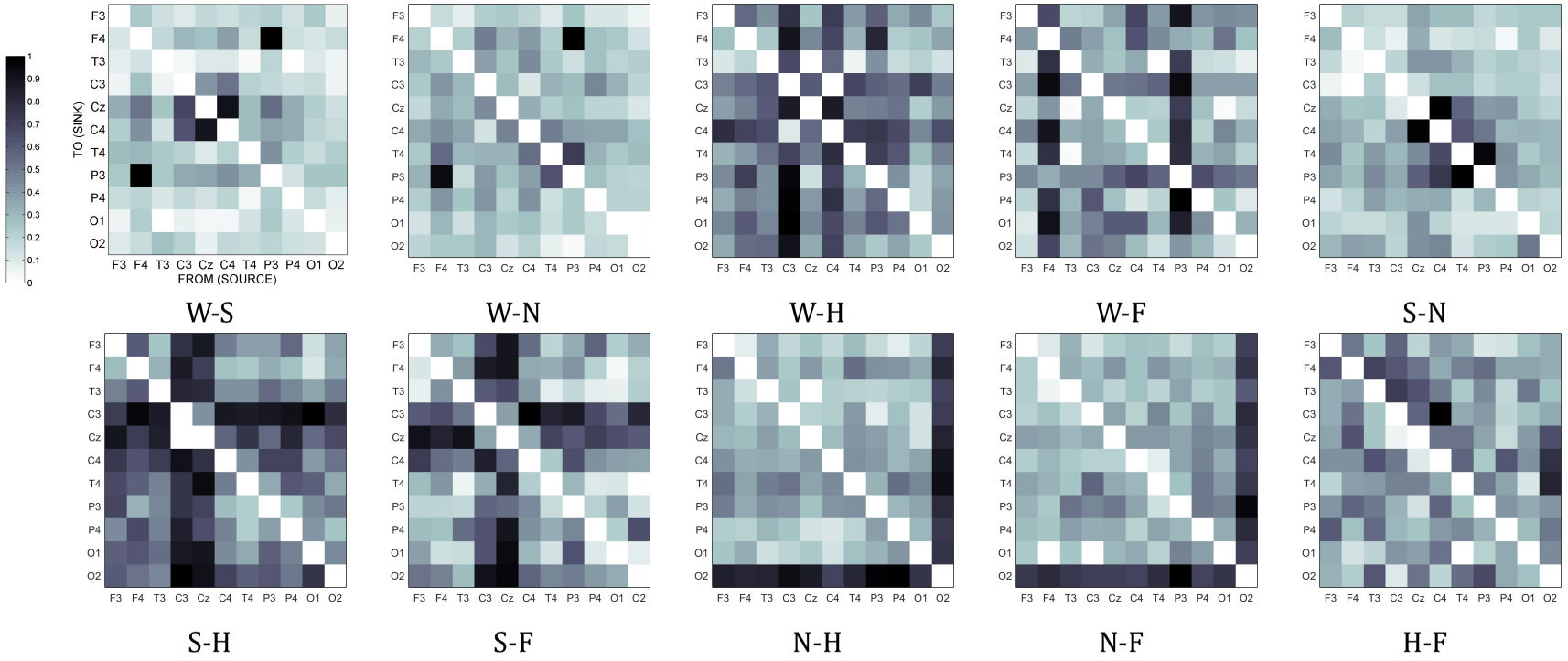

Figure 4.7: Class-correlation matrices for each pairwise comparison for dataset-2. The absolute values of the class correlation coefficients for all subjects and sessions were averaged and normalised between 0 and 1 for each binary classification task pair separately. Each matrix element represents directional connectivity feature from the i^{th} column (source) to the j^{th} row (sink).

4.4 Discussion

Most of the connectivity based single-trial BCI studies focus on MI related modulations in the motor cortex functional network. Investigations of the brain connectome related to imagination and execution of motor tasks revealed the exhibition of induced activations and information flow at various cerebral structures, incorporating M1, PMC, and SMA [247]. These cortical areas are located in close vicinity to each other making discriminative estimation of the MI task related causal interactions a challenging task, in particular at scalp level analyses. Thus, the performances of the MI-based BCI systems using connectivity features are typically low. In this study, we presented an alternative solution to overcome this confounding factor by employing CI features, including word generation, spatial navigation, and mathematical tasks. The rationale behind this hypothesis is that these imagery tasks activate distinct brain regions, which are relatively far from each other.

In this chapter, we have considered PGC, DTF, and PDC to generate effective connectivity features in six frequency bands, i.e. δ, θ, α, β, lower γ, and wide-band using two publicly available imagery-related BCI datasets. Next, to obtain the best performing method and optimum frequency band, we compared the results for 16 binary classification tasks involving MI and CI. Moreover, we compared the performances of PGC method and CSP algorithm by evaluating the results of binary classification tasks for both datasets. Our analysis yielded four major findings. First, we obtained higher discriminative connectivity features in the lower γ band as compared to the rest of the canonical frequency bands (i.e. δ, θ, α, β, and wide-band). Second, the performance of PGC is significantly better than PDC and DTF in the lower γ band. Third, and more importantly, the PGC and CSP comparative analysis showed significantly high improvement in classification performances with effective connectivity based features for mixed imagery tasks (i.e. CI versus MI) as compared to MI tasks. Finally, the post-hoc analysis showed higher values of class correlation coefficients for connectivity features in binary classification tasks involving word generation, spatial navigation and subtraction

task compared to MI tasks.

The results of the current analysis illustrate that lower γ frequency range holds greater information regarding cortical interactions during various brain imagery tasks than α and β frequency ranges. It is worth noting that we have included the low-frequency γ range (i.e. $25-40$ Hz) to avoid the muscular artefacts as these are more prominent at higher frequencies. However, high-frequency broadband gamma may capture better information related to the brain responses and can be seen in electrocorticographic (ECoG) signals. Nevertheless, these findings are consistent with several prior studies. A transfer entropy based brain connectivity study suggested strongest modulation in the γ band during MI task [24]. Similarly, detection of high-frequency activations in motor cortex during motor execution and imagery was reported using invasive modalities including electrocorticography (ECoG) [248] and non-invasive recording methods including fMRI [249]. Furthermore, two recent studies presented high correlation between the high-frequency range of ECoG signal with spatially focal BOLD peaks in primary sensorimotor areas [250] and in pre and post-central areas (i.e. covering the motor area) [251]. However, it is evident that the signal to noise ratio is a significant issue when dealing with high frequencies in EEG signals. To mitigate the effect of muscular noise, we implemented CSD estimation as a pre-processing method [220]. A similar study involving various MVAR based connectivity measures reported low accuracies of PDC and DTF for MI-based BCI system [25]. Moreover, the theoretical formulation of PDC and DTF is based on standard GC measure while the PGC method enhances the efficiency of conditional GC measure by mitigating the effect of confounding factors (i.e. latent variables and exogenous inputs) using a concept similar to partial correlation [84]. A recent study provided evidence supporting the higher accuracy and consistency obtained with PGC compared to conditional GC and PDC approaches in identifying causal connectivity of neural circuits with both simulated and empirical datasets [99].

A major challenge in BCI is to increase the information transfer rate (ITR) as

the brain-computer interaction competes with other modalities (e.g. eye-tracking) particularly for people who are not entirely locked-in. The increase of the number of commands, i.e. the increase of the imagery tasks, that can be accurately selected at any moment can improve the ITR. The findings of this chapter have shown that while the performance of features based on effective connectivity remains below the existing methods for MI tasks, these type of features provide a robust performance for other types of imagery tasks such as CI. Finally, because the choice of the easiest imagery tasks may be subject dependent, the results show that the choice of the feature extraction method must be based on the selected imagery tasks.

4.5 Summary

Discrimination of brain evoked responses corresponding to imagery tasks is a challenge for both the person who has to imagine a specific task and the signal processing methods that have to extract robust discriminant features. Most of the previous studies have focused on MI tasks (e.g., left vs right) by using features based on the bandpower or log-variance of bandpass signals after spatial filtering. While this approach remains successful for the classification of MI, we have shown that the use of features based on effective connectivity using PGC in the gamma band can lead to more reliable performance in specific imagery tasks, i.e. word generation, numerical subtraction, and spatial navigation tasks. The results demonstrate that the performance of the proposed system is superior to the performance achieved with a state-of-the-art method for MI (i.e. CSP). Finally, the results also suggest that the combination of different imagery tasks opens the scope for improved BCI based on the detection of imagery tasks by increasing the number of possible classes.

One of the major application fields of M/EEG-based brain activation pattern detection (BAPD) systems (e.g. BCIs) is upper-limb (UL) stroke rehabilitation [27, 28, 8, 29]. However, neurophysiological effects of the attained recovery is still poorly understood. Chapter 5 aims to explore the patterns based

on M/EEG functional brain networks (FBNs) in order to better understand the process of stroke recovery and to assess the clinical efficacy of the M/EEG based UL stroke rehabilitation.

Chapter 5

Brain-machine interface driven post-stroke upper limb functional recovery correlates with beta band mediated cortical networks

5.1 Introduction

Recovery of movement related functions after stroke and its assessment are highly crucial for restoring activities of daily living (ADLs) of the patients. Majority of the stroke survivors have upper-limb (UL) associated symptoms after undergoing an acute stroke [190]. Many patients show some degree of spontaneous (autonomous) recovery during initial months following a stroke, however, this is generally inadequate particularly in terms of motor functions. The condition of the patients with null or incomplete recovery can be improvised with several restorative therapy methods. These methods mainly include: (i) dynamic splinting which helps the stroke survivors to straighten their wrists and fingers (e.g. physical therapy, constraint-induced movement therapy, gait therapy) [149, 150], (ii) electrical muscle stimulation which helps in moving weak limb by using electrical impulses delivered directly to skin using

electrodes [160, 161], (iii) device-driven therapy which guides the users to execute repeated movements (e.g. robotics, brain-computer interface (BCI)) [156, 157, 158, 159], (iv) transcranial magnetic stimulation which uses electromagnetic induction to induce weak currents and helps in causing activity in specific parts of brain [162, 163], and (v) mirror therapy: to make it appears as if stroke survivors are moving their affected arm, however, they actually look at the movement of their unaffected hand [252, 253]. These days mental practice (MP) and physical practice (PP) are two frequently used evidence-based clinical interventions to enhance UL motor function purportedly to improve motor movement, coordination, and balance following stroke [254, 255].

Motor-imagery (MI) based BCI systems offer the use of neuronal signals (i.e. electroencephalography/magnetoencephalography (M/EEG)) for UL rehabilitation goals, by providing the end users with brain state-related neuro-feedback through various means such as functional electrical stimulation, virtual reality environments, or robotic systems. Taking this into consideration, BCI systems that are applied for motor neuromodulation purposes are used to induce activity-dependent plasticity by making the user pay close attention to a task requiring the activation or deactivation of specific brain areas [256, 65, 214].

Section 2.7.3 of Chapter 2 presented a major research challenge related to the evaluation of the neurophysiological mechanisms related to UL functional recovery attained during a longitudinal stroke rehabilitative intervention provided through a motor attempt (MA)-based BCI-driven hand-exoskeleton.

We estimated the brain connectivity networks using resting-state (RS) MEG signals acquired at five different sessions in conjunction with a multi-modal rehabilitative therapy provided with the simultaneous intervention of MA-based BCI and robotic hand-exoskeleton over a period of up to 6 weeks. This study included five sessions of functional recovery assessment involving Action Research Arm Test (ARAT) and grip-strength (GS) measurements. Further, to assess the neuronal mechanisms related to the stroke recovery obtained from BCI-driven robotic hand-exoskeleton, the associations between the estimated

brain networks of the RS MEG data and the functional recovery outcomes are evaluated. Moreover, a detailed investigation into these neuronal mechanisms is reported in this chapter.

The remainder of this chapter is organised as follows: Section 5.2 provides the detailed description about the participants, rehabilitative intervention, assessment of hand functional recovery, and acquisition and connectivity analysis of RS MEG data. Section 5.3 illustrates the outcomes of the hand functional recovery assessment, BCI performance in terms of classification accuracies, and the RS MEG connectivity analysis. Section 5.4 provides a detailed review of the outcomes and impact of the studies undertaken in this chapter. Section 5.5 concludes the chapter.

5.2 Materials and methods

5.2.1 Participants

Five stroke (ischemic) survivors (3 females, 2 males, age 61.6 ± 5.32 years (range $56-69$ years)) who had persistent coordination deficit of the UL were enrolled for an uncontrolled clinical trial. The clinical trial is retrospectively registered at the ISRCTN registry with the registration number *ISRCTN13139098*[1]. The mean time after stroke was 21.8 ± 4.49 months (range $17-28$ months). Table 5.1 provides the demographic information of all the participants. Four participants were first-time stroke victims. All participants provided written informed consent for their participation and this study was approved by the University Research Ethics Committee of the Ulster University, Northern Ireland, UK. All research procedures were carried out in accordance with approved institutional guidelines and regulations.

[1] http://www.isrctn.com/ISRCTN13139098

Table 5.1: Participant details: The Id, age, sex, affected hemishpere, mini-mental state examination (MMSE) score, time since stroke, baseline ARAT score, baseline GS score and affected brain location are shown for each participant. *P05 had to leave the intervention after initial 2 weeks of the intervention.

Participant ID	Age (years)	Sex	Affected Upper limb	MMSE score	Time since stroke (months)	Baseline ARAT	Baseline GS (Kgs)	Most affected brain location
P01	56	M	Left	30	28	6	11.7	Right middle cerebral artery
P02	69	F	Right	28	24	29	13.7	Left frontal lobe peri-ventricular and basal gangalia region
P03	60	F	Right	28.5	22	35	3	Left side of pons
P04	65	F	Left	27	18	24	12	Thalamus
P05	58	M	Right	28	17	26	13.3	Brainstem
Mean (SD)	61.6 (5.3)			21.8 (4.5)	28.3 (1.1)	24 (10.9)	10.7 (4.4)	

Inclusion criteria were as follows: ischemic stroke resulting in UL disability, time since stroke onset greater than 6 months, age between 18−80 years (both inclusive), and no history of neurological condition. Exclusion criteria were as follows: severe deficits in cognition (Mini-Mental State Examination (MMSE) score <21), claustrophobic, pregnant or breastfeeding, and metal or active body implants. This study involved a liberal approach while considering the effect of handedness of participants on the overall improvement of the physical outcomes and hence recruited the participants without considering the handedness of the affected arm. As one of the participants (i.e. P05) had to leave the intervention after initial 2 weeks of the intervention, the data of the participant is excluded from the analysis.

5.2.2 Intervention

In this study, we have conducted a clinical trial comprising of a rehabilitative intervention to four hemiparetic stroke patients who underwent the same intervention for a period of upto 6 weeks. The intervention consisted of two stages. The first stage was the PP stage of 30 min followed by an MP stage of almost 46 min including the BCI calibration time of around 16 min. This PP and MP based neurorehabilitation protocol was inspired by an earlier work on BCI based UL rehabilitation producing effective motor recovery [8].

During PP stage a home-grown hand-exoskeleton device provided repetitive finger grasping and extension exercise to the affected hand in assist-as-needed mode. The assist-as-needed strategy was implemented by a force threshold based switching between active non-assist and passive assistance mode. The applied finger-tip force by the participants was converted into exoskeleton motion using an impedance model when the force is above a certain threshold level (active non-assist mode). The controller goes into a passive assistance mode providing full assistance to complete the on-going finger grasping/extension action when the applied force is below the threshold. The difficulty level of the PP was adjusted by updating the impedance parameters of the controller, according to

the average force generation ability of the participant in a session.

In the MP stage the participants were given a hybrid-BCI based multimodal neurofeedback contingent to the simultaneous activations in the EEG and electromyography (EMG) signal measured by a spectral bandpower correlation between the two [257]. Fig. 5.1 depicts the timing and structural details of MP stage of the intervention. In one particular session of the MP, there were five runs of approximately 7 min 3 s each consisting of 40 trials. Each trial starts with a 3 s rest period, followed by the presentation of a cue to perform either a left or right-hand grasp attempt. Although the cue remains for 2 s, the participants were asked to perform the task until 5 s after the presentation of the cue. Among the 5 runs, first 2 runs were for calibrating the BCI system and the subsequent 3 runs were for giving online neurofeedback based on the EEG-EMG pattern classifier trained during the calibration stage. For the online neurofeedback runs, visual and proprioceptive feedbacks were provided through the screen and hand-exoskeleton, respectively, during the last 3 s of the task period. The exoskeleton was worn in the impaired hand of the participant, whereas the other hand was placed on a softball on top of the table. During the task period of the trials, the participants were asked either to perform the grasp movement with the hand-exoskeleon with impared hand or with softball with unimpaired hand and the subsequent visual feedback was provided in both cases. It is to be noted that the participants had not gone for any kind of physiotherapy (PT) or occupational therapy (OT) during the course of the intervention.

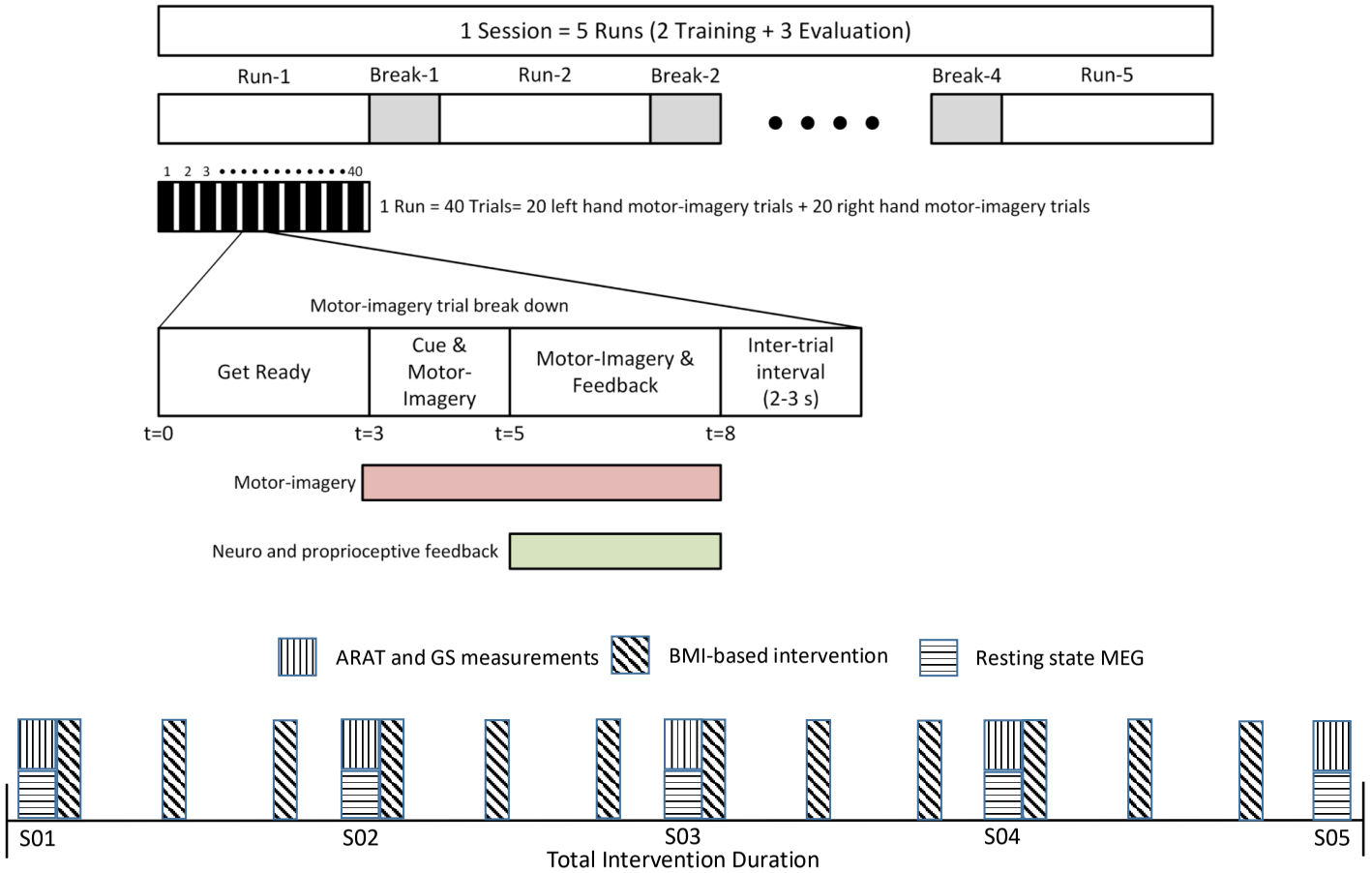

Figure 5.1: A detailed description of proposed EEG and MEG data acquisition paradigm. The upper section provides the description of the BMI paradigm. The lower section presents the timings of BMI-based intervention, rehabilitation outcome assessment (i.e. ARAT and GS), and RS MEG data acquisition over the total duration of the rehabilitative intervention (upto 6 weeks). ARAT, GS, and RS MEG were recorded at five different sessions (S01−S05).

5.2.3 Assessment of upper-limb functional recovery

Each participant underwent the ARAT [258] and GS assessment at five different times during the complete duration of the intervention (see Fig. 5.1). The ARAT is a standardised ordinal scale for the assessment of 4 basic UL movements i.e. primary grasp (score range: $0-18$), grip (score range: $0-12$), pinch (score range: $0-18$), and gross movements of flexion and extension at the elbow and shoulder (score range: $0-9$). GS (in Kg) was assessed using a hydraulic hand dynamometer which gives accurate and repeatable GS readings. The hydraulic hand dynamometer provides five different positions to accommodate variable hand sizes and features a range of 0 to 200lb (90kg). While GS is used to directly describe strength of the UL, it may also indicate the level of overall upper extremity strength.

5.2.4 MEG data acquisition

All the participants were screened for any metallic foreign substance e.g. jewellery, coins, keys or any other ferromagnetic material before entering the magnetically shielded room. The standard fiducial landmarks (left and right pre-auricular points and Nasion), five head position indicator (HPI) coils (placed over scalp), and the additional reference points over the scalp were digitised (Fastrak Polhemus system) to store information about the participants' head position, orientation, and shape. In addition, ocular and cardiac activities were recorded with two sets of bipolar electro-oculogram (EOG) electrodes (horizontal-EOG and vertical-EOG) and one set of electrocardiogram (EKG) electrodes, respectively. Before starting the data acquisition, the complete procedure and the experimental paradigm were described to the participants.

Ten minutes of resting-state MEG data (i.e. five minutes each for eyes-open and eyes-closed) were recorded with a 306-channel (102 magnetometers and 204 planar gradiometers) Elekta Neuromag™ system (Elekta Oy, Helsinki, Finland) located at the Northern Ireland Functional Brain Mapping (NIFBM) Facility of the Intelligent Systems Research Centre, Ulster University. During the

eyes-open experiment participants were instructed to remain relaxed but alert with their eyes open and fixated on a red cross presented at the centre of the screen. The fixation point was displayed on a Panasonic projector with a screen resolution of 1024×768 and refresh rate of 60 Hz. All recordings were made with participants seated in upright position in the scanner.

The MEG signals were filtered at a bandwidth of $0.1-330$ Hz (online) and sampled at the rate of 1 kHz during the acquisition itself. Continuous head positioning was switched on after 20 s of raw data recording and kept running for rest of the acquisition period.

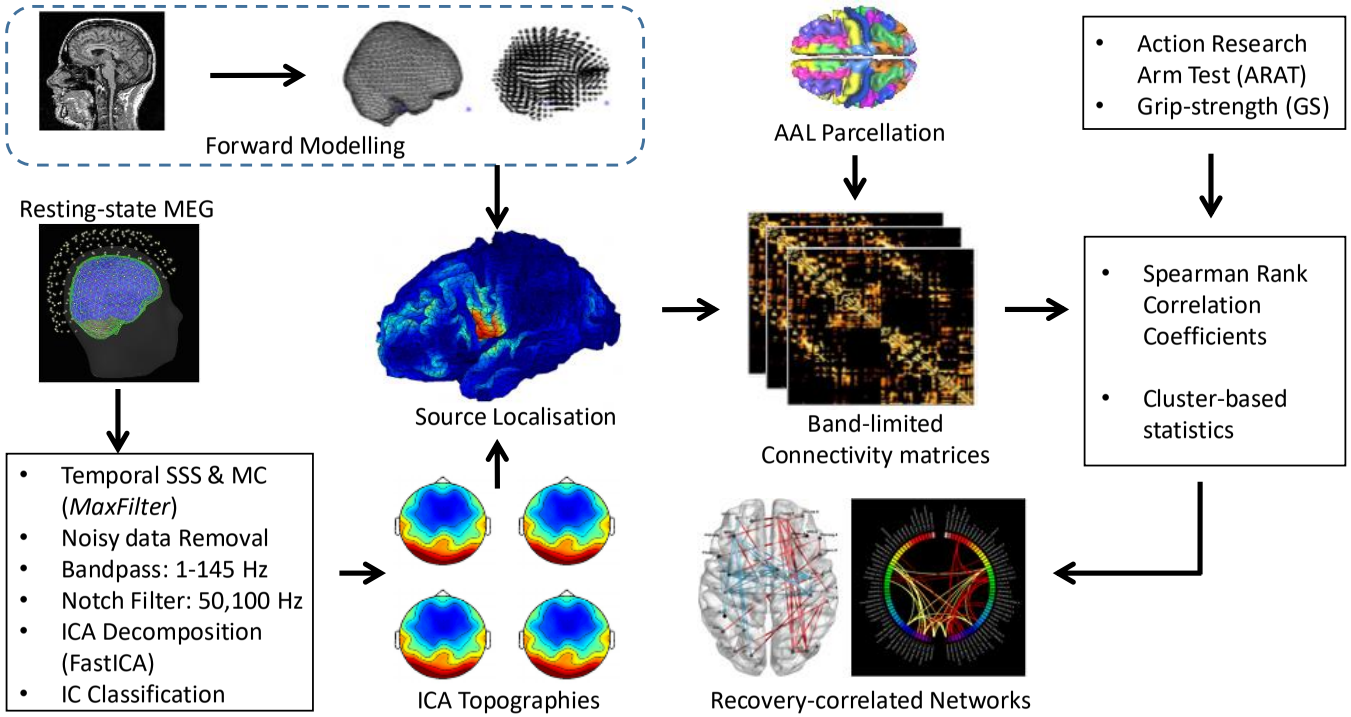

Figure 5.2: Schematic diagram representing the signal analysis pipeline. From top left corner: Resting state MEG data were preprocessed and then, decomposed to independent components (ICs) using FastICA. Further the IC classification was performed to obtain brain-related ICs. The topographies of brain ICs and forward model created from the structural MRI were utilised for source localisation of the MEG data. Further, band-limited voxel-based functional connectivity networks (FBNs) were generated and converted to ROI-based networks using automated anatomical labelling (AAL) atlas. Next, cluster-based statistics was implemented to obtain the recovery-correlated functional sub-networks.

5.2.5 MEG analysis

The MEG analysis consists of following steps:

Pre-processing and independent component analysis: During the rehabilitative intervention, a total of five sessions of MEG datasets were recorded for each participant. As several participants reported episodes of sleep during eyes-closed paradigm, only RS eyes-open MEG data have been included for further analysis. The recorded datasets were visually examined for strong muscular movements, and then processed for head movement correction wherein HPI signal-based compensation was carried out using an inbuilt software, i.e. Maxfilter in the ELEKTA MEG system (Elekta Neuromag Oy, version 2.2.15). The environmental interferences and constant or periodic artefacts were corrected by applying the temporal extension of signal-space separation (t-SSS) method with default parameters and after exclusion of bad channels [259]. Further to this point, data processing was performed using the FieldTrip toolbox [224] and Matlab 9.2 (64 bit version, R2017a, Mathworks, Natick, USA).

The data were bandpass filtered over $1-145$ Hz and notch filtered at harmonics of 50 Hz (i.e. 50 and 100 Hz). Artefacts related to squid jump, clip, and muscular movements were identified and removed. The cleaned data were then decomposed into independent components (ICs) by means of the FastICA algorithm [260] and ICs related to EOG and EKG were identified using an in-house algorithm based on correlation and coherence methods. Before running the IC decomposition, the data were resampled to 500 Hz to reduce the computational load. The remaining ICs were further categorised into brain and non-brain ICs using their multiple characteristics (e.g. fit with 1/f spectrum, flat spectrum quantification, and time kurtosis) in time and frequency domains [261, 262]. The whole process was repeated 20 times and the iteration with highest number of brain ICs was selected for further analysis.

Source localisation: The IC sensor maps were projected onto the individual participants' brain via a localization procedure carried out by means of a linear inverse method. The T1-weighted structural magnetic resonance images were

obtained from each participant's health records after obtaining their consent. Further, the structural MRI of the participants' head was co-registered to the MEG coordinates using the three fiducial points and the scalp points acquired before the MEG data acquisition. A single shell volume conduction model was created based on the segmentation of the head tissues. The structural data was further processed using FreeSurfer [263, 264] and MNE suite [265] involving triangulation of the cortical surfaces with dense meshes with ∼4,000 vertices in each hemisphere. This allows for the definition of the source space, that is, a regular 2D grid within the single shell head model, sampled into 8126 voxels corresponding to a spacing of approximately 8 mm between adjacent source locations. A geometrical registration of the MEG sensor array to a coordinate system referred to the participants' head was performed by using functional landmarks (i.e. nasion and pre-auricular points). The m_c brain IC sensor maps were scaled to norm one. An amplitude restoring factor α_i, to be subsequently used in the forward model of data formation, is defined such as $a_{ci} = \alpha_i \widetilde{a_{ci}}$, where $\widetilde{a_{ci}}$ indicates the i^{th} IC sensor-level map after scaling. Next, the scaled IC sensors maps were projected onto the source space via a weighted minimum-norm least squares (WMNLS) inverse method [266, 267]. Thus, the brain IC source maps q_i are obtained from the sensor maps as follows:

$$q_i = W^{-2} L^T (L W^{-2} L^T + \lambda I) \widetilde{a_{ci}} \tag{5.1}$$

where i runs over the subset of the m_c brain ICs, W is a diagonal weighting matrix of size $[3k \times 3k]$, the elements of which are defined by $W_{kk} = ||L||$, L is the lead-field matrix of size $[n \times 3k]$, I is the identity matrix of size $[n \times n]$, and λ is a regularization parameter set on the basis of the noise level [268]. In this analysis pipeline, the regularization parameter was optimised separately for each IC. This is an important difference with respect to WMNLS localization of artifact-corrected recordings. After the localization step, m_c source maps in participants' space were obtained. In addition, an affine transformation has been applied to the source maps for a coordinate transformation to an MNI stereotaxic space. This allowed spatial

comparison across participants.

Once the component topographies had been projected on to the source space, the activity at each voxel at each sample in time was obtained as a linear combination of the component time courses weighted by their related brain source map.

Functional brain network estimation: For the estimation of functional connectivity networks from the source localised MEG data, we used an extension of the imaginary part of coherence, namely the Multivariate Interaction Measure (MIM) [269, 270], that maximises the imaginary part of coherence between a given reference voxel (seed, s) and any other voxel (target, j). More specifically, the estimated MEG signal at each brain voxel is a vector quantity that can be represented through its components in a given reference system. MIM is designed to maximise the imaginary part of coherence between vector quantities. The mathematical details on MIM derivation can be found in [269]. For the readers' convenience, we briefly review MIM definition in the following.

Given the vector Fourier transformed signals as a function of frequency f at the seed and target voxels: $X_s(f)$ and $X_j(f)$, respectively, and introducing the compact notation $X(f) = [X_s^T(f) X_j^T(f)]$, the cross-spectrum (C(f)) between the two vectors $X_s(f)$ and $X_j(f)$, can be written in the block form:

$$C(f) = \langle X(f) X(f)^* \rangle \tag{5.2}$$

$$C(f) = \begin{bmatrix} C_{ss}^R(f) + JC_{ss}^I(f) & C_{sj}^R(f) + JC_{sj}^I(f) \\ C_{js}^R(f) + JC_{js}^I(f) & C_{jj}^R(f) + JC_{jj}^I(f) \end{bmatrix} \tag{5.3}$$

and MIM between s and j is thus defined as:

$$MIM_{sj} = tr\left((C_{ss}^R)^{-1} C_{sj}^I (C_{jj}^R)^{-1} (C_{sj}^I)^T\right) \tag{5.4}$$

In the above notation, tr indicates matrix trace, the T subscript indicates matrix transpose, superscripts R and I denote the real and the imaginary parts,

the $(\cdot)^{-1}$ subscript indicates matrix inverse, the $*$ subscript indicates matrix conjugate transpose, and the capital J indicates the imaginary unit. A more detailed recapitulation of the method is also given in Marzetti et al. (2013) [270].

In this work, cross-spectra were estimated with Fast Fourier analysis after signal linear de-trending and Hanning windowing and were averaged using time epochs of 1.0 s duration with 50% overlap leading to a frequency resolution of 1 Hz. The number of averaged epochs is approximately 550 for each dataset. The method, being based on the maximization of imaginary coherence, largely overcomes the well-known limitation to the study of functional connectivity by EEG/MEG posed by signal mixing artifacts, i.e. any active source in the brain contributes, in a weighted manner, to the signals measured at all sensors through volume spread (see Figure 2A in [271]). This effect constitutes an especially severe confound for estimates of brain interactions [272, 273, 274, 275] and needs to be taken into account by mapping MEG functional connectivity through robust measures. Thus, voxel-wise whole brain networks in various frequency bands i.e. delta ($1-4$ Hz), theta ($4-8$Hz), alpha ($8-15$ Hz), beta-low ($15-26$ Hz), beta-high ($26-35$ Hz), gamma-low ($34-49$ Hz), gamma-mid ($51-76$ Hz) and gamma-high ($76-120$ Hz) were obtained using MIM with the reconstructed neuronal time-series. Furthermore, these voxel-based networks were parcellated to ROI-based networks using AAL [276] atlas restricting the further analysis to 78 cortical regions and 12 sub-cortical brain regions. This process was implemented for all the MEG sessions and each participant to generate respective FBNs.

5.2.6 Cluster-based statistical testing

For estimating the overall upper limb functional recovery, we first estimated a composite recovery score by taking a weighted mean of the GS measure and the total ARAT score i.e. sum of the four components (primary grasp, grip, pinch, and gross movements). Firstly, the respective weights for both variables were calculated using following equations:

$$w_{ATAS} = 1 - \frac{mean_{ATAS}}{mean_{ATAS} + mean_{GS}} \tag{5.5}$$

$$w_{GS} = 1 - \frac{mean_{GS}}{mean_{ATAS} + mean_{GS}} \tag{5.6}$$

Secondly, the raw values of ATAS and GS were multiplied with their respective weights and averaged to generate the final composite score for each session. Next, given brain connectivity data, we implemented cluster-based statistics which is a two-step process, to estimate the sub-networks which are (un)correlated with the composite recovery score. In the first step, partial correlation coefficients between each edge of the FBN and the composite recovery score were computed using Spearman rank correlation coefficient since distribution of the brain connectivity data is unknown and often does not satisfy the normality condition. The second step of our method performs cluster-based multiple comparison correction for correlation coefficients computed in the previous step for all network edges. The neighbouring connections with strong correlation were first grouped together to form clusters and their maximum sizes were calculated. This procedure is repeated for randomly permuted assignments of composite recovery score and finally significance levels of the identified sub-networks are estimated from the null distribution of the cluster sizes [277]. This method is independent of network construction methods: either structural or functional network can be used in association with any functional recovery measures and its efficacy has been proved by several previous studies [278, 279].

It is worth noting that before implementation of the cluster-based statistical analysis, the ROIs for two participant who had right hemisphere lesions were flipped along the x-plane so that all lesions are on the left hemisphere, thus, for all participants, the left hemisphere is the ipsilesional hemisphere.

5.3 Results

This section provides the results obtained from the assessment of the hand function recovery and the cluster-based statistical test of RS MEG FC networks.

5.3.1 Upper-limb functional recovery outcomes

The total ARAT score and the GS (in Kg) are measured five times during the intervention at regular intervals and their values over the five sessions and for all four participants are presented in Fig. 5.3 and Fig. 5.4, respectively. A steady increase in the ARAT score is observed for all the participants and the improvement is in range of 21 for P04 to 26 for P01. In a similar manner, GS scores of all the participants are also improved over the course of intervention, however, in contrast to ARAT score, the incremental changes are highly variable. For P03, there is a high percentage increase in the GS score (approximately 600.0%) whereas the GS is comparatively less improvised (approximately 30.0%) for P01. The improvement in GS score is in range of 1.7 Kg for P01 to 17 Kg for P03. Fig. 5.5 presents the average ARAT and GS scores across the four participants recorded before and after the rehabilitative intervention i.e. pre-intervention (red color) and post-intervention (green color). The error bar represents the standard error mean. Across all the participants, there is a mean change of 23.5 (100.0%) and 8.9 (88.0%) with respect to the mean score of 23.5 and 10.1 recorded at pre-intervention session for ARAT and GS, respectively. The student t-test (paired, two-tailed) is implemented to estimate the statistical significance for the change in pre- and post-intervention values of both parameters. The test provided statistically significant difference in the ARAT score only ($p = 0.00028$). Nevertheless, both measures showed improvements greater than the minimal clinically important difference (MCID).

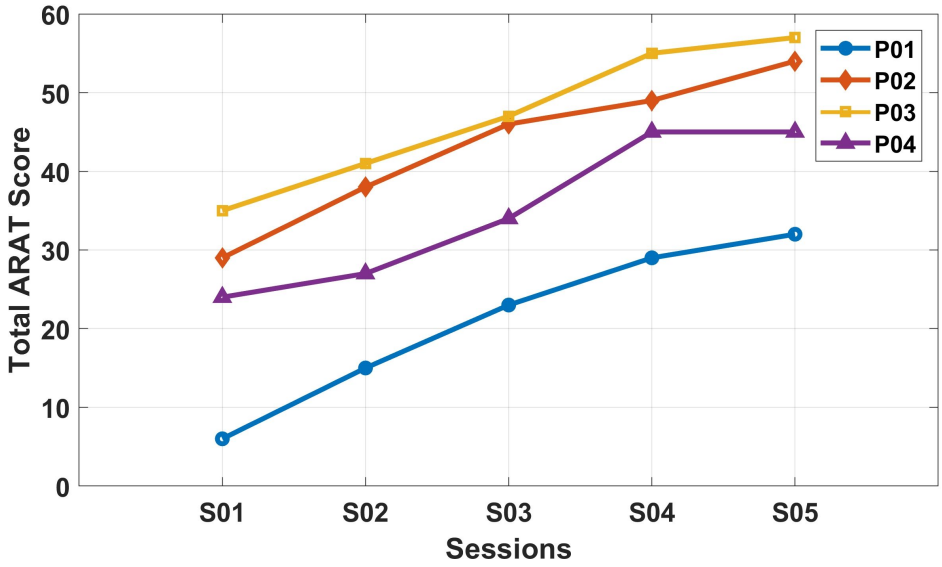

Figure 5.3: The ARAT score recorded over the five sessions of the rehabilitative intervention for the four participants.

5.3.2 MEG connectivity analysis

The cluster-based statistical analysis provided significant functional connectivity sub-networks for alpha (8−15 Hz), beta-low (15−26 Hz), beta-high (26−35 Hz) frequency bands, however, these sub-networks are stable (i.e. presence of any positively/negatively correlated cluster over all the four participants) only for beta-low (15−26 Hz) band. Thus, the further results are presented for beta-low band, unless stated otherwise. The positively and negatively correlated functional connectivity clusters for participant P01, P02, P03, and P04 are depicted over a brain template in Fig. 5.6, 5.7, 5.8, and 5.9, respectively. The black dots represent the ROIs based on the AAL atlas. The nomenclature of the AAL atlas brain regions and their list of abbreviations are provided in Appendix 1. For majority of the participants (i.e. P01, P02, and P04), the intra-hemispherical FC values in motor cortical regions involving precentral gyrus (i.e. primary motor area (M1)), postcentral gyrus (i.e. primary somatosensory cortex (S1)) and supplementary motor area (SMA) within both ipsilesional and contralesional hemispheres increase with UL functional recovery. The cluster-based analysis also showed hemispherical laterlisation wherein the ipsilesional hemisphere possesses larger number of positively correlated clusters while contralesional hemisphere exhibits

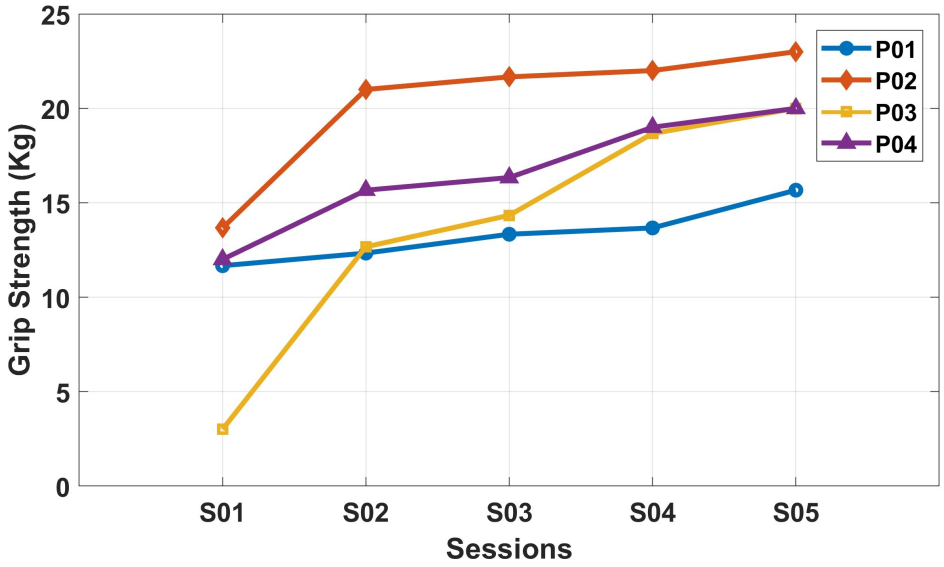

Figure 5.4: The Grip Strength (in Kg) recorded over the five sessions of the rehabilitative intervention for the four participants.

a contrasting characteristics. Moreover, this lateralization is more prominent within the anterior-posterior (i.e. Fronto-parietal) network involving superior frontal gyrus (SFG), inferior frontal gyrus (IFG), superior parietal gyrus (SPG), superior occipital gyrus (SOG), and medial occipital gyrus (MOG). The inter-hemispherical FC analysis showed a stable pattern of positively correlated connections within the motor cortical regions whereas the inter-hemispheric negative cluster is variable across the participant. For each participant, change in the values of FC are estimated as follows:

$$MIM^{i}_{diff} = MIM^{i}_{post} - MIM^{i}_{pre} \tag{5.7}$$

where MIM^{i}_{pre} and MIM^{i}_{post} are FC values for i^{th} ROI of pre- and post-intervention session. Furthermore, node strength of all the significantly correlated ROIs were estimated by adding their associated FC values (one-to-all). Fig. 5.10 presents the average node strengths (across four participants) of all the significantly correlated ROIs. Thus, the group analysis showed increase in node strengths in the motor cortex region and decrease in the node strengths in the frontal, parietal and occipital areas of the contralesional hemisphere.

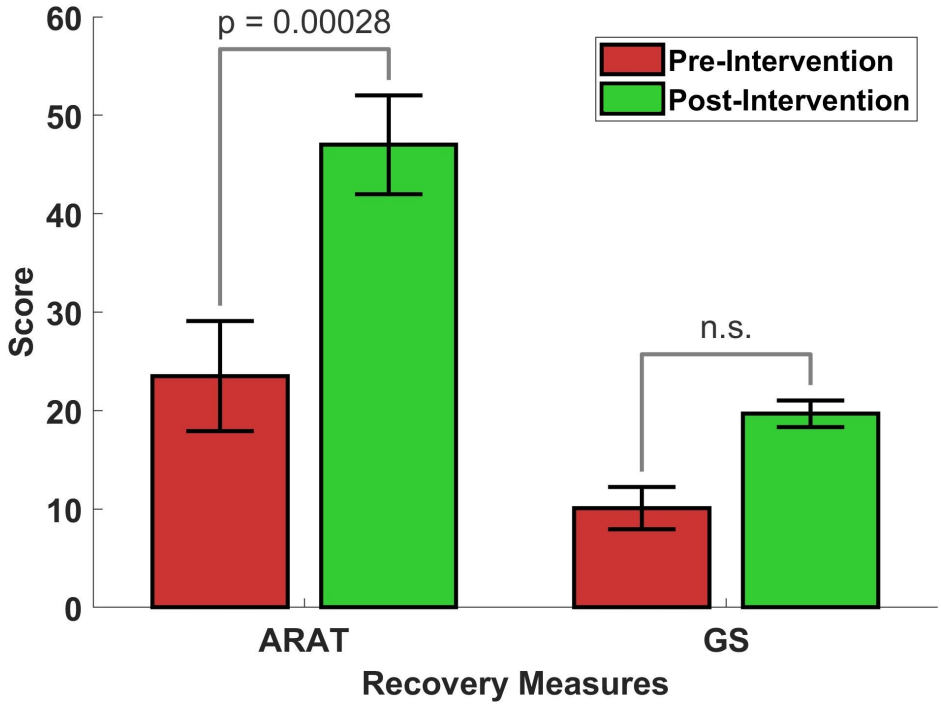

Figure 5.5: The average ARAT and GS scores across the four participants recorded before and after the rehabilitative intervention i.e. pre-intervention (red color) and post-intervention (green color). The error bar represents the standard error mean. Two-tailed, paired student t-test is implemented between pre- and post-intervention scores. n.s.- not significant.

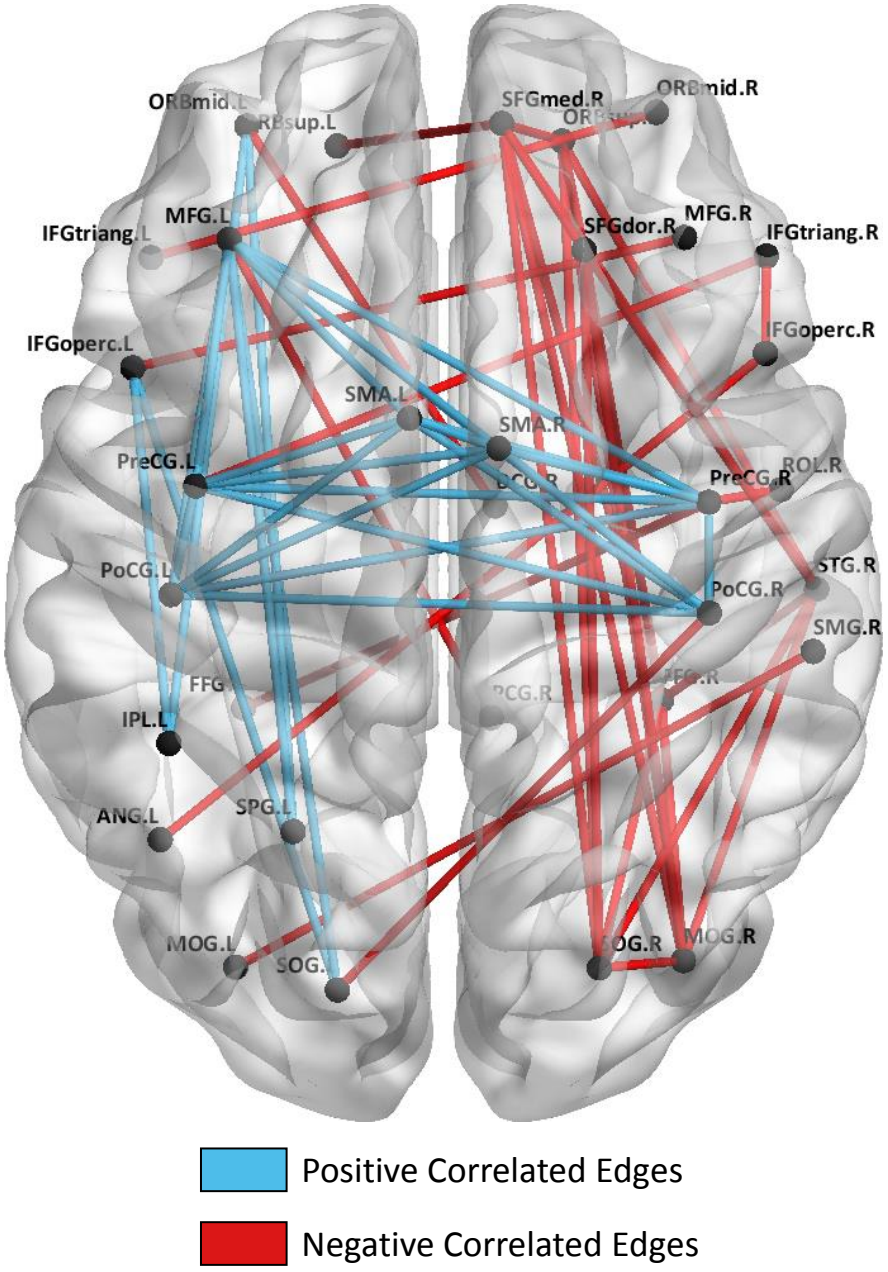

Figure 5.6: Functional connectivity clusters correlated positively (blue) and negatively (Red) with the hand functional recovery index for participant P01 in beta-low (15−26 Hz) frequency band. The nomenclature of the AAL atlas brain regions and their list of abbreviations are provided in Appendix 1. Left = Ipsilesional hemisphere

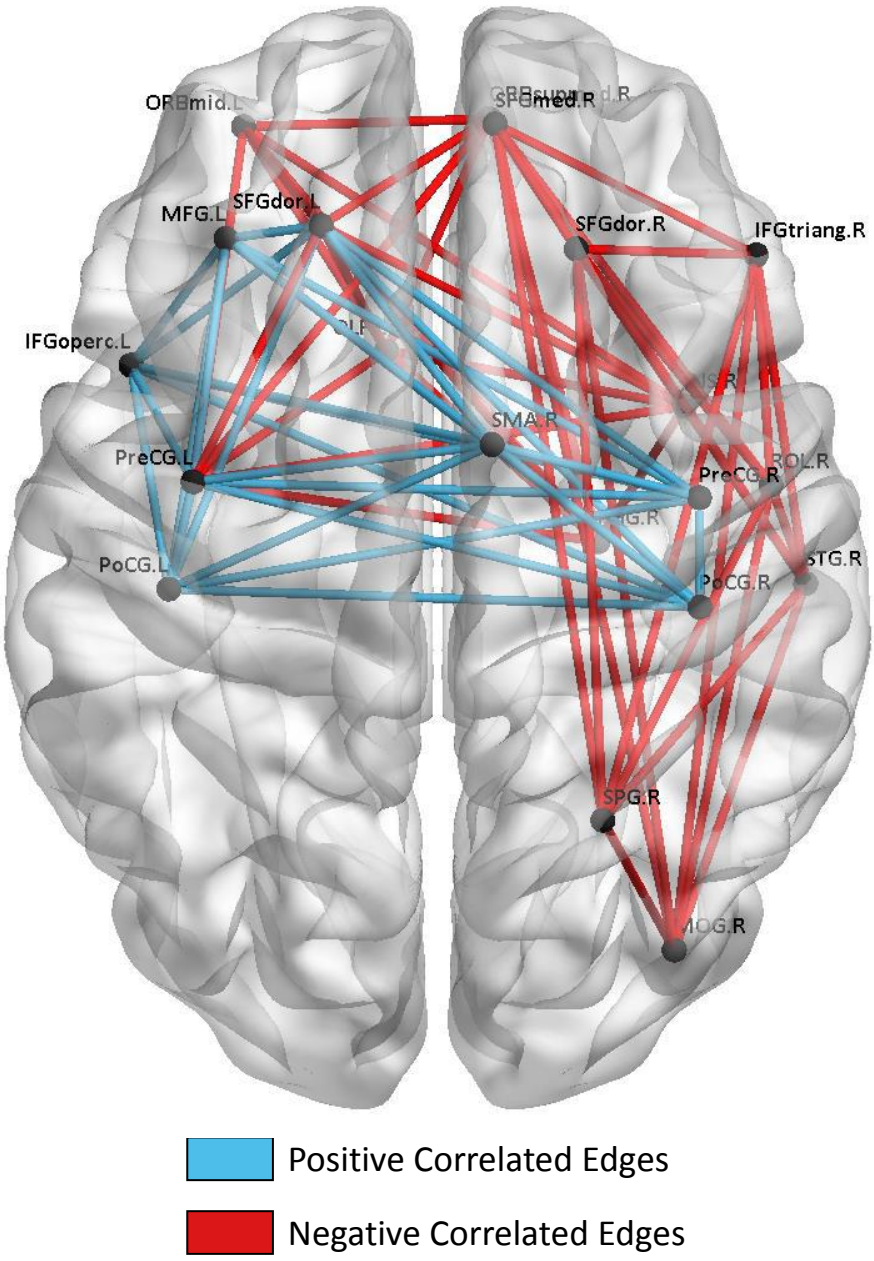

Figure 5.7: Functional connectivity clusters correlated positively (blue) and negatively (Red) with the hand functional recovery index for participant P02 in beta-low (15−26 Hz) frequency band. The nomenclature of the AAL atlas brain regions and their list of abbreviations are provided in Appendix 1. Left = Ipsilesional hemisphere

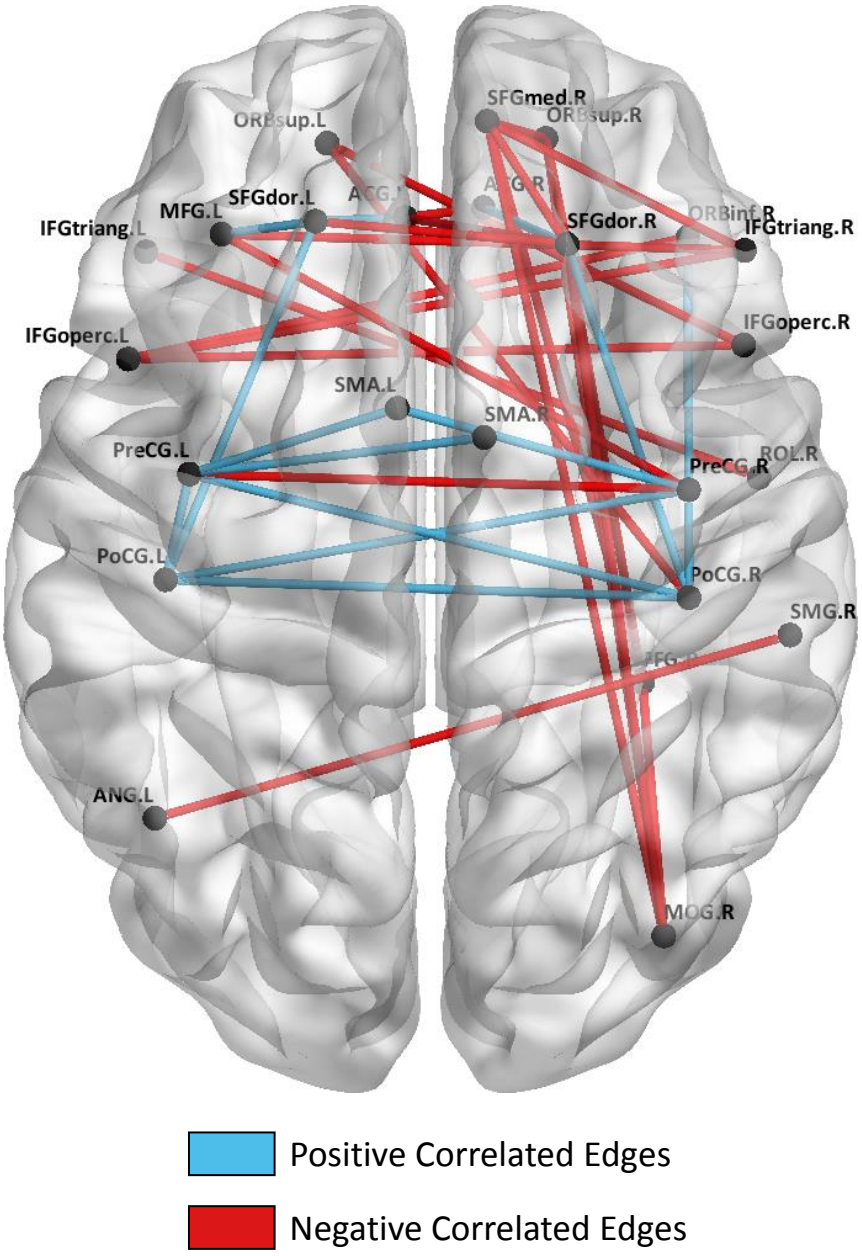

Figure 5.8: Functional connectivity clusters correlated positively (blue) and negatively (Red) with the hand functional recovery index for participant P03 in beta-low (15−26 Hz) frequency band. The nomenclature of the AAL atlas brain regions and their list of abbreviations are provided in Appendix 1. Left = Ipsilesional hemisphere

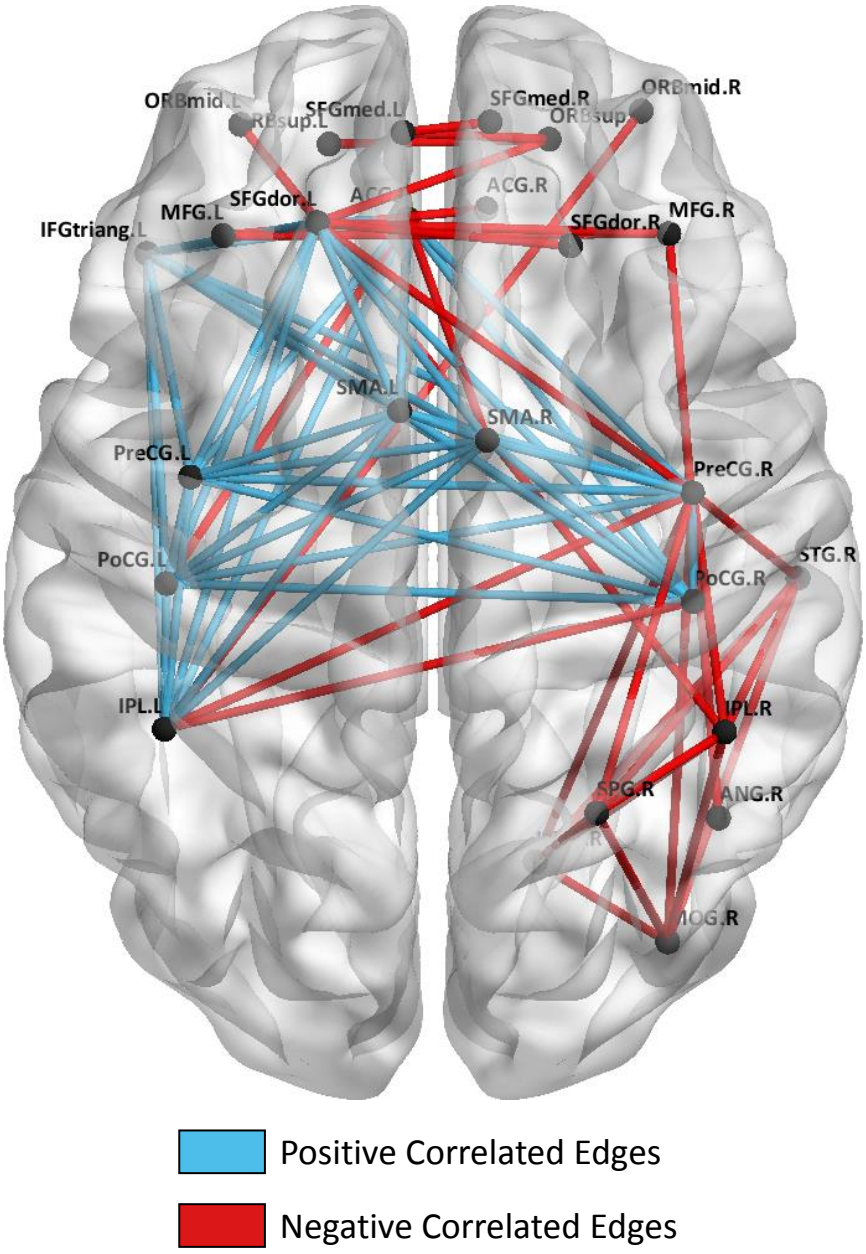

Figure 5.9: Functional connectivity clusters correlated positively (blue) and negatively (Red) with the hand functional recovery index for participant P04 in beta-low (15−26 Hz) frequency band. The nomenclature of the AAL atlas brain regions and their list of abbreviations are provided in Appendix 1. Left = Ipsilesional hemisphere

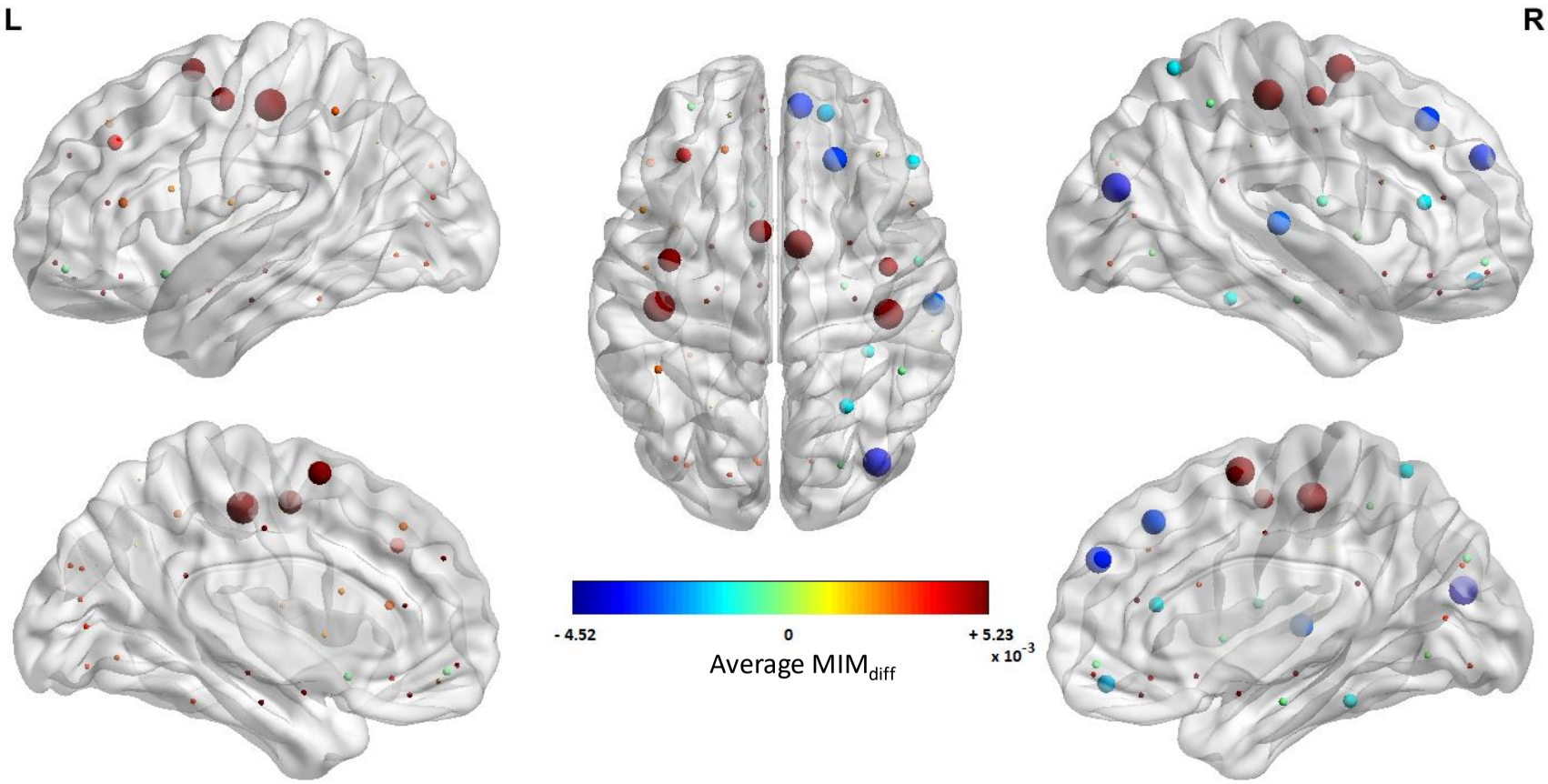

Figure 5.10: The average node strengths (over the participants) for all significantly correlated (both positive and negative) ROIs estimated from the difference between the brain functional connectivity values of the pre-intervention and the post-intervention MEG scans. The nomenclature of the AAL atlas brain regions and their list of abbreviations are provided in Appendix 1. L: Left; R: Right; Ipsilesional hemisphere = Left

5.4 Discussion

Assessment of functional recovery of upper extremities after stroke is highly crucial for restoring ADLs of the patients. Moreover, this assessment can not only validate the effectiveness of the rehabilitative intervention but may contribute to the development of better intervention designs. This study presented a functional connectivity-based neurophysiological assessment of a longitudinal rehabilitative intervention involving the simultaneous implementation of MA, BCI, visual as well as proprioceptive feedback, and robotic hand-exoskeleton. The whole-brain functional connectivity networks using RS MEG data and two different UL functional recovery measures (i.e. ARAT and GS) were acquired for five different sessions over the complete intervention period. Furthermore, a cluster-based statistical analysis was implemented to discover the positively and negatively correlated sub-networks wherein Spearman rank correlation coefficients were estimated between the band-limited whole-brain RS MEG FC networks and the UL functional recovery index. This analysis yielded several major outcomes.

The behavioural assessment of the functional recovery showed gradual improvement in the ARAT and GS scores for all the four participants. A statistically significant increase in the overall ARAT score is obtained with the intervention, while improvements are well over the MCID for both measures. Although, our previous work based on MI-BCI showed inconsistent improvement (over the participants) in both ARAT and GS measures [8], a more stable improvement in this current study may be explained by the major advancement of involving a combination of several rehabilitative modalities together.

The MEG connectivity analysis and the cluster-based statistical testing have given several distinct patterns of brain functional connectome. First, the motor network involving precentral gyrus (i.e. M1), postcentral gyrus (i.e. S1), and SMA brain regions became stronger with UL functional recovery. Both M1 and S1 have been directly associated with motor learning and post-stroke functional recovery whereas SMA is known to play a crucial role in gait control and motor coordination [280, 200, 281]. A strengthened association of these three systems

namely, the M1, S1, and the SMA in a functional network could be beneficial for motor recovery because it might constitute an adapted functional network for processing. Moreover, this pattern emerged in both ipsilesional and contralesional hemispheres of the brain, thus, depicting a bilateral hemispheric effect of the neurorehabilitation intervention. The association of ipsilesional and/or contralesional hemispheres with UL functional recovery is still unclear with inconsistent findings reported elsewhere [234, 210, 282]. However, the implementation of MP and PP to both hands (i.e. healthy and affected) during the rehabilitative intervention may cause the bilateral hemispheric reorganisation of brain observed in this study.

Interestingly, we have observed a lateralised reorganisation of a fronto-parietal network wherein the ipsilesional and the contralesional hemispheres showed enhanced and reduced connectivity strengths, respectively. Fronto-parietal connectivity is known to be involved in top-down attentional control and visuospatial processing [283]. Recently, its association with mobility has been established through a randomised controlled trial involving aerobic exercise [284]. However, the hemispheric lateralization showed specificity of the intervention effect on the FP network. As the intervention involves MA and robotics-guided physical movements, its effect may not only involve physical recovery but also cognitive functional recovery. However, further studies must be undertaken for in-depth assessment of the phenomena.

5.5 Summary

BMI driven robot-assisted neurorehabilitation intervention has demonstrated improvement in UL motor function, specifically, with post-stroke hemiparetic patients. However, neurophysiological patterns related to such interventions are not well understood. This study examined the longitudinal changes in band-limited RS FC networks in association with post-stroke UL functional recovery achieved by a multimodal intervention involving MA based BMI and robotic hand-exoskeleton. Five adults were rehabilitated with the intervention for

a duration of upto 6 weeks. RS MEG signals, ARAT, and GS measures were recorded at five equispaced sessions over the intervention period. An average post-interventional increase of 100.0% ($p = 0.00028$) and 88.0% were attained for ARAT and GS, respectively. A cluster-based statistical test involving correlation estimates between beta-band ($15-26$ Hz) RS-MEG FCs and UL functional recovery provided positively correlated sub-networks in both contralesional and ipsilesional motor cortices. The fronto-parietal FC exhibited hemispheric lateralisation wherein majority of the positively and negatively correlated connections were found in contralesional and ipsilesional hemispheres, respectively. Our findings are consistent with the theory of bilateral motor cortical association with UL recovery and predict novel FC patterns that can be important for higher level cognitive functions.

Chapter 6

Conclusion and future directions

6.1 Thesis Summary

This thesis presented a significant work in the field of computational analysis and modelling of M/EEG data.

- A review of the two often used neuroimaging techniques i.e. electroencephalography (EEG) and magnetoencephalography (MEG) along with the currently available computational algorithms that are implemented for analysis and modelling of the M/EEG data is presented in Chapter 1. In particular, special emphasis is given to various pre-processing methods (i.e. EEG referencing schemes and surface Laplacian (SL) methods), feature extraction methods (i.e. common spatial pattern (CSP) and Granger causality (GC) based connectivity features), and application of single-trial brain activation pattern detection (BAPD) with M/EEG signals. Furthermore, based on this literature review, three open research challenges have been identified to further improve the computational analysis of M/EEG signals in pursuit of performance enhancement of M/EEG-based BAPD systems. Firstly, despite the availability of various referencing schemes and SL methods for EEG, there is no empirical evaluation of their impact on the performance of single-trial EEG BAPD systems. Secondly, over the last few years, several studies showed the

potential of functional connectivity features to be useful for single-trial brain-computer interface (BCI) systems, however, performances of these systems are not sufficiently high to be used for practical applications. Moreover, the majority of these studies showed significantly poor classification accuracies of functional connectivity (FC) features as compared to the features derived from intra-channel signals. Lastly, there is a compelling need to study the patterns of functional brain networks associated with the motor recovery during a longitudinal brain-machine interface-driven UL stroke rehabilitative intervention. These challenges motivated to undertake research to handle these issues associated with current M/EEG-based BAPD systems opening a prospect of novel contributions towards advancing the computational analysis and modelling of M/EEG data.

- In chapter 3, the estimation of current source density (CSD) is introduced as an essential pre-processing step for EEG analysis. Volume conduction (VC) may result in diminished separability of the EEG features for distinct cognitive tasks/processes and hence, adversely affecting the performance of the M/EEG-based BAPD systems. Thus, new robust pre-processing methods are needed to improve the accuracy of single-trial command detection. It is shown that CSD significantly improves the distinction of motor-imagery (MI) related brain responses and has performed better than other referencing schemes (i.e. common reference (CR) and common average reference (CAR)) and spherical surface Laplacian (SSL) methods (i.e. SSL using finite-difference method (SS_F) and SSL using realistic head model (SS_R)). In addition, it is shown that selecting a large number of channels at pre-processing stage (possibly whole scalp coverage) and confining to the motor cortex related channels during feature extraction, yielded better classification accuracies for all the SL methods as compared to other combinations. Furthermore, a significant improvement in the discriminability of the connectivity-based features has been achieved by

introducing CSD as a pre-processing method.

- Discrimination of brain evoked responses corresponding to imagery tasks is a challenge for both the person who has to imagine a specific task and the signal processing methods that have to extract robust discriminant features. Most of the previous studies have focused on MI tasks (e.g., left vs right hand movement) by using features based on the bandpower or log-variance of bandpass signals after spatial filtering. While this approach remains successful for the classification of MI tasks, it has been that the use of features based on effective connectivity using partial-GC (PGC) in the gamma band can lead to more reliable performance in specific imagery tasks, i.e. word generation, numerical subtraction, and spatial navigation tasks. The results presented in Chapter 4 demonstrate significant improvement in single-trial classification performance with FC features as compared to a state-of-the-art method for mixed imagery (i.e. a combination of MI and cognitive imagery) tasks. Finally, the results also suggest that the combination of different imagery tasks opens the scope for improved BCI based on the detection of imagery tasks by increasing the number of possible classes. A major application field of M/EEG-based BAPD systems is post-stroke upper-limb (UL) rehabilitation [27, 28, 8, 29]. However, neurophysiological effects of the attained recovery is still poorly understood. Chapter 5 aims to explore the patterns based on M/EEG functional brain networks(FBNs) in order to better understand the process of stroke recovery and to assess the clinical efficacy of the M/EEG based UL movement rehabilitation.

- Further, a study is undertaken in Chapter 5 to examine the longitudinal changes in band-limited resting-state (RS) FC networks in association with post-stroke UL functional recovery achieved by a multimodal intervention involving motor-attempt (MA) based brain-machine interface (BMI) and robotic hand-exoskeleton. Five adults participated in the neuro-rehabilitation pilot trial involving the multi-modal intervention for a

duration of upto 6 weeks. RS-MEG signals, action research arm test (ARAT), and grip-strength (GS) measures were recorded at five equispaced sessions over the intervention period. An average post-interventional increase of 100.0% ($p = 0.00028$) and 88.0% were attained for ARAT and GS, respectively. A cluster-based statistical test involving correlation estimates between beta-band ($15-26$ Hz) RS-MEG FCs and UL functional recovery provided positively correlated sub-networks in both contralesional and ipsilesional motor cortices. The fronto-parietal FC exhibited hemispheric lateralisation wherein majority of the positively and negatively correlated connections were found in contralesional and ipsilesional hemispheres, respectively. The findings are consistent with the theory of bilateral motor cortical association with UL recovery and predict novel FC patterns that can be important for higher level cognitive functions.

6.2 Limitations and Future Directions

There are following ways that may improve the work presented in this thesis.

- The work presented in Chapter 3 showed significant improvement in the discriminability of the MI related EEG features (both scalp level brain connectivity and filter bank CSP (FBCSP)) by implementation of CSD estimation as a pre-processing step in the analysis. There are several limitations to be considered while using SL for BCI systems and and can be taken into account in future studies. First, montage density of EEG data is a critical consideration, affecting both the surface potential and SL estimates [285]. A dense electrode array EEG montage (64 or more electrodes), providing whole head coverage and with inter-electrode distances less than 2 cm, are generally preferred to a low-density EEG montage (less than 21) with inter-electrode distances greater than 6 cm [182]. Perhaps, this issue can be seen as a possible cause of the reduced effectiveness of the two other Laplacian methods other than CSD (i.e SS_F

and SS_R). But for BCI application, affording high-density montage may not be a suitable choice for varied reasons, e.g., long preparation time, subject inconvenience and it adds to the computational complexity of the system. Second, the pursuit of the maximum accuracy in estimation of the SL has strengthened the predominant consideration of high spatial sampling of the EEG signal in particular to avoid spatial aliasing and other topographic misrepresentations [286, 287]. However, this principle either rejects the usefulness of low density or it overlooks the evidence that the SL transform still renders more useful EEG measures than those obtained from direct surface potentials. Here, we consider that the usefulness of SL must be determined with regards to the research objective and in the case of BCI research, their effectiveness can majorly be assessed in terms of the classification accuracy to predict the targeted identity. Third, with SL pre-processing, several studies showed suppression of low spatial frequency (i.e. originating from deep and/or distributed generator sources) by the Laplacian effect of spatial high-pass filtering. Although the phenomenon has been studied for EEG coherency, its possible effect on spatial filtering based feature extraction methods (as for FBCSP) still needs to be determined [288].

- In Chapter 4, a significant performance improvement of single-trial connectivity-feature based BCI system was achieved by considering a combination of cognitive imagery tasks (i.e. word generation, subtraction, and spatial navigation) and MI tasks (i.e. Left hand, right hand, feet, and tongue). For the mixed imagery tasks, PGC significantly outperformed a state-of-the-art method (i.e. CSP). However, connectivity features related to MI tasks failed to provide high separability between different MI tasks. We also found higher AUCs for mixed imagery tasks (i.e. adding CI and MI) as compared to single imagery type tasks (i.e. either MI or CI only) with both CSP and PGC features which is consistent with findings of several previous studies [238, 289, 290]. However, as per our knowledge, this is the first

study to compare the CI, MI, and the combined tasks pairs for connectivity features. There are several limitations to this study. Firstly, dataset-2 consists of small number of trials, and hence future work may involve validation of the proposed hypothesis with a larger number of trials and also with other non-invasive imaging modalities, such as MEG and functional magnetic resonance imaging (fMRI). Secondly, the linearly mixed noise due to VC is the most challenging problem in scalp-based connectivity analysis. Although we computed CSDs from the raw EEG signal to reduce the amount of spurious interactions before estimating the connectivity matrices, several other methods, including independent component analysis (ICA) decomposition [291] and source localization [292] may provide more robust estimations in the face of higher computational complexity. Thirdly, although we estimated the class-correlation coefficients for all binary classification tasks to find significant connectivity features, the interpretation of neurophysiological mechanisms based on these findings is not absolute and requires further analysis in the source space. The EEG data acquired from the sensors can not be directly related to the underlying neuronal sources as the brain signal undergoes several spatio-temporal transformation before reaching the scalp surface [11, 293]. Thus, for studying actual physiological mechanisms the sensor space data must be source localised before estimation of connectivity features, however, it requires to solve the ill-posed EEG inverse problem. Nevertheless, future work may involve in-depth study of the mixed imagery related physiological interactions at source level.

- Chapter 5 presented an FC-based neurophysiological assessment of a multi-modal longitudinal rehabilitative intervention involving the simultaneous implementation of MA, BCI, visual as well as proprioceptive feedback, and robotic hand-exoskeleton. The whole-brain FC networks using RS MEG data and two different UL functional recovery measures (i.e. ARAT and GS) were acquired for five different sessions over the complete

intervention period. Furthermore, a cluster-based statistical analysis was implemented to discover the positively and negatively correlated sub-networks wherein Spearman rank correlation coefficients were estimated between the band-limited whole-brain RS-MEG FC networks and the UL functional recovery index. There are several limitations to be considered while considering these outcomes of this study. First, as the study involves the implementation of several rehabilitative modalities simultaneously, it is difficult to associate various outcomes with different modalities individually. Thus future studies may consider assessment of RS FC networks for the clinical trials involving various modalities separately and in comparison with healthy control groups. Second, this study involved neurophysiological assessment of the intervention with stroke participants only and lacks the involvement of healthy individuals as a control group. Thus, future work may include a demographically matched control group for assessment of the longitudinal neurophysiological changes in relation to UL functional recovery. Third, these findings must be verified with large sample size and larger intervention duration for further establishment of these neurophysiological patterns as biomarkers for the BMI-driven post-stroke UL functional recovery.

Appendix-I

Nomenclature of Automated Anatomical Labelling (AAL) atlas brain regions and their list of abbreviations

Region No.	Regions	Abbr.	Anatomical Area
1, 2	Precentral gyrus	PreCG	Sensorimotor
3, 4	Superior frontal gyrus, dorsolateral	SFGdor	Frontal
5, 6	Superior frontal gyrus, orbital part	ORBsup	Frontal
7, 8	Middle frontal gyrus	MFG	Frontal
9, 10	Middle frontal gyrus, orbital part	ORBmid	Frontal
11, 12	Inferior frontal gyrus, opercular part	IFGoperc	Frontal
13, 14	Inferior frontal gyrus, triangular part	IFGtriang	Frontal
15, 16	Inferior frontal gyrus, orbital part	ORBinf	Frontal
17, 18	Rolandic operculum	ROL	Frontal
19, 20	Supplementary motor area	SMA	Sensorimotor
21, 22	Olfactory cortex	OLF	Frontal
23, 24	Superior frontal gyrus, medial	SFGmed	Frontal
25, 26	Superior frontal gyrus, medial orbital	ORBsupmed	Frontal
27, 28	Gyrus rectus	REC	Frontal
29, 30	Insula	INS	Subcortical
31, 32	Anterior cingulate & paracingulate gyri	ACG	Frontal
33, 34	Median cingulate & paracingulate gyri	DCG	Frontal
35, 36	Posterior cingulate gyrus	PCG	Parietal
37, 38	Hippocampus	HIP	Temporal
39, 40	Parahippocampal gyrus	PHG	Temporal
41, 42	Amygdala	AMYG	Subcortical

Region No.	Regions	Abbr.	Anatomical Area
43, 44	Calcarine fissure & surrounding cortex	CAL	Occipital
45, 46	Cuneus	CUN	Occipital
47, 48	Lingual gyrus	LING	Occipital
49, 50	Superior occipital gyrus	SOG	Occipital
51, 52	Middle occipital gyrus	MOG	Occipital
53, 54	Inferior occipital gyrus	IOG	Occipital
55, 56	Fusiform gyrus	FFG	Temporal
57, 58	Postcentral gyrus	PoCG	Sensorimotor
59, 60	Superior parietal gyrus	SPG	Parietal
61, 62	Inferior parietal	IPL	Parietal
63, 64	Supramarginal gyrus	SMG	Parietal
65, 66	Angular gyrus	ANG	Parietal
67, 68	Precuneus	PCUN	Parietal
69, 70	Paracentral lobule	PCL	Parietal
71, 72	Caudate nucleus	CAU	Subcortical
73, 74	Lenticular nucleus, putamen	PUT	Subcortical
75, 76	Lenticular nucleus, pallidum	PAL	Subcortical
77, 78	Thalamus	THA	Subcortical
79, 80	Heschl gyrus	HES	Temporal
81, 82	Superior temporal gyrus	STG	Temporal
83, 84	Temporal pole: superior temporal gyrus	TPOsup	Temporal
85, 86	Middle temporal gyrus	MTG	Temporal
87, 88	Temporal pole: middle temporal gyrus	TPOmid	Temporal
89, 90	Inferior temporal gyrus	ITG	Temporal

Bibliography

[1] RSJ Frackowiak and KJ Friston. Methodology of activation paradigms. *Handbook of neuropsychology*, 10:369–369, 1995.

[2] Michael I Posner and Marcus E Raichle. *Images of mind.* New York, NY, US: Scientific American Library/Scientific American Books, 1994.

[3] Per E Roland, Pere E Roland, and Per E Roland. *Brain activation*. Wiley-Liss New York, 1993.

[4] Hans Berger. Electroencephalogram in humans. *Archiv fur Psychiatrie und nervenkrankheiten*, 87:527–570, 1929.

[5] Jonathan D Cohen, William M Perlstein, Todd S Braver, Leigh E Nystrom, Douglas C Noll, John Jonides, and Edward E Smith. Temporal dynamics of brain activation during a working memory task. *Nature*, 386(6625):604, 1997.

[6] Muhammad Imran Khalid, Turky Alotaiby, Saeed A Aldosari, Saleh A Alshebeili, Majed Hamad Al-Hameed, Fida Sadeq Y Almohammed, and Tahani S Alotaibi. Epileptic meg spikes detection using common spatial patterns and linear discriminant analysis. *IEEE Access*, 4:4629–4634, 2016.

[7] M BARRY Sterman. Biofeedback in the treatment of epilepsy. *Cleve Clin J Med*, 77(suppl 3):S60–S67, 2010.

[8] Girijesh Prasad, Pawel Herman, Damien Coyle, Suzanne McDonough, and Jacqueline Crosbie. Applying a brain-computer interface to support motor imagery practice in people with stroke for upper limb recovery: a feasibility study. *Journal of neuroengineering and rehabilitation*, 7(1):60, 2010.

[9] Jonathan R Wolpaw, Niels Birbaumer, Dennis J McFarland, Gert Pfurtscheller, and Theresa M Vaughan. Brain–computer interfaces for communication and control. *Clinical neurophysiology*, 113(6):767–791, 2002.

[10] Torkel Klingberg. Training and plasticity of working memory. *Trends in cognitive sciences*, 14(7):317–324, 2010.

[11] Sebastianus Petrus van den Broek, F Reinders, M Donderwinkel, and MJ Peters. Volume conduction effects in EEG and MEG. *Electroencephalography and clinical neurophysiology*, 106(6):522–534, 1998.

[12] Paul L Nunez and Ramesh Srinivasan. *Electric fields of the brain: the neurophysics of EEG*.

Oxford University Press, USA, 2006.

[13] Ramesh Srinivasan, Paul L Nunez, Don M Tucker, Richard B Silberstein, and Peter J Cadusch. Spatial sampling and filtering of EEG with spline laplacians to estimate cortical potentials. *Brain topography*, 8(4):355–366, 1996.

[14] Bo Hjorth. An on-line transformation of eeg scalp potentials into orthogonal source derivations. *Electroencephalography and clinical neurophysiology*, 39(5):526–530, 1975.

[15] F Perrin, J Pernier, O Bertrand, and JF Echallier. Spherical splines for scalp potential and current density mapping. *Electroencephalography and clinical neurophysiology*, 72(2):184–187, 1989.

[16] Samuel K Law, Paul L Nunez, and Ranjith S Wijesinghe. High-resolution EEG using spline generated surface laplacians on spherical and ellipsoidal surfaces. *IEEE transactions on Biomedical engineering*, 40(2):145–153, 1993.

[17] Siyi Deng, William Winter, Samuel Thorpe, and Ramesh Srinivasan. Improved surface laplacian estimates of cortical potential using realistic models of head geometry. *IEEE Transactions on Biomedical Engineering*, 59(11):2979–2985, 2012.

[18] Ali Bashashati, Mehrdad Fatourechi, Rabab K Ward, and Gary E Birch. A survey of signal processing algorithms in brain–computer interfaces based on electrical brain signals. *Journal of Neural engineering*, 4(2):R32, 2007.

[19] Craig E Tenke and Jürgen Kayser. Generator localization by current source density (CSD): implications of volume conduction and field closure at intracranial and scalp resolutions. *Clinical neurophysiology*, 123(12):2328–2345, 2012.

[20] Claudio Carvalhaes and J Acacio de Barros. The surface laplacian technique in eeg: Theory and methods. *International Journal of Psychophysiology*, 97(3):174–188, 2015.

[21] Guofa Shou and Lei Ding. Detection of EEG spatial–spectral–temporal signatures of errors: A comparative study of ica-based and channel-based methods. *Brain topography*, 28(1):47–61, 2015.

[22] Mahyar Hamedi, Sh-Hussain Salleh, and Alias Mohd Noor. Electroencephalographic motor imagery brain connectivity analysis for bci: a review. *Neural computation*, 28(6):999–1041, 2016.

[23] Dean J Krusienski, Dennis J McFarland, and Jonathan R Wolpaw. Value of amplitude, phase, and coherence features for a sensorimotor rhythm-based brain–computer interface. *Brain research bulletin*, 87(1):130–134, 2012.

[24] Moritz Grosse-Wentrup. Understanding brain connectivity patterns during motor imagery for brain-computer interfacing. In *Advances in neural information processing systems*, pages 561–568, 2009.

[25] Martin Billinger, Clemens Brunner, and Gernot R Müller-Putz. Single-trial connectivity estimation for classification of motor imagery data. *Journal of neural engineering*,

10(4):046006, 2013.

[26] Huaijian Zhang, Ricardo Chavarriaga, and José del R Millán. Discriminant brain connectivity patterns of performance monitoring at average and single-trial levels. *NeuroImage*, 120:64–74, 2015.

[27] Andrea Paggiaro, Niels Birbaumer, Marianna Cavinato, Cristina Turco, Emanuela Formaggio, Alessandra Del Felice, Stefano Masiero, and Francesco Piccione. Magnetoencephalography in stroke recovery and rehabilitation. *Frontiers in neurology*, 7:35, 2016.

[28] Kai Keng Ang, Karen Sui Geok Chua, Kok Soon Phua, Chuanchu Wang, Zheng Yang Chin, Christopher Wee Keong Kuah, Wilson Low, and Cuntai Guan. A randomized controlled trial of eeg-based motor imagery brain-computer interface robotic rehabilitation for stroke. *Clinical EEG and neuroscience*, 46(4):310–320, 2015.

[29] Ethan Buch, Cornelia Weber, Leonardo G Cohen, Christoph Braun, Michael A Dimyan, Tyler Ard, Jurgen Mellinger, Andrea Caria, Surjo Soekadar, Alissa Fourkas, et al. Think to move: a neuromagnetic brain-computer interface (bci) system for chronic stroke. *Stroke*, 39(3):910–917, 2008.

[30] David Cohen. Magnetoencephalography: evidence of magnetic fields produced by alpha-rhythm currents. *Science*, 161(3843):784–786, 1968.

[31] Matti Hämäläinen, Riitta Hari, Risto J Ilmoniemi, Jukka Knuutila, and Olli V Lounasmaa. Magnetoencephalography—theory, instrumentation, and applications to noninvasive studies of the working human brain. *Reviews of modern Physics*, 65(2):413, 1993.

[32] Brian David Josephson. Possible new effects in superconductive tunnelling. *Physics letters*, 1(7):251–253, 1962.

[33] RC Jaklevic, John Lambe, AH Silver, and JE Mercereau. Quantum interference effects in josephson tunneling. *Physical Review Letters*, 12(7):159, 1964.

[34] Bascom S Deaver Jr and William M Fairbank. Experimental evidence for quantized flux in superconducting cylinders. *Physical Review Letters*, 7(2):43, 1961.

[35] Robert Doll and M Näbauer. Experimental proof of magnetic flux quantization in a superconducting ring. *Physical Review Letters*, 7(2):51, 1961.

[36] Fredrik Öisjöen, Justin F Schneiderman, GA Figueras, ML Chukharkin, A Kalabukhov, Anders Hedström, Mikael Elam, and Dag Winkler. High-t c superconducting quantum interference device recordings of spontaneous brain activity: Towards high-t c magnetoencephalography. *Applied Physics Letters*, 100(13):132601, 2012.

[37] Justin F Schneiderman. Information content with low-vs. high-tc squid arrays in meg recordings: The case for high-tc squid-based meg. *Journal of neuroscience methods*, 222:42–46, 2014.

[38] TH Sander, J Preusser, R Mhaskar, J Kitching, L Trahms, and S Knappe. Magnetoencephalography with a chip-scale atomic magnetometer. *Biomedical optics*

express, 3(5):981–990, 2012.

[39] Elena Boto, Sofie S Meyer, Vishal Shah, Orang Alem, Svenja Knappe, Peter Kruger, T Mark Fromhold, Mark Lim, Paul M Glover, Peter G Morris, et al. A new generation of magnetoencephalography: Room temperature measurements using optically-pumped magnetometers. *NeuroImage*, 149:404–414, 2017.

[40] T Iwamoto, R Sawada, T Haruyama, S Mihara, T Doke, Y Hisamatsu, K Kasami, A Maki, T Mori, H Natori, et al. Development of a large volume zero boil-off liquid xenon storage system for muon rare decay experiment (meg). *Cryogenics*, 49(6):254–258, 2009.

[41] Ernst Niedermeyer and FH Lopes da Silva. *Electroencephalography: basic principles, clinical applications, and related fields*. Lippincott Williams & Wilkins, 2005.

[42] TW Picton, S Bentin, P Berg, Emanuel Donchin, SA Hillyard, R Johnson, GA Miller, W Ritter, DS Ruchkin, MD Rugg, et al. Guidelines for using human event-related potentials to study cognition: recording standards and publication criteria. *Psychophysiology*, 37(2):127–152, 2000.

[43] Thomas C Ferree, Phan Luu, Gerald S Russell, and Don M Tucker. Scalp electrode impedance, infection risk, and eeg data quality. *Clinical Neurophysiology*, 112(3):536–544, 2001.

[44] Babak A Taheri, Robert T Knight, and Rosemary L Smith. A dry electrode for eeg recording. *Electroencephalography and clinical neurophysiology*, 90(5):376–383, 1994.

[45] Florin Popescu, Siamac Fazli, Yakob Badower, Benjamin Blankertz, and Klaus-R Müller. Single trial classification of motor imagination using 6 dry eeg electrodes. *PloS one*, 2(7):e637, 2007.

[46] Gaetano Gargiulo, Rafael A Calvo, Paolo Bifulco, Mario Cesarelli, Craig Jin, Armin Mohamed, and André van Schaik. A new eeg recording system for passive dry electrodes. *Clinical Neurophysiology*, 121(5):686–693, 2010.

[47] Hui-Ling Peng, Jing-Quan Liu, Hong-Chang Tian, Yun-Zhao Dong, Bin Yang, Xiang Chen, and Chun-Sheng Yang. A novel passive electrode based on porous ti for eeg recording. *Sensors and Actuators B: Chemical*, 226:349–356, 2016.

[48] Robert Oostenveld and Peter Praamstra. The five percent electrode system for high-resolution eeg and erp measurements. *Clinical neurophysiology*, 112(4):713–719, 2001.

[49] George H Klem, Hans Otto LuÈders, HH Jasper, C Elger, et al. The ten-twenty electrode system of the international federation. *Electroencephalogr Clin Neurophysiol*, 52(3):3–6, 1999.

[50] David Cohen. Magnetoencephalography: detection of the brain's electrical activity with a superconducting magnetometer. *Science*, 175(4022):664–666, 1972.

[51] A Hillebrand and GR Barnes. A quantitative assessment of the sensitivity of whole-head meg to activity in the adult human cortex. *Neuroimage*, 16(3):638–650, 2002.

[52] Nobuhiro Mikuni, Takashi Nagamine, Akio Ikeda, Kiyohito Terada, Waro Taki, Jun Kimura, Haruhiko Kikuchi, and Hiroshi Shibasaki. Simultaneous recording of epileptiform discharges by meg and subdural electrodes in temporal lobe epilepsy. *Neuroimage*, 5(4):298–306, 1997.

[53] Julia M Stephen, Doug M Ranken, Cheryl J Aine, Michael P Weisend, and Jerry J Shih. Differentiability of simulated meg hippocampal, medial temporal and neocortical temporal epileptic spike activity. *Journal of clinical neurophysiology*, 22(6):388–401, 2005.

[54] Lily Riggs, Sandra N Moses, Tim Bardouille, Anthony T Herdman, Bernhard Ross, and Jennifer D Ryan. A complementary analytic approach to examining medial temporal lobe sources using magnetoencephalography. *Neuroimage*, 45(2):627–642, 2009.

[55] Jaakko Malmivuo and Robert Plonsey. *Bioelectromagnetism: principles and applications of bioelectric and biomagnetic fields*. Oxford University Press, USA, 1995.

[56] Ramesh Srinivasan. Anatomical constraints on source models for high-resolution eeg and meg derived from mri. *Technology in cancer research & treatment*, 5(4):389, 2006.

[57] Ramesh Srinivasan, William R Winter, Jian Ding, and Paul L Nunez. Eeg and meg coherence: measures of functional connectivity at distinct spatial scales of neocortical dynamics. *Journal of neuroscience methods*, 166(1):41–52, 2007.

[58] Dennis J McFarland, Lynn M McCane, Stephen V David, and Jonathan R Wolpaw. Spatial filter selection for eeg-based communication. *Electroencephalography and clinical Neurophysiology*, 103(3):386–394, 1997.

[59] Thom F Oostendorp and Adriaan van Oosterom. The surface laplacian of the potential: theory and application. *IEEE Transactions on Biomedical Engineering*, 43(4):394–405, 1996.

[60] Antti Savelainen. An introduction to eeg artifacts. *Independent research projects in applied mathematics*, 2010.

[61] Aina Puce and Matti S Hämäläinen. A review of issues related to data acquisition and analysis in eeg/meg studies. *Brain sciences*, 7(6):58, 2017.

[62] Fabien Lotte, Marco Congedo, Anatole Lécuyer, Fabrice Lamarche, and Bruno Arnaldi. A review of classification algorithms for eeg-based brain–computer interfaces. *Journal of neural engineering*, 4(2):R1, 2007.

[63] Dennis J McFarland and Jonathan R Wolpaw. Sensorimotor rhythm-based brain-computer interface (bci): feature selection by regression improves performance. *IEEE Transactions on Neural Systems and Rehabilitation Engineering*, 13(3):372–379, 2005.

[64] Niels Birbaumer, Nimr Ghanayim, Thilo Hinterberger, Iver Iversen, Boris Kotchoubey, Andrea Kübler, Juri Perelmouter, Edward Taub, and Herta Flor. A spelling device for the paralysed. *Nature*, 398(6725):297, 1999.

[65] G Pfurtscheller, A Aranibar, and W Wege. Changes in central eeg activity in relation to voluntary movement. ii. hemiplegic patients. In *Progress in brain research*, volume 54, pages 491–495. Elsevier, 1980.

[66] Colin Andrew and Gert Pfurtscheller. On the existence of different alpha band rhythms in the hand area of man. *Neuroscience letters*, 222(2):103–106, 1997.

[67] Gert Pfurtscheller, Ch Neuper, Colin Andrew, and Günter Edlinger. Foot and hand area mu rhythms. *International Journal of Psychophysiology*, 26(1-3):121–135, 1997.

[68] O Bertrand, F Perrin, and J Pernier. A theoretical justification of the average reference in topographic evoked potential studies. *Electroencephalography and Clinical Neurophysiology/Evoked Potentials Section*, 62(6):462–464, 1985.

[69] Milton Abramowitz and Irene A Stegun. *Handbook of mathematical functions: with formulas, graphs, and mathematical tables*, volume 55. Courier Corporation, 1964.

[70] Geertjan Huiskamp. Difference formulas for the surface laplacian on a triangulated surface. *Journal of computational physics*, 95(2):477–496, 1991.

[71] Nelson Max. Weights for computing vertex normals from facet normals. *Journal of Graphics Tools*, 4(2):1–6, 1999.

[72] Zoltan J Koles, Michael S Lazar, and Steven Z Zhou. Spatial patterns underlying population differences in the background eeg. *Brain topography*, 2(4):275–284, 1990.

[73] Dieter Devlaminck, Bart Wyns, Moritz Grosse-Wentrup, Georges Otte, and Patrick Santens. Multisubject learning for common spatial patterns in motor-imagery bci. *Computational intelligence and neuroscience*, 2011:8, 2011.

[74] Vahab Youssofzadeh, Damiano Zanotto, KongFatt Wong-Lin, Sunil K Agrawal, and Girijesh Prasad. Directed functional connectivity in fronto-centroparietal circuit correlates with motor adaptation in gait training. *IEEE Transactions on Neural Systems and Rehabilitation Engineering*, 24(11):1265–1275, 2016.

[75] Herbert Ramoser, Johannes Muller-Gerking, and Gert Pfurtscheller. Optimal spatial filtering of single trial eeg during imagined hand movement. *IEEE transactions on rehabilitation engineering*, 8(4):441–446, 2000.

[76] Benjamin Blankertz, Ryota Tomioka, Steven Lemm, Motoaki Kawanabe, and K-R Muller. Optimizing spatial filters for robust eeg single-trial analysis. *IEEE Signal processing magazine*, 25(1):41–56, 2008.

[77] Benjamin Blankertz, Guido Dornhege, Matthias Krauledat, Klaus-Robert Müller, and Gabriel Curio. The non-invasive berlin brain–computer interface: fast acquisition of effective performance in untrained subjects. *NeuroImage*, 37(2):539–550, 2007.

[78] Steven Lemm, Benjamin Blankertz, Gabriel Curio, and K-R Muller. Spatio-spectral filters for improving the classification of single trial eeg. *IEEE transactions on biomedical engineering*, 52(9):1541–1548, 2005.

[79] Guido Dornhege, Benjamin Blankertz, Matthias Krauledat, Florian Losch, Gabriel Curio, and K-R Muller. Combined optimization of spatial and temporal filters for improving brain-computer interfacing. *IEEE transactions on biomedical engineering*, 53(11):2274–2281, 2006.

[80] Ryota Tomioka, Guido Dornhege, Guido Nolte, Benjamin Blankertz, Kazuyuki Aihara, and Klaus-Robert Müller. Spectrally weighted common spatial pattern algorithm for single trial eeg classification. *Dept. Math. Eng., Univ. Tokyo, Tokyo, Japan, Tech. Rep*, 40, 2006.

[81] Norbert Wiener. The theory of prediction. *Modern mathematics for engineers*, 1956.

[82] Clive WJ Granger. Investigating causal relations by econometric models and cross-spectral methods. *Econometrica: Journal of the Econometric Society*, pages 424–438, 1969.

[83] A Korzeniewska, S Kasicki, M Kamiński, and KJ Blinowska. Information flow between hippocampus and related structures during various types of rat's behavior. *Journal of neuroscience methods*, 73(1):49–60, 1997.

[84] Shuixia Guo, Anil K Seth, Keith M Kendrick, Cong Zhou, and Jianfeng Feng. Partial granger causality—eliminating exogenous inputs and latent variables. *Journal of neuroscience methods*, 172(1):79–93, 2008.

[85] Raphaël Gaillard, Stanislas Dehaene, Claude Adam, Stéphane Clémenceau, Dominique Hasboun, Michel Baulac, Laurent Cohen, and Lionel Naccache. Converging intracranial markers of conscious access. *PLoS biology*, 7(3):e1000061, 2009.

[86] Mingzhou Ding, Steven L Bressler, Weiming Yang, and Hualou Liang. Short-window spectral analysis of cortical event-related potentials by adaptive multivariate autoregressive modeling: data preprocessing, model validation, and variability assessment. *Biological cybernetics*, 83(1):35–45, 2000.

[87] Wolfram Hesse, Eva Möller, Matthias Arnold, and Bärbel Schack. The use of time-variant eeg granger causality for inspecting directed interdependencies of neural assemblies. *Journal of neuroscience methods*, 124(1):27–44, 2003.

[88] Thomas Weiss, Wolfram Hesse, Mihaela Ungureanu, Holger Hecht, Lutz Leistritz, Herbert Witte, and Wolfgang HR Miltner. How do brain areas communicate during the processing of noxious stimuli? an analysis of laser-evoked event-related potentials using the granger causality index. *Journal of Neurophysiology*, 99(5):2220–2231, 2008.

[89] Claudio Babiloni, Raffaele Ferri, Giuliano Binetti, Fabrizio Vecchio, Giovanni B Frisoni, Bartolo Lanuzza, Carlo Miniussi, Flavio Nobili, Guido Rodriguez, Francesco Rundo, et al. Directionality of eeg synchronization in alzheimer's disease subjects. *Neurobiology of aging*, 30(1):93–102, 2009.

[90] Adam B Barrett, Michael Murphy, Marie-Aurélie Bruno, Quentin Noirhomme, Mélanie Boly, Steven Laureys, and Anil K Seth. Granger causality analysis of steady-state electroencephalographic signals during propofol-induced anaesthesia. *PloS one*, 7(1):e29072, 2012.

[91] Michael X Cohen and Simon Van Gaal. Dynamic interactions between large-scale brain networks predict behavioral adaptation after perceptual errors. *Cerebral Cortex*, 23(5):1061–1072, 2012.

[92] Alard Roebroeck, Elia Formisano, and Rainer Goebel. Mapping directed influence over the brain using granger causality and fmri. *Neuroimage*, 25(1):230–242, 2005.

[93] Olivier David, Isabelle Guillemain, Sandrine Saillet, Sebastien Reyt, Colin Deransart,

Christoph Segebarth, and Antoine Depaulis. Identifying neural drivers with functional mri: an electrophysiological validation. *PLoS biology*, 6(12):e315, 2008.

[94] Stephen M Smith, Karla L Miller, Gholamreza Salimi-Khorshidi, Matthew Webster, Christian F Beckmann, Thomas E Nichols, Joseph D Ramsey, and Mark W Woolrich. Network modelling methods for fmri. *Neuroimage*, 54(2):875–891, 2011.

[95] Anil K Seth, Paul Chorley, and Lionel C Barnett. Granger causality analysis of fmri bold signals is invariant to hemodynamic convolution but not downsampling. *Neuroimage*, 65:540–555, 2013.

[96] Sanggyun Kim, David Putrino, Soumya Ghosh, and Emery N Brown. A granger causality measure for point process models of ensemble neural spiking activity. *PLoS computational biology*, 7(3):e1001110, 2011.

[97] Meng Hu, Wu Li, and Hualou Liang. A copula-based granger causality measure for the analysis of neural spike train data. *IEEE/ACM Transactions on Computational Biology and Bioinformatics*, 2015.

[98] Lionel Barnett and Anil K Seth. The mvgc multivariate granger causality toolbox: a new approach to granger-causal inference. *Journal of neuroscience methods*, 223:50–68, 2014.

[99] Vahab Youssofzadeh, Girijesh Prasad, Muhammad Naeem, and KongFatt Wong-Lin. Temporal information of directed causal connectivity in multi-trial erp data using partial granger causality. *Neuroinformatics*, 14(1):99–120, 2016.

[100] Adam B Barrett, Lionel Barnett, and Anil K Seth. Multivariate granger causality and generalized variance. *Physical Review E*, 81(4):041907, 2010.

[101] Bjorn Roelstraete and Yves Rosseel. Does partial granger causality really eliminate the influence of exogenous inputs and latent variables? *Journal of neuroscience methods*, 206(1):73–77, 2012.

[102] Daniele Marinazzo, Wei Liao, Huafu Chen, and Sebastiano Stramaglia. Nonlinear connectivity by granger causality. *Neuroimage*, 58(2):330–338, 2011.

[103] Boris Petrovich Bezruchko, Vladimir Ivanovich Ponomarenko, Mikhail Dmitrievich Prokhorov, Dmitrii Alekseevich Smirnov, and Peter Alexander Tass. Modeling nonlinear oscillatory systems and diagnostics of coupling between them using chaotic time series analysis: applications in neurophysiology. *Physics-Uspekhi*, 51(3):304–310, 2008.

[104] Heli Hytti, Reijo Takalo, and Heimo Ihalainen. Tutorial on multivariate autoregressive modelling. *Journal of clinical monitoring and computing*, 20(2):101–108, 2006.

[105] Martin Morf, Augusto Vieira, Daniel TL Lee, and Thomas Kailath. Recursive multichannel maximum entropy spectral estimation. *IEEE Transactions on Geoscience Electronics*, 16(2):85–94, 1978.

[106] Mingzhou Ding, Yonghong Chen, and SL Bressler. Granger causality: basic theory and application to neuroscience. 2006. *arXiv preprint q-bio/0608035*.

[107] M Kay Steven et al. Modern spectral estimation: theory and application. *Signal Processing*

Series, 1988.

[108] John F Geweke. Measures of conditional linear dependence and feedback between time series. *Journal of the American Statistical Association*, 79(388):907–915, 1984.

[109] John Geweke. Measurement of linear dependence and feedback between multiple time series. *Journal of the American statistical association*, 77(378):304–313, 1982.

[110] Luiz A Baccalá and Koichi Sameshima. Partial directed coherence: a new concept in neural structure determination. *Biological cybernetics*, 84(6):463–474, 2001.

[111] Luiz A Baccalá and Koichi Sameshima. Overcoming the limitations of correlation analysis for many simultaneously processed neural structures. In *Progress in brain research*, volume 130, pages 33–47. Elsevier, 2001.

[112] MJ Kaminski and Katarzyna J Blinowska. A new method of the description of the information flow in the brain structures. *Biological cybernetics*, 65(3):203–210, 1991.

[113] James R Patterson and Martin Grabois. Locked-in syndrome: a review of 139 cases. *Stroke*, 17(4):758–764, 1986.

[114] Hideaki Hayashi and Shuichi Kato. Total manifestations of amyotrophic lateral sclerosis: Als in the totally locked-in state. *Journal of the neurological sciences*, 93(1):19–35, 1989.

[115] Aleksander Kostov and Mark Polak. Parallel man-machine training in development of eeg-based cursor control. *IEEE Transactions on Rehabilitation Engineering*, 8(2):203–205, 2000.

[116] Eric W Sellers, Theresa M Vaughan, and Jonathan R Wolpaw. A brain-computer interface for long-term independent home use. *Amyotrophic lateral sclerosis*, 11(5):449–455, 2010.

[117] Andrea Kübler and Niels Birbaumer. Brain–computer interfaces and communication in paralysis: extinction of goal directed thinking in completely paralysed patients? *Clinical neurophysiology*, 119(11):2658–2666, 2008.

[118] Thilo Hinterberger, Stefan Schmidt, Nicola Neumann, Jürgen Mellinger, Benjamin Blankertz, Gabriel Curio, and Niels Birbaumer. Brain-computer communication and slow cortical potentials. *IEEE Transactions on Biomedical Engineering*, 51(6):1011–1018, 2004.

[119] Jdel R Millan and Josep Mouriño. Asynchronous bci and local neural classifiers: an overview of the adaptive brain interface project. *IEEE Transactions on Neural Systems and Rehabilitation Engineering*, 11(2):159–161, 2003.

[120] Brijil Chambayil, Rajesh Singla, and Rameshwar Jha. Virtual keyboard bci using eye blinks in eeg. In *Wireless and Mobile Computing, Networking and Communications (WiMob), 2010 IEEE 6th International Conference on*, pages 466–470. IEEE, 2010.

[121] Bernhard Obermaier, Gemot R Muller, and Gert Pfurtscheller. " virtual keyboard" controlled by spontaneous eeg activity. *IEEE Transactions on Neural Systems and Rehabilitation Engineering*, 11(4):422–426, 2003.

[122] Stefano Silvoni, Chiara Volpato, Marianna Cavinato, Mauro Marchetti, Konstantinos Priftis, Antonio Merico, Paolo Tonin, Konstantinos Koutsikos, Fabrizio Beverina, and Francesco Piccione. P300-based brain-computer interface communication: evaluation and follow-up

in amyotrophic lateral sclerosis. *Frontiers in neuroscience*, 3:1, 2009.

[123] Reza Fazel-Rezai and Kamyar Abhari. A region-based p300 speller for brain-computer interface. *Canadian Journal of Electrical and Computer Engineering*, 34(3):81–85, 2009.

[124] Gustavo P Braz, Michael Russold, and Glen M Davis. Functional electrical stimulation control of standing and stepping after spinal cord injury: a review of technical characteristics. *Neuromodulation: Technology at the Neural Interface*, 12(3):180–190, 2009.

[125] Gert Pfurtscheller, Gernot R Müller, Jörg Pfurtscheller, Hans Jürgen Gerner, and Rüdiger Rupp. 'thought'–control of functional electrical stimulation to restore hand grasp in a patient with tetraplegia. *Neuroscience letters*, 351(1):33–36, 2003.

[126] XL Hu, KY Tong, R Li, M Chen, JJ Xue, SK Ho, and PN Chen. Post-stroke wrist rehabilitation assisted with an intention-driven functional electrical stimulation (fes)-robot system. In *Rehabilitation Robotics (ICORR), 2011 IEEE International Conference on*, pages 1–6. IEEE, 2011.

[127] Gert Pfurtscheller, C Guger, Gernot Müller, G Krausz, and Christa Neuper. Brain oscillations control hand orthosis in a tetraplegic. *Neuroscience letters*, 292(3):211–214, 2000.

[128] Gernot R Müller-Putz, Reinhold Scherer, Gert Pfurtscheller, and Rüdiger Rupp. Eeg-based neuroprosthesis control: a step towards clinical practice. *Neuroscience letters*, 382(1-2):169–174, 2005.

[129] Robert Leeb, Doron Friedman, Gernot R Müller-Putz, Reinhold Scherer, Mel Slater, and Gert Pfurtscheller. Self-paced (asynchronous) bci control of a wheelchair in virtual environments: a case study with a tetraplegic. *Computational intelligence and neuroscience*, 2007:7, 2007.

[130] Dandan Huang, Kai Qian, Ding-Yu Fei, Wenchuan Jia, Xuedong Chen, and Ou Bai. Electroencephalography (eeg)-based brain–computer interface (bci): A 2-d virtual wheelchair control based on event-related desynchronization/synchronization and state control. *IEEE Transactions on Neural Systems and Rehabilitation Engineering*, 20(3):379–388, 2012.

[131] Ricardo Ron-Angevin, Francisco Velasco-Álvarez, Álvaro Fernández-Rodríguez, Antonio Díaz-Estrella, María José Blanca-Mena, and Francisco Javier Vizcaíno-Martín. Brain-computer interface application: auditory serial interface to control a two-class motor-imagery-based wheelchair. *Journal of neuroengineering and rehabilitation*, 14(1):49, 2017.

[132] Christian Mandel, Thorsten Lüth, Tim Laue, Thomas Röfer, Axel Gräser, and Bernd Krieg-Brückner. Navigating a smart wheelchair with a brain-computer interface interpreting steady-state visual evoked potentials. In *Intelligent Robots and Systems, 2009. IROS 2009. IEEE/RSJ International Conference on*, pages 1118–1125. IEEE, 2009.

[133] SM Torres Müller, Wanderley Cardoso Celeste, Teodiano Freire Bastos-Filho, and Mário Sarcinelli-Filho. Brain-computer interface based on visual evoked potentials to command autonomous robotic wheelchair. *Journal of Medical and Biological Engineering*, 30(6):407–

415, 2010.

[134] Gernot R Muller-Putz and Gert Pfurtscheller. Control of an electrical prosthesis with an ssvep-based bci. *IEEE Transactions on Biomedical Engineering*, 55(1):361–364, 2008.

[135] Stephen T Foldes, Douglas J Weber, and Jennifer L Collinger. Meg-based neurofeedback for hand rehabilitation. *Journal of neuroengineering and rehabilitation*, 12(1):85, 2015.

[136] Steven C Cramer, Rajendra Shah, Jenifer Juranek, Kit R Crafton, and Vu Le. Activity in the peri-infarct rim in relation to recovery from stroke. *Stroke*, 37(1):111–115, 2006.

[137] Timothy H Murphy and Dale Corbett. Plasticity during stroke recovery: from synapse to behaviour. *Nature Reviews Neuroscience*, 10(12):861, 2009.

[138] Peter Langhorne, Julie Bernhardt, and Gert Kwakkel. Stroke rehabilitation. *The Lancet*, 377(9778):1693–1702, 2011.

[139] Steven C. Cramer, Steven L. Wolf, Harold P. Adams, Daofen Chen, Alexander W. Dromerick, Kari Dunning, Caitlyn Ellerbe, Andrew Grande, Scott Janis, Maarten G. Lansberg, Ronald M. Lazar, Yuko Y. Palesch, Lorie Richards, Elliot Roth, Sean I. Savitz, Lawrence R. Wechsler, Max Wintermark, and Joseph P. Broderick. Stroke recovery and rehabilitation research. *Stroke*, 48(3):813–819, 2017.

[140] S Graziadio, L Tomasevic, G Assenza, F Tecchio, and JA Eyre. The myth of the 'unaffected'side after unilateral stroke: Is reorganisation of the non-infarcted corticospinal system to re-establish balance the price for recovery? *Experimental neurology*, 238(2):168–175, 2012.

[141] Steven R Zeiler, Ellen M Gibson, Robert E Hoesch, Ming Y Li, Paul F Worley, Richard J O'Brien, and John W Krakauer. Medial premotor cortex shows a reduction in inhibitory markers and mediates recovery in a mouse model of focal stroke. *Stroke*, 44(2):483–489, 2013.

[142] SB Frost, S Barbay, KM Friel, EJ Plautz, and RJ Nudo. Reorganization of remote cortical regions after ischemic brain injury: a potential substrate for stroke recovery. *Journal of neurophysiology*, 89(6):3205–3214, 2003.

[143] P Talelli, RJ Greenwood, and JC Rothwell. Arm function after stroke: neurophysiological correlates and recovery mechanisms assessed by transcranial magnetic stimulation. *Clinical neurophysiology*, 117(8):1641–1659, 2006.

[144] Anna C Zemke, Patrick J Heagerty, Christopher Lee, and Steven C Cramer. Motor cortex organization after stroke is related to side of stroke and level of recovery. *Stroke*, 34(5):e23–e26, 2003.

[145] Katie P Wadden, Todd S Woodward, Paul D Metzak, Katie M Lavigne, Bimal Lakhani, Angela M Auriat, and Lara A Boyd. Compensatory motor network connectivity is associated with motor sequence learning after subcortical stroke. *Behavioural brain research*, 286:136–145, 2015.

[146] Alex R Carter, Serguei V Astafiev, Catherine E Lang, Lisa T Connor, Jennifer Rengachary, Michael J Strube, Daniel LW Pope, Gordon L Shulman, and Maurizio Corbetta. Resting interhemispheric functional magnetic resonance imaging connectivity predicts performance

after stroke. *Annals of neurology*, 67(3):365–375, 2010.

[147] Esteban A Fridman, Takashi Hanakawa, Melissa Chung, Friedhelm Hummel, Ramon C Leiguarda, and Leonardo G Cohen. Reorganization of the human ipsilesional premotor cortex after stroke. *Brain*, 127(4):747–758, 2004.

[148] Nagako Murase, Julie Duque, Riccardo Mazzocchio, and Leonardo G Cohen. Influence of interhemispheric interactions on motor function in chronic stroke. *Annals of neurology*, 55(3):400–409, 2004.

[149] Diane U Jette, Nancy K Latham, Randall J Smout, Julie Gassaway, Mary D Slavin, and Susan D Horn. Physical therapy interventions for patients with stroke in inpatient rehabilitation facilities. *Physical therapy*, 85(3):238–248, 2005.

[150] Dae-Hyouk Bang, Won-Seob Shin, and Ho-Suk Choi. Effects of modified constraint-induced movement therapy with trunk restraint in early stroke patients: A single-blinded, randomized, controlled, pilot trial. *NeuroRehabilitation*, 42(1):29–35, 2018.

[151] Yanna Tong, John T Pendy Jr, William A Li, Huishan Du, Tong Zhang, Xiaokun Geng, and Yuchuan Ding. Motor imagery-based rehabilitation: potential neural correlates and clinical application for functional recovery of motor deficits after stroke. *Aging and disease*, 8(3):364, 2017.

[152] Suvadeep De, Charu Chopra, Daksha Mehta Mehta, and MM Mehndiratta. Comparison between mirror therapy and mental imagery in improving ankle motor recovery in sub acute stroke patients. *Indian Journal of Physiotherapy & Occupational Therapy*, 11(3), 2017.

[153] Tamise Aguiar Caires, Luciane Fernanda Rodrigues Martinho Fernandes, Lislei Jorge Patrizzi, Rafael de Almeida Oliveira, and Luciane Aparecida Pascucci Sande de Souza. Immediate effect of mental practice with and without mirror therapy on muscle activation in hemiparetic stroke patients. *Journal of bodywork and movement therapies*, 21(4):1024–1027, 2017.

[154] PJ Standen, K Threapleton, A Richardson, Louise Connell, DJ Brown, S Battersby, F Platts, and Audrey Burton. A low cost virtual reality system for home based rehabilitation of the arm following stroke: a randomised controlled feasibility trial. *Clinical rehabilitation*, 31(3):340–350, 2017.

[155] Kate E Laver, Belinda Lange, Stacey George, Judith E Deutsch, Gustavo Saposnik, and Maria Crotty. Virtual reality for stroke rehabilitation. *Stroke*, 49(4):e160–e161, 2018.

[156] Zan Yue, Xue Zhang, and Jing Wang. Hand rehabilitation robotics on poststroke motor recovery. *Behavioural neurology*, 2017, 2017.

[157] Giovanni Morone, Stefano Paolucci, Andrea Cherubini, Domenico De Angelis, Vincenzo Venturiero, Paola Coiro, and Marco Iosa. Robot-assisted gait training for stroke patients: current state of the art and perspectives of robotics. *Neuropsychiatric disease and treatment*, 13:1303, 2017.

[158] Mikhail A Lebedev and Miguel AL Nicolelis. Brain-machine interfaces: From basic science to neuroprostheses and neurorehabilitation. *Physiological reviews*, 97(2):767–837, 2017.

[159] Surjo R Soekadar, Niels Birbaumer, Marc W Slutzky, and Leonardo G Cohen. Brain–machine interfaces in neurorehabilitation of stroke. *Neurobiology of disease*, 83:172–179, 2015.

[160] Seth A Hays, Navid Khodaparast, Daniel R Hulsey, Andrea Ruiz, Andrew M Sloan, Robert L Rennaker, and Michael P Kilgard. Vagus nerve stimulation during rehabilitative training improves functional recovery after intracerebral hemorrhage. *Stroke*, pages STROKEAHA–114, 2014.

[161] Kotaro Takeda, Genichi Tanino, and Hiroyuki Miyasaka. Review of devices used in neuromuscular electrical stimulation for stroke rehabilitation. *Medical devices (Auckland, NZ)*, 10:207, 2017.

[162] Ana Dionísio, Isabel Catarina Duarte, Miguel Patrício, and Miguel Castelo-Branco. The use of repetitive transcranial magnetic stimulation for stroke rehabilitation: A systematic review. *Journal of Stroke and Cerebrovascular Diseases*, 27(1):1–31, 2018.

[163] W Klomjai, A Lackmy-Vallee, N Roche, P Pradat-Diehl, V Marchand-Pauvert, and R Katz. Repetitive transcranial magnetic stimulation and transcranial direct current stimulation in motor rehabilitation after stroke: an update. *Annals of physical and rehabilitation medicine*, 58(4):220–224, 2015.

[164] Anne Balossier, Olivier Etard, Chloé Descat, Denis Vivien, and Evelyne Emery. Epidural cortical stimulation as a treatment for poststroke aphasia: a systematic review of the literature and underlying neurophysiological mechanisms. *Neurorehabilitation and neural repair*, 30(2):120–130, 2016.

[165] Richard D Zorowitz. Road to recovery: drugs used in stroke rehabilitation. *Expert review of neurotherapeutics*, 4(2):219–231, 2004.

[166] John W Krakauer. Motor learning: its relevance to stroke recovery and neurorehabilitation. *Current opinion in neurology*, 19(1):84–90, 2006.

[167] Magdalena Ietswaart, Marie Johnston, H Chris Dijkerman, Sara Joice, Clare L Scott, Ronald S MacWalter, and Steven JC Hamilton. Mental practice with motor imagery in stroke recovery: randomized controlled trial of efficacy. *Brain*, 134(5):1373–1386, 2011.

[168] Diljit Singh Kajal, Christoph Braun, Jürgen Mellinger, Matthew D Sacchet, Sergio Ruiz, Eberhard Fetz, Niels Birbaumer, and Ranganatha Sitaram. Learned control of inter-hemispheric connectivity: Effects on bimanual motor performance. *Human brain mapping*, 38(9):4353–4369, 2017.

[169] Doris Broetz, Christoph Braun, Cornelia Weber, Surjo R Soekadar, Andrea Caria, and Niels Birbaumer. Combination of brain-computer interface training and goal-directed physical therapy in chronic stroke: a case report. *Neurorehabilitation and Neural Repair*, 24(7):674–679, 2010.

[170] Andrea Caria, Cornelia Weber, Doris Brötz, Ander Ramos, Luca F Ticini, Alireza Gharabaghi, Christoph Braun, and Niels Birbaumer. Chronic stroke recovery after combined bci training and physiotherapy: a case report. *Psychophysiology*, 48(4):578–582, 2011.

[171] Haider Raza, Hubert Cecotti, Yuhua Li, and Girijesh Prasad. Adaptive learning with covariate shift-detection for motor imagery-based brain–computer interface. *Soft Computing*, 20(8):3085–3096, 2016.

[172] Wei Wu, Zhe Chen, Xiaorong Gao, Yuanqing Li, Emery N Brown, and Shangkai Gao. Probabilistic common spatial patterns for multichannel EEG analysis. *IEEE transactions on pattern analysis and machine intelligence*, 37(3):639–653, 2015.

[173] Feifei Qi, Yuanqing Li, and Wei Wu. RSTFC: A novel algorithm for spatio-temporal filtering and classification of single-trial EEG. *IEEE Trans. Neural Netw. Learn. Syst*, 26(12):3070–3082, 2015.

[174] Yijun Wang and Tzyy-Ping Jung. Improving brain–computer interfaces using independent component analysis. In *Towards Practical Brain-Computer Interfaces*, pages 67–83. Springer, 2012.

[175] Cuntai Guan, Manoj Thulasidas, and Jiankang Wu. High performance P300 speller for brain-computer interface. In *Biomedical circuits and systems, 2004 ieee international workshop on*, pages S3–5. IEEE, 2004.

[176] Willeke Staljanssens, Gregor Strobbe, Pieter van Mierlo, Roel Van Holen, and Stefaan Vandenberghe. EEG beamforming to extract better features of motor imagery in a two-class real-time BCI. In *International conference on basic and clinical multimodal imaging*, volume 20, pages 108–109. SAGE, 2013.

[177] Vikram Shenoy Handiru, A Prasad Vinod, and Cuntai Guan. Cortical source localization for analysing single-trial motor imagery EEG. In *Systems, Man, and Cybernetics (SMC), 2015 IEEE International Conference on*, pages 3146–3151. IEEE, 2015.

[178] Christoph Dinh, Daniel Strohmeier, Martin Luessi, Daniel Güllmar, Daniel Baumgarten, Jens Haueisen, and Matti S Hämäläinen. Real-time MEG source localization using regional clustering. *Brain topography*, 28(6):771–784, 2015.

[179] Bradley J Edelman, Bryan Baxter, and Bin He. EEG source imaging enhances the decoding of complex right-hand motor imagery tasks. *IEEE Transactions on Biomedical Engineering*, 63(1):4–14, 2016.

[180] Febo Cincotti, Donatella Mattia, Fabio Aloise, Simona Bufalari, Laura Astolfi, Fabrizio De Vico Fallani, Andrea Tocci, Luigi Bianchi, Maria Grazia Marciani, Shangkai Gao, et al. High-resolution EEG techniques for brain–computer interface applications. *Journal of neuroscience methods*, 167(1):31–42, 2008.

[181] Michael X Cohen. Comparison of different spatial transformations applied to EEG data: a case study of error processing. *International Journal of Psychophysiology*, 97(3):245–257,

2015.

[182] Sean P Fitzgibbon, Trent W Lewis, David MW Powers, Emma W Whitham, John O Willoughby, and Kenneth J Pope. Surface laplacian of central scalp electrical signals is insensitive to muscle contamination. *IEEE Transactions on Biomedical Engineering*, 60(1):4–9, 2013.

[183] Bartosz Binias, Henryk Palus, and Michał Niezabitowski. Elimination of bioelectrical source overlapping effects from the EEG measurements. In *Carpathian Control Conference (ICCC), 2016 17th International*, pages 70–75. IEEE, 2016.

[184] Jun Lu, Dennis J McFarland, and Jonathan R Wolpaw. Adaptive laplacian filtering for sensorimotor rhythm-based brain–computer interfaces. *Journal of neural engineering*, 10(1):016002, 2012.

[185] Ou Bai, Peter Lin, Sherry Vorbach, Mary Kay Floeter, Noriaki Hattori, and Mark Hallett. A high performance sensorimotor beta rhythm-based brain–computer interface associated with human natural motor behavior. *Journal of neural engineering*, 5(1):24, 2007.

[186] Jonathan R Wolpaw and Dennis J McFarland. Control of a two-dimensional movement signal by a noninvasive brain-computer interface in humans. *Proceedings of the National Academy of Sciences of the United States of America*, 101(51):17849–17854, 2004.

[187] Nazlar Ghassemzadeh and Siamak Haghipour. A review on eeg based brain computer interface systems feature extraction methods. *International Journal of Advanced Biological and Biomedical Research*, 4(2):117–123, 2016.

[188] Thomas Schreiber. Measuring information transfer. *Physical review letters*, 85(2):461, 2000.

[189] L Xu, H Zhang, M Hui, Z Long, Z Jin, Y Liu, and L Yao. Motor execution and motor imagery: a comparison of functional connectivity patterns based on graph theory. *Neuroscience*, 261:184–194, 2014.

[190] Enas S Lawrence, Catherine Coshall, Ruth Dundas, Judy Stewart, Anthony G Rudd, Robin Howard, and Charles DA Wolfe. Estimates of the prevalence of acute stroke impairments and disability in a multiethnic population. *Stroke*, 32(6):1279–1284, 2001.

[191] Pamela W Duncan, Larry B Goldstein, David Matchar, George W Divine, and John Feussner. Measurement of motor recovery after stroke. outcome assessment and sample size requirements. *Stroke*, 23(8):1084–1089, 1992.

[192] Alex Pollock, Gillian Baer, Pauline Campbell, Pei Ling Choo, Anne Forster, Jacqui Morris, Valerie M Pomeroy, and Peter Langhorne. Physical rehabilitation approaches for the recovery of function and mobility following stroke. *The Cochrane Library*, 2014.

[193] Floriana Pichiorri, Giovanni Morone, Manuela Petti, Jlenia Toppi, Iolanda Pisotta, Marco Molinari, Stefano Paolucci, Maurizio Inghilleri, Laura Astolfi, Febo Cincotti, et al. Brain–computer interface boosts motor imagery practice during stroke recovery. *Annals of neurology*, 77(5):851–865, 2015.

[194] Alexander A Frolov, Olesya Mokienko, Roman Lyukmanov, Elena Biryukova, Sergey Kotov,

Lydia Turbina, Georgy Nadareyshvily, and Yulia Bushkova. Post-stroke rehabilitation training with a motor-imagery-based brain-computer interface (bci)-controlled hand exoskeleton: A randomized controlled multicenter trial. *Frontiers in neuroscience*, 11:400, 2017.

[195] Kai Keng Ang, Cuntai Guan, Kok Soon Phua, Chuanchu Wang, Longjiang Zhou, Ka Yin Tang, Ephraim Joseph, J Gopal, Christopher Wee Keong Kuah, and Karen Sui Geok Chua. Brain-computer interface-based robotic end effector system for wrist and hand rehabilitation: results of a three-armed randomized controlled trial for chronic stroke. *Frontiers in neuroengineering*, 7:30, 2014.

[196] EV Biryukova, OG Pavlova, ME Kurganskaya, PD Bobrov, LG Turbina, AA Frolov, VI Davydov, AV Silchenko, and OA Mokienko. Recovery of the motor function of the arm with the aid of a hand exoskeleton controlled by a brain–computer interface in a patient with an extensive brain lesion. *Human Physiology*, 42(1):13–23, 2016.

[197] Alexander A Frolov, Dušan Húsek, Elena V Biryukova, Pavel Dmitrievitch Bobrov, Olesya A Mokienko, and AV Alexandrov. Principles of motor recovery in post-stroke patients using hand exoskeleton controlled by the brain-computer interface based on motor imagery. *Neural Network World*, 27(1):107, 2017.

[198] Esther Monge-Pereira, Jaime Ibañez-Pereda, Isabel M Alguacil-Diego, Jose I Serrano, María P Spottorno-Rubio, and Francisco Molina-Rueda. Use of electroencephalography brain-computer interface systems as a rehabilitative approach for upper limb function after a stroke: A systematic review. *PM&R*, 9(9):918–932, 2017.

[199] Kai Keng Ang and Cuntai Guan. Brain-computer interface in stroke rehabilitation. 2013.

[200] Bálint Várkuti, Cuntai Guan, Yaozhang Pan, Kok Soon Phua, Kai Keng Ang, Christopher Wee Keong Kuah, Karen Chua, Beng Ti Ang, Niels Birbaumer, and Ranganathan Sitaram. Resting state changes in functional connectivity correlate with movement recovery for bci and robot-assisted upper-extremity training after stroke. *Neurorehabilitation and Neural Repair*, 27(1):53–62, 2013.

[201] SV Kotov, LG Turbina, PD Bobrov, AA Frolov, OG Pavlova, ME Kurganskaya, and EV Biryukova. Rehabilitation of stroke patients with a bioengineered "brain–computer interface with exoskeleton" system. *Neuroscience and Behavioral Physiology*, 46(5):518–522, 2016.

[202] OA Mokienko, R Kh Lyukmanov, LA Chernikova, NA Suponeva, MA Piradov, and AA Frolov. Brain–computer interface: The first experience of clinical use in russia. *Human Physiology*, 42(1):24–31, 2016.

[203] Ander Ramos-Murguialday, Doris Broetz, Massimiliano Rea, Leonhard Läer, Özge Yilmaz, Fabricio L Brasil, Giulia Liberati, Marco R Curado, Eliana Garcia-Cossio, Alexandros Vyziotis, et al. Brain–machine interface in chronic stroke rehabilitation: a controlled study. *Annals of neurology*, 74(1):100–108, 2013.

[204] Takashi Ono, Keiichiro Shindo, Kimiko Kawashima, Naoki Ota, Mari Ito, Tetsuo Ota, Masahiko

Mukaino, Toshiyuki Fujiwara, Akio Kimura, Meigen Liu, et al. Brain-computer interface with somatosensory feedback improves functional recovery from severe hemiplegia due to chronic stroke. *Frontiers in neuroengineering*, 7:19, 2014.

[205] Anirban Chowdhury, Haider Raza, Yogesh Kumar Meena, Ashish Dutta, and Girijesh Prasad. Online covariate shift detection based adaptive brain-computer interface to trigger hand exoskeleton feedback for neuro-rehabilitation. *IEEE Transactions on Cognitive and Developmental Systems*, 2017.

[206] Fabrizio Sergi, Hermano Igo Krebs, Benjamin Groissier, Avrielle Rykman, Eugenio Guglielmelli, Bruce T Volpe, and Judith D Schaechter. Predicting efficacy of robot-aided rehabilitation in chronic stroke patients using an mri-compatible robotic device. In *Engineering in Medicine and Biology Society, EMBC, 2011 Annual International Conference of the IEEE*, pages 7470–7473. IEEE, 2011.

[207] G Andrew James, Zhong-Lin Lu, John W VanMeter, K Sathian, Xiaoping P Hu, and Andrew J Butler. Changes in resting state effective connectivity in the motor network following rehabilitation of upper extremity poststroke paresis. *Topics in stroke rehabilitation*, 16(4):270–281, 2009.

[208] Sahil Bajaj, Andrew J Butler, Daniel Drake, and Mukesh Dhamala. Brain effective connectivity during motor-imagery and execution following stroke and rehabilitation. *NeuroImage: Clinical*, 8:572–582, 2015.

[209] Brittany Mei Young, Zack Nigogosyan, Alexander Remsik, Léo M Walton, Jie Song, Veena A Nair, Scott W Grogan, Mitchell E Tyler, Dorothy Farrar Edwards, Kristin Caldera, et al. Changes in functional connectivity correlate with behavioral gains in stroke patients after therapy using a brain-computer interface device. *Frontiers in neuroengineering*, 7:25, 2014.

[210] G Pellegrino, L Tomasevic, M Tombini, G Assenza, M Bravi, S Sterzi, V Giacobbe, L Zollo, E Guglielmelli, G Cavallo, et al. Inter-hemispheric coupling changes associate with motor improvements after robotic stroke rehabilitation. *Restorative neurology and neuroscience*, 30(6):497–510, 2012.

[211] Jonathan R Wolpaw, Dennis J McFarland, Gregory W Neat, and Catherine A Forneris. An EEG-based brain-computer interface for cursor control. *Electroencephalography and clinical neurophysiology*, 78(3):252–259, 1991.

[212] Gert Pfurtscheller, Doris Flotzinger, and Joachim Kalcher. Brain-computer interface – a new communication device for handicapped persons. *Journal of Microcomputer Applications*, 16(3):293–299, 1993.

[213] Benjamin Blankertz, K-R Muller, Dean J Krusienski, Gerwin Schalk, Jonathan R Wolpaw, Alois Schlogl, Gert Pfurtscheller, Jd R Millan, M Schroder, and Niels Birbaumer. The BCI competition III: Validating alternative approaches to actual BCI problems. *IEEE Transactions on Neural Systems and Rehabilitation Engineering*, 14(2):153–159, 2006.

[214] Dheeraj Rathee, Hubert Cecotti, and Girijesh Prasad. Single-trial effective brain connectivity patterns enhance discriminability of mental imagery tasks. *Journal of neural engineering*, 14(5):056005, 2017.

[215] Hubert Cecotti. A self-paced and calibration-less SSVEP-based brain–computer interface speller. *IEEE Transactions on Neural Systems and Rehabilitation Engineering*, 18(2):127–133, 2010.

[216] Hubert Cecotti and Axel Graser. Convolutional neural networks for p300 detection with application to brain-computer interfaces. *IEEE transactions on pattern analysis and machine intelligence*, 33(3):433–445, 2011.

[217] Dennis J McFarland, William A Sarnacki, and Jonathan R Wolpaw. Electroencephalographic (EEG) control of three-dimensional movement. *Journal of neural engineering*, 7(3):036007, 2010.

[218] Bin He, Bryan Baxter, Bradley J Edelman, Christopher C Cline, and W Ye Wenjing. Noninvasive brain-computer interfaces based on sensorimotor rhythms. *Proceedings of the IEEE*, 103(6):907–925, 2015.

[219] Alois Schlögl, Felix Lee, Horst Bischof, and Gert Pfurtscheller. Characterization of four-class motor imagery EEG data for the BCI-competition 2005. *Journal of neural engineering*, 2(4):L14, 2005.

[220] Francois Perrin, Olivier Bertrand, and Jacques Pernier. Scalp current density mapping: value and estimation from potential data. *IEEE Transactions on Biomedical Engineering*, (4):283–288, 1987.

[221] Michael Tangermann, Klaus-Robert Müller, Ad Aertsen, Niels Birbaumer, Christoph Braun, Clemens Brunner, Robert Leeb, Carsten Mehring, Kai J Miller, Gernot Mueller-Putz, et al. Review of the BCI competition IV. *Frontiers in neuroscience*, 6:55, 2012.

[222] Kai Keng Ang, Zheng Yang Chin, Chuanchu Wang, Cuntai Guan, and Haihong Zhang. Filter bank common spatial pattern algorithm on BCI competition IV datasets 2a and 2b. *Frontiers in neuroscience*, 6:39, 2012.

[223] J Kayser. Current source density (CSD) interpolation using spherical splines–CSD toolbox (version 1.1). *New York State Psychiatric Institute: Division of Cognitive Neuroscience*, 2009.

[224] Robert Oostenveld, Pascal Fries, Eric Maris, and Jan-Mathijs Schoffelen. Fieldtrip: open source software for advanced analysis of MEG, EEG, and invasive electrophysiological data. *Computational intelligence and neuroscience*, 2011:1, 2011.

[225] Dennis J McFarland. The advantages of the surface laplacian in brain–computer interface research. *International Journal of Psychophysiology*, 97(3):271–276, 2015.

[226] Gideon Schwarz et al. Estimating the dimension of a model. *The annals of statistics*, 6(2):461–464, 1978.

[227] CE Tenke, J Kayser, R Fong, P Leite, JP Towey, and GE Bruder. Response-and stimulus-related

ERP asymmetries in a tonal oddball task: a laplacian analysis. *Brain topography*, 10(3):201–210, 1998.

[228] Diana Valbuena, Marco Cyriacks, Ola Friman, Ivan Volosyak, and Axel Graser. Brain-computer interface for high-level control of rehabilitation robotic systems. In *Rehabilitation Robotics, 2007. ICORR 2007. IEEE 10th International Conference on*, pages 619–625. IEEE, 2007.

[229] Hubert Cecotti. Spelling with non-invasive brain–computer interfaces–current and future trends. *Journal of Physiology-Paris*, 105(1-3):106–114, 2011.

[230] Francisco Velasco-Alvarez, Ricardo Ron-Angevin, and Miguel Angel Lopez-Gordo. Bci-based navigation in virtual and real environments. In *International Work-Conference on Artificial Neural Networks*, pages 404–412. Springer, 2013.

[231] Mauro Rodríguez, Ramiro Giménez, Pablo Diez, Enrique Avila, Eric Laciar, Lorena Orosco, and Agustina Garcés Correa. Playing with your mind. In *Journal of Physics: Conference Series*, volume 477, page 012038. IOP Publishing, 2013.

[232] Thorsten O Zander and Christian Kothe. Towards passive brain–computer interfaces: applying brain–computer interface technology to human–machine systems in general. *Journal of neural engineering*, 8(2):025005, 2011.

[233] Yogesh Kumar Meena, Hubert Cecotti, KongFatt Wong-Lin, and Girijesh Prasad. Towards increasing the number of commands in a hybrid brain-computer interface with combination of gaze and motor imagery. In *Engineering in Medicine and Biology Society (EMBC), 2015 37th Annual International Conference of the IEEE*, pages 506–509. IEEE, 2015.

[234] Jennifer Wu, Erin Burke Quinlan, Lucy Dodakian, Alison McKenzie, Nikhita Kathuria, Robert J Zhou, Renee Augsburger, Jill See, Vu H Le, Ramesh Srinivasan, et al. Connectivity measures are robust biomarkers of cortical function and plasticity after stroke. *Brain*, 138(8):2359–2369, 2015.

[235] Hikaru Takeuchi, Yasuyuki Taki, Yuko Sassa, Hiroshi Hashizume, Atsushi Sekiguchi, Ai Fukushima, and Ryuta Kawashima. Brain structures associated with executive functions during everyday events in a non-clinical sample. *Brain Structure and Function*, 218(4):1017–1032, 2013.

[236] Angeliki Papana, Catherine Kyrtsou, Dimitris Kugiumtzis, and Cees Diks. Simulation study of direct causality measures in multivariate time series. *Entropy*, 15(7):2635–2661, 2013.

[237] Elzbieta Olejarczyk, Laura Marzetti, Vittorio Pizzella, and Filippo Zappasodi. Comparison of connectivity analyses for resting state eeg data. *Journal of neural engineering*, 14(3):036017, 2017.

[238] Reinhold Scherer, Josef Faller, Elisabeth VC Friedrich, Eloy Opisso, Ursula Costa, Andrea Kübler, and Gernot R Müller-Putz. Individually adapted imagery improves brain-computer interface performance in end-users with disability. *PloS one*, 10(5):e0123727, 2015.

[239] Denis Kwiatkowski, Peter CB Phillips, Peter Schmidt, and Yongcheol Shin. Testing the null

hypothesis of stationarity against the alternative of a unit root: How sure are we that economic time series have a unit root? *Journal of econometrics*, 54(1-3):159–178, 1992.

[240] James Durbin and Geoffrey S Watson. Testing for serial correlation in least squares regression. ii. *Biometrika*, 38(1/2):159–177, 1951.

[241] Camillo Porcaro, Gianluca Coppola, Francesco Pierelli, Stefano Seri, Giorgio Di Lorenzo, Leo Tomasevic, Carlo Salustri, and Franca Tecchio. Multiple frequency functional connectivity in the hand somatosensory network: an eeg study. *Clinical Neurophysiology*, 124(6):1216–1224, 2013.

[242] Camillo Porcaro, Filippo Zappasodi, Paolo Maria Rossini, and Franca Tecchio. Choice of multivariate autoregressive model order affecting real network functional connectivity estimate. *Clinical Neurophysiology*, 120(2):436–448, 2009.

[243] Hirotugu Akaike. A new look at the statistical model identification. *IEEE transactions on automatic control*, 19(6):716–723, 1974.

[244] Anil K Seth. A matlab toolbox for granger causal connectivity analysis. *Journal of neuroscience methods*, 186(2):262–273, 2010.

[245] Guiomar Niso, Ricardo Bruña, Ernesto Pereda, Ricardo Gutiérrez, Ricardo Bajo, Fernando Maestú, and Francisco del Pozo. Hermes: towards an integrated toolbox to characterize functional and effective brain connectivity. *Neuroinformatics*, 11(4):405–434, 2013.

[246] Tom Fawcett. An introduction to roc analysis. *Pattern recognition letters*, 27(8):861–874, 2006.

[247] Sébastien Hétu, Mathieu Grégoire, Arnaud Saimpont, Michel-Pierre Coll, Fanny Eugène, Pierre-Emmanuel Michon, and Philip L Jackson. The neural network of motor imagery: an ale meta-analysis. *Neuroscience & Biobehavioral Reviews*, 37(5):930–949, 2013.

[248] Kai J Miller, Gerwin Schalk, Eberhard E Fetz, Marcel Den Nijs, Jeffrey G Ojemann, and Rajesh PN Rao. Cortical activity during motor execution, motor imagery, and imagery-based online feedback. *Proceedings of the National Academy of Sciences*, 107(9):4430–4435, 2010.

[249] Melissa M Smith, Kurt E Weaver, Thomas J Grabowski, Rajesh PN Rao, and Felix Darvas. Non-invasive detection of high gamma band activity during motor imagery. *Frontiers in human neuroscience*, 8:817, 2014.

[250] Dora Hermes, Kai J Miller, Mariska J Vansteensel, Erik J Aarnoutse, Frans SS Leijten, and Nick F Ramsey. Neurophysiologic correlates of fmri in human motor cortex. *Human brain mapping*, 33(7):1689–1699, 2012.

[251] Christopher R Conner, Timothy M Ellmore, Thomas A Pieters, Michael A DiSano, and Nitin Tandon. Variability of the relationship between electrophysiology and bold-fmri across cortical regions in humans. *Journal of Neuroscience*, 31(36):12855–12865, 2011.

[252] Jin-Young Park, Moonyoung Chang, Kyeong-Mi Kim, and Hee-Jung Kim. The effect of mirror therapy on upper-extremity function and activities of daily living in stroke patients. *Journal*

of physical therapy science, 27(6):1681–1683, 2015.

[253] SN Waghavkar and SS Ganvir. Effectiveness of mirror therapy to improve hand functions in acute and subacute stroke patients. *Int J Neurorehabilitation*, 2(184):2376–0281, 2015.

[254] D García Carrasco and J Aboitiz Cantalapiedra. Effectiveness of motor imagery or mental practice in functional recovery after stroke: a systematic review. *Neurología (English Edition)*, 31(1):43–52, 2016.

[255] Hua Liu, Lu-ping Song, and Tong Zhang. Mental practice combined with physical practice to enhance hand recovery in stroke patients. *Behavioural Neurology*, 2014, 2014.

[256] L Huang and G van Luijtelaar. Brain computer interface for epilepsy treatment. In *Brain-Computer Interface Systems-Recent Progress and Future Prospects*. InTech, 2013.

[257] Anirban Chowdhury, Haider Raza, Ashish Dutta, and Girijesh Prasad. Eeg-emg based hybrid brain computer interface for triggering hand exoskeleton for neuro-rehabilitation. In *Proceedings of the Advances in Robotics*, page 45. ACM, 2017.

[258] Ronald C Lyle. A performance test for assessment of upper limb function in physical rehabilitation treatment and research. *International Journal of Rehabilitation Research*, 4(4):483–492, 1981.

[259] Samu Taulu and Juha Simola. Spatiotemporal signal space separation method for rejecting nearby interference in meg measurements. *Physics in Medicine & Biology*, 51(7):1759, 2006.

[260] Aapo Hyvarinen. Fast and robust fixed-point algorithms for independent component analysis. *IEEE transactions on Neural Networks*, 10(3):626–634, 1999.

[261] Giulia Barbati, Camillo Porcaro, Filippo Zappasodi, Paolo Maria Rossini, and Franca Tecchio. Optimization of an independent component analysis approach for artifact identification and removal in magnetoencephalographic signals. *Clinical Neurophysiology*, 115(5):1220–1232, 2004.

[262] Arnaud Delorme, Terrence Sejnowski, and Scott Makeig. Enhanced detection of artifacts in EEG data using higher-order statistics and independent component analysis. *Neuroimage*, 34(4):1443–1449, 2007.

[263] Anders M Dale, Bruce Fischl, and Martin I Sereno. Cortical surface-based analysis: I. segmentation and surface reconstruction. *Neuroimage*, 9(2):179–194, 1999.

[264] Bruce Fischl, Martin I Sereno, and Anders M Dale. Cortical surface-based analysis: Ii: inflation, flattening, and a surface-based coordinate system. *Neuroimage*, 9(2):195–207, 1999.

[265] Alexandre Gramfort, Martin Luessi, Eric Larson, Denis A Engemann, Daniel Strohmeier, Christian Brodbeck, Lauri Parkkonen, and Matti S Hämäläinen. MNE software for processing MEG and EEG data. *Neuroimage*, 86:446–460, 2014.

[266] Matti S Hämäläinen and Risto J Ilmoniemi. Interpreting magnetic fields of the brain: minimum norm estimates. *Medical & biological engineering & computing*, 32(1):35–42, 1994.

[267] J-Z Wang, Samuel J Williamson, and Lloyd Kaufman. Magnetic source images determined by a

lead-field analysis: the unique minimum-norm least-squares estimation. *IEEE Transactions on Biomedical Engineering*, 39(7):665–675, 1992.

[268] Manfred Fuchs, Michael Wagner, Thomas Köhler, and Hans-Aloys Wischmann. Linear and nonlinear current density reconstructions. *Journal of clinical Neurophysiology*, 16(3):267–295, 1999.

[269] Arne Ewald, Laura Marzetti, Filippo Zappasodi, Frank C Meinecke, and Guido Nolte. Estimating true brain connectivity from EEG/MEG data invariant to linear and static transformations in sensor space. *Neuroimage*, 60(1):476–488, 2012.

[270] Laura Marzetti, Stefania Della Penna, Abraham Z Snyder, Vittorio Pizzella, Guido Nolte, Francesco de Pasquale, Gian Luca Romani, and Maurizio Corbetta. Frequency specific interactions of MEG resting state activity within and across brain networks as revealed by the multivariate interaction measure. *Neuroimage*, 79:172–183, 2013.

[271] Andreas K Engel, Christian Gerloff, Claus C Hilgetag, and Guido Nolte. Intrinsic coupling modes: multiscale interactions in ongoing brain activity. *Neuron*, 80(4):867–886, 2013.

[272] Guido Nolte, Ou Bai, Lewis Wheaton, Zoltan Mari, Sherry Vorbach, and Mark Hallett. Identifying true brain interaction from EEG data using the imaginary part of coherency. *Clinical neurophysiology*, 115(10):2292–2307, 2004.

[273] L Marzetti, G Nolte, MG Perrucci, GL Romani, and C Del Gratta. The use of standardized infinity reference in EEG coherency studies. *Neuroimage*, 36(1):48–63, 2007.

[274] Jan-Mathijs Schoffelen and Joachim Gross. Source connectivity analysis with MEG and EEG. *Human brain mapping*, 30(6):1857–1865, 2009.

[275] Kensuke Sekihara, Julia P Owen, Stephan Trisno, and Srikantan S Nagarajan. Removal of spurious coherence in MEG source-space coherence analysis. *IEEE Transactions on Biomedical Engineering*, 58(11):3121–3129, 2011.

[276] Nathalie Tzourio-Mazoyer, Brigitte Landeau, Dimitri Papathanassiou, Fabrice Crivello, Olivier Etard, Nicolas Delcroix, Bernard Mazoyer, and Marc Joliot. Automated anatomical labeling of activations in SPM using a macroscopic anatomical parcellation of the MNI MRI single-subject brain. *Neuroimage*, 15(1):273–289, 2002.

[277] Eugene S Edgington. Randomization tests. *The Journal of psychology*, 57(2):445–449, 1964.

[278] Cheol E Han, Luis R Peraza, John-Paul Taylor, and Marcus Kaiser. Predicting age across human lifespan based on structural connectivity from diffusion tensor imaging. In *Biomedical Circuits and Systems Conference (BioCAS), 2014 IEEE*, pages 137–140. IEEE, 2014.

[279] Enrico Glerean, Raj K Pan, Juha Salmi, Rainer Kujala, Juha M Lahnakoski, Ulrika Roine, Lauri Nummenmaa, Sami Leppämäki, Taina Nieminen-von Wendt, Pekka Tani, et al. Reorganization of functionally connected brain subnetworks in high-functioning autism. *Human brain mapping*, 37(3):1066–1079, 2016.

[280] MR Borich, SM Brodie, WA Gray, S Ionta, and LA Boyd. Understanding the role of the primary

somatosensory cortex: Opportunities for rehabilitation. *Neuropsychologia*, 79:246–255, 2015.

[281] Dheeraj Rathee, Hubert Cecotti, and Girijesh Prasad. Estimation of effective fronto-parietal connectivity during motor imagery using partial granger causality analysis. In *Neural Networks (IJCNN), 2016 International Joint Conference on*, pages 2055–2062. IEEE, 2016.

[282] Isabelle Favre, Thomas A Zeffiro, Olivier Detante, Alexandre Krainik, Marc Hommel, and Assia Jaillard. Upper limb recovery after stroke is associated with ipsilesional primary motor cortical activity: a meta-analysis. *Stroke*, 45(4):1077–1083, 2014.

[283] Miranda Scolari, Katharina N Seidl-Rathkopf, and Sabine Kastner. Functions of the human frontoparietal attention network: Evidence from neuroimaging. *Current opinion in behavioral sciences*, 1:32–39, 2015.

[284] Chun L Hsu, John R Best, Shirley Wang, Michelle W Voss, Robin GY Hsiung, Michelle Munkacsy, Winnie Cheung, Todd C Handy, and Teresa Liu-Ambrose. The impact of aerobic exercise on fronto-parietal network connectivity and its relation to mobility: an exploratory analysis of a 6-month randomized controlled trial. *Frontiers in human neuroscience*, 11:344, 2017.

[285] Jürgen Kayser and Craig E Tenke. Issues and considerations for using the scalp surface laplacian in EEG/ERP research: A tutorial review. *International Journal of Psychophysiology*, 97(3):189–209, 2015.

[286] Markus Junghöfer, Thomas Elbert, Paul Leiderer, Patrick Berg, and Brigitte Rockstroh. Mapping EEG-potentials on the surface of the brain: a strategy for uncovering cortical sources. *Brain Topography*, 9(3):203–217, 1997.

[287] Paul L Nunez and Andrew F Westdorp. The surface laplacian, high resolution EEG and controversies. *Brain topography*, 6(3):221–226, 1994.

[288] Paul L Nunez, Ramesh Srinivasan, Andrew F Westdorp, Ranjith S Wijesinghe, Don M Tucker, Richard B Silberstein, and Peter J Cadusch. EEG coherency-I: statistics, reference electrode, volume conduction, laplacians, cortical imaging, and interpretation at multiple scales. *Clinical Neurophysiology*, 103(5):499–515, 1997.

[289] Elisabeth VC Friedrich, Reinhold Scherer, and Christa Neuper. The effect of distinct mental strategies on classification performance for brain–computer interfaces. *International Journal of Psychophysiology*, 84(1):86–94, 2012.

[290] Elisabeth VC Friedrich, Reinhold Scherer, and Christa Neuper. Long-term evaluation of a 4-class imagery-based brain–computer interface. *Clinical Neurophysiology*, 124(5):916–927, 2013.

[291] Stefan Haufe, Vadim V Nikulin, Klaus-Robert Müller, and Guido Nolte. A critical assessment of connectivity measures for eeg data: a simulation study. *Neuroimage*, 64:120–133, 2013.

[292] Munsif Ali Jatoi, Nidal Kamel, Aamir Saeed Malik, Ibrahima Faye, and Tahamina Begum.

A survey of methods used for source localization using eeg signals. *Biomedical Signal Processing and Control*, 11:42–52, 2014.

[293] Sylvain Baillet, John C Mosher, and Richard M Leahy. Electromagnetic brain mapping. *IEEE Signal processing magazine*, 18(6):14–30, 2001.